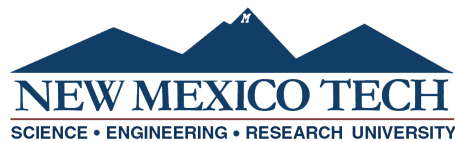


**COMBINED SCHLIEREN AND
IMAGING SPECTROSCOPY FOR MULTI-SPECIES
FLOW FIELD CHARACTERIZATION AND
DENSITY RECONSTRUCTION**

by

Maria J. Ortiz

Submitted in Partial Fulfillment
of the Requirements for the Degree of
Master of Science in Mechanical Engineering
with Specialization in Explosives Engineering



New Mexico Institute of Mining and Technology
Socorro, New Mexico
May 2025

This thesis is dedicated to my family for always supporting me no matter what, and especially to my Grandpa Don. You always told me to "work the problem". This is what I came up with.

Maria J. Ortiz
New Mexico Institute of Mining and Technology
May 2025

ACKNOWLEDGMENTS

I would first like to thank my academic and research advisor, Dr. Hargather, for his guidance, support, and patience throughout this project. From the first summer I arrived at the SGDL to now, you've continually pushed me to confidently be and do "better than my best". I'm a better scientist because of it. I'd also like to thank Dr. Mier for his unwavering support and encouragement over the final months of this work. Thank you to my entire committee for taking the time to help me through this process. Thank you also to Dustin Lester, John Myrkle, and everyone at EMRTC who helped me along the way with testing. Your encouragement and moral support have been truly appreciated.

Thank you to my family for their constant support and understanding over these last few years. Thank you especially to my mom. I'm here today because of all you've done and sacrificed for me to pursue my goals. To Uncle Sandy and Aunt Roxanne, thank you for the best advice and the most love and support I could ever ask for. To Don and Andrew, thank you for never letting me lose sight of my goals, and for providing me with introductions to energetic materials of "various sorts" from as early as I can remember. And to Grandpa Don and Grandma Julie, thank you for always asking the hardest questions and loving me no matter what. My accomplishments are dedicated to and because of all of you.

Thank you also to those friends I made during my undergraduate career who have stuck by my side, even when I moved 2,000 miles away. Our check-ins and constant stream of life updates have truly kept me sane.

Finally, to past and present members of the SGDL and EFDL, my lab mates and friends, thank you for your support, passion, and companionship. Thanks especially to the grad gals, and to those undergraduates who have done the absolute most these last few months. I'll forever cherish our latest nights, earliest mornings, taco truck lunches, and endless discussions of the most random and fantastic topics in life. To quote the grad student who believed in me first, "May Weenie Wednesday live on wherever we are."

This work was sponsored in part by NSF INTENSE REU award 1757793.

This thesis was typeset with L^AT_EX¹ by the author.

¹The L^AT_EX document preparation system was developed by Leslie Lamport as a special version of Donald Knuth's T_EX program for computer typesetting. T_EX is a trademark of the American Mathematical Society. The L^AT_EX macro package for the New Mexico Institute of Mining and Technology thesis format was written by John W. Shipman.

ABSTRACT

Schlieren imaging is a widely used technique to visualize refractive disturbances in gaseous flows, but it lacks the ability to directly determine chemical composition. To address this limitation, a method was developed for simultaneous schlieren imaging and imaging spectroscopy, enabling the visualization and interpretation of chemically complex environments with multiple gas species. Experiments utilized laminar helium plumes infused with iodine gas to compare refractive index changes captured via schlieren imaging with spectrally resolved iodine absorption features recorded through an imaging spectrometer. By applying the Beer-Lambert Law to the spectral data, local iodine concentrations were extracted and correlated spatially with refractive index variations. To simplify the setup, a secondary color-filtered schlieren system was introduced, replacing the spectrometer with narrow bandpass filters centered on specific iodine absorption wavelengths. Quantitative schlieren imaging, paired with dual-wavelength measurements, enabled calculation of both the local refractive field and the species concentration without direct spectral analysis. These measurements were further used to reconstruct the density field across the plume. The methodology demonstrates that color-filtered schlieren imaging, when combined with appropriate calibration and reconstruction algorithms, can simultaneously deliver species concentration and density field information, providing a practical and efficient alternative to traditional multi-diagnostic approaches for chemically non-uniform flows.

Keywords: Schlieren Imaging; Imaging Spectroscopy; Concentration; Beer-Lambert Law; Color-Filtered Schlieren; Optical Diagnostics; Density Reconstruction.

CONTENTS

	Page
LIST OF TABLES	viii
LIST OF FIGURES	ix
NOMENCLATURE	xv
CHAPTER 1. INTRODUCTION	1
1.1 Research motivation	1
1.2 Optical experimental methods	1
1.2.1 Schlieren imaging	1
1.2.2 Shadowgraphy	3
1.3 Spectroscopy	4
1.3.1 Imaging spectroscopy	6
1.4 Tomographic reconstruction	6
1.5 Foundational research	9
1.6 Objectives of the present research	9
CHAPTER 2. EXPERIMENTAL METHODS AND TESTING SETUPS	11
2.1 Imaging diagnostics for simultaneous schlieren and imaging spectroscopy	11
2.1.1 Imaging spectrometer	12
2.2 Imaging diagnostics for color-filtered schlieren	15
2.3 Light source	17
2.4 Camera syncing and triggering	17
2.5 Chemical selection	18
2.6 Gas introduction setup	20
2.6.1 Plume flow rates	21
2.6.2 Plume temperatures	24

CHAPTER 3. SYSTEM CALIBRATION AND IMAGE PROCESSING METHODS	27
3.1 Background subtraction	27
3.2 Distance and sizing calibration	28
3.3 Image registration	31
3.4 Quantitative schlieren methods	32
3.4.1 Color-filtered schlieren calibration	34
3.4.2 Abel inversion transform	38
3.5 Imaging spectrometer calibration	40
3.6 Correlating fields of view between schlieren and imaging spectrometer	42
3.6.1 Aligning center position of both views	42
3.6.2 Imaging spectrometer field of view within schlieren images	43
CHAPTER 4. RESULTS AND DISCUSSION FOR SIMULTANEOUS SCHLIEREN AND IMAGING SPECTROSCOPY	47
4.1 Beer-Lambert Law and data processing	47
4.1.1 Calculating maximum theoretical concentration	52
4.2 Helium-only plumes	52
4.3 Mixed helium-iodine plumes	54
4.3.1 Local absorption coefficient and concentration calculation .	57
4.3.2 Mole fractions and spectrometer-based density reconstruction	62
4.3.3 Schlieren-based density reconstruction	64
4.4 Error calculations	68
4.4.1 Error associated with spectrometer measurements	69
4.4.2 Error associated with schlieren measurements	70
4.5 Final results and discussion	71
CHAPTER 5. DATA, RESULTS, AND DISCUSSION FOR COLOR-FILTERED SCHLIEREN FOR DETERMINING DENSITY FIELD OF HELIUM-IODINE PLUME	73
5.1 Determination of baseline refraction angles using helium-only plume	73
5.2 Refraction and image intensity prediction using helium baseline . .	75
5.3 Absorbance deconvolution and concentration calculations	78
5.4 Density field reconstruction	81
5.5 Final results and discussion	83

CHAPTER 6. CONCLUSIONS AND RECOMMENDATIONS FOR FUTURE WORK 87

REFERENCES 90

APPENDIX A. GAS CONTAINMENT BOX ENGINEERING DRAWINGS 96

A.1 Full Containment Box Assembly 97

A.2 Front Panel 98

A.3 Top Panel 99

A.4 Side Panel 100

LIST OF TABLES

Table	Page
2.1 Helium plume temperatures.	26
2.2 Mixed helium-iodine plume temperatures.	26
3.1 Calibration distances and corresponding uncertainties for images captured through schlieren.	31
3.2 Calibration distances and corresponding uncertainties for images captured through spectrometer.	31

LIST OF FIGURES

Figure	Page
Figure 1.1 Basic setup design of a lens-type schlieren system. See text and nomenclature listings for detailed description.	2
Figure 1.2 Diagram of the direct shadowgraph method in its simplest form. See text and nomenclature listings for detailed description.	4
Figure 1.3 Diagram depicting the use of tomographic reconstruction inversions and transforms to deconvolve line of sight measurements.	7
Figure 2.1 Setup diagram for simultaneous schlieren and imaging spectroscopy. See text and nomenclature listings for detailed description.	12
Figure 2.2 Experimental setup images for simultaneous schlieren and imaging spectroscopy: (a) iodine containment box with test section and optics, and (b) optical diagnostics setup. See text and nomenclature listings for detailed description.	13
Figure 2.3 Schematic of internal setup of typical Czerny-Turner style imaging spectrometer.	14
Figure 2.4 Setup diagram for simultaneous color-filtered schlieren. See text and nomenclature listings for detailed description.	15
Figure 2.5 Optical diagnostics experimental setup images for color-filtered schlieren. See text and nomenclature listings for detailed description.	16
Figure 2.6 Plot of manufacturer provided SugarCube LED spectral output.	17
Figure 2.7 Schematic for camera triggering during simultaneous schlieren and imaging spectroscopy testing.	18
Figure 2.8 Digital recreation of iodine spectral response found by Tellinghuisen (1973) and Saiz-Lopez (2004). Curves normalized for comparison.	19
Figure 2.9 Solid iodine grains used in experimental testing.	20
Figure 2.10 Experimental setup images for gas introduction setup: (a) helium gas introduction system overview, (b) iodine heating chamber, and (c) directional valve for switching between pure helium plumes and mixed helium-iodine plumes.	22

Figure 2.11	Example of thermocouple positioning within a pure helium plume for temperature measurements: (a) thermocouple positioned immediately above pipe exit, and (b) thermocouple positioned 40 mm above pipe exit.	25
Figure 3.1	(a) Schlieren field of view before performing background subtraction. (b) Same field of view after background subtraction. It should be noted that the background is more uniform and specks on the lens have been removed.	28
Figure 3.2	(a) Spectrometer field of view before performing background subtraction. (b) Same field of view after background subtraction. It should be noted that the background is more uniform along the horizontal axis and specks on the lens have been removed. (c) Artificial background image created to perform background subtraction.	29
Figure 3.3	(a) Calibration lens holder in schlieren field of view for determining pixel to length ratio in images. (b) Outer boundary of calibration item (red) and center-line across for distance measurement (blue) determined from image processing. It should be noted that the boundary is drawn several pixels wide for visualization, but the true boundary used for measurement was a single pixel wide.	30
Figure 3.4	Example of schlieren images captured simultaneously with two-camera system: (a) frames overlaid before performing MATLAB image registration, and (b) frames overlaid after performing MATLAB image registration.	32
Figure 3.5	(a) Calibration lens in field of view with center column of extracted pixels highlighted. (b) Associated calibration curve for quantitative schlieren measurements.	34
Figure 3.6	Example of the data collected through simultaneous color-filtered schlieren: (a) 530 nm filtered schlieren view, and (b) 650 nm filtered schlieren view.	35
Figure 3.7	530 nm color-filtered schlieren view of calibration lens for quantitative schlieren measurements: (a) calibration lens image, (b) corresponding pixel versus intensity calibration curve with region of interest outlined in green, and (c) corresponding refraction angle (ϵ) versus intensity with polynomial fit outlined in green.	36
Figure 3.8	650 nm color-filtered schlieren view of calibration lens for quantitative schlieren measurements: (a) calibration lens image, (b) corresponding pixel versus intensity calibration curve with region of interest outlined in green, and (c) corresponding refraction angle (ϵ) versus intensity with polynomial fit outlined in green.	37
Figure 3.9	Diagram of light path through a circular plume cross-section.	39

Figure 3.10 Color images of imaging spectrometer data: (a) Background spectral response of SugarCube LED, (b) spectral response with helium plume passing through test section, and bandpass filtered spectrum at (c) 450 nm, (d) 500 nm, (e) 530 nm, and (f) 650 nm. . . .	41
Figure 3.11 Relative light intensities of SugarCube LED before and after color bandpass filters are applied.	42
Figure 3.12 Calibration optical post in both schlieren and imaging spectrometer field of view for determining spatial position correlation. Object edges are outlined in blue and their center-lines are drawn in white.	43
Figure 3.13 A small lab jack was used to find the edges of imaging spectrometer field of view within schlieren images: (a) left edge, (b) right edge, (c) top edge, and (d) bottom edge.	44
Figure 3.14 (a) Schlieren field of view with spectrometer view outlined in light blue. (b) Spectrometer view of light emitted by test section. (c) Schlieren view of plume moving through test section, with spectrometer view outlined in light blue. (d) Spectrometer view of light emitted by test section with plume region outlined in dark blue. . .	46
Figure 4.1 Visual depiction of the relationship between incident and transmitted light passing through an absorbing species of an optical path length, b	48
Figure 4.2 Examples of test images captured through imaging spectrometer of the iodine plume: (a) background image of spectral response of SugarCube LED, (b) spectral response resulting from presence of gas plume moving through test section, seen as a darkened vertical stripe across the spectrum, and (c) resulting absorbance map after applying Equation 4.6 to images (a) and (b).	50
Figure 4.3 The center line of the plume traveling through the test section was correlated and aligned between the two data sets: (a) schlieren image with plume center line drawn in white, and (b) spectrometer image with corresponding plume center line drawn in white.	53
Figure 4.4 Processed data for a pure helium plume at $t = 0$ ms as the plume first enters the spectrometer field of view: (a) schlieren view with plume center line marked in white, (b) Beer-Lambert Law processed spectrometer view representing absorption with center line marked in white and regions of interest at 530 nm and 650 nm outlined in green and red, respectively, and (c) line plot of measured absorbance at both wavelengths of interest. It should be noted that the image in (b) has been brightened by a value of 0.3 for easier visualization.	55

Figure 4.5	Processed data for a pure helium plume at $t = 30$ ms: (a) schlieren view with plume center line marked in white, (b) Beer-Lambert Law processed spectrometer view representing absorption with center line marked in white and regions of interest at 530 nm and 650 nm outlined in green and red, respectively, and (c) line plot of measured absorbance at both wavelengths of interest. It should be noted that the image in (b) has been brightened by a value of 0.3 for easier visualization.	56
Figure 4.6	Processed data for a mixed helium-iodine plume at $t = 0$ ms as the plume first enters the spectrometer field of view: (a) schlieren view with plume center line marked in white, (b) Beer-Lambert Law processed spectrometer view representing absorption with center line marked in white and regions of interest at 530 nm and 650 nm outlined in green and red, respectively, and (c) LOS integrated absorbance at both wavelengths of interest. It should be noted that the image in (b) has been brightened by a value of 0.3 for easier visualization.	58
Figure 4.7	Processed data for a mixed helium-iodine plume at $t = 8$ ms: (a) schlieren view with plume center line marked in white, (b) Beer-Lambert Law processed spectrometer view representing absorption with center line marked in white and regions of interest at 530 nm and 650 nm outlined in green and red, respectively, and (c) LOS integrated absorbance at both wavelengths of interest. It should be noted that the image in (b) has been brightened by a value of 0.3 for easier visualization.	59
Figure 4.8	Processed data for a mixed helium-iodine plume at $t = 64$ ms: (a) schlieren view with plume center line marked in white, (b) Beer-Lambert Law processed spectrometer view representing absorption with center line marked in white and regions of interest at 530 nm and 650 nm outlined in green and red, respectively, and (c) LOS integrated absorbance at both wavelengths of interest. It should be noted that the image in (b) has been brightened by a value of 0.3 for easier visualization.	60
Figure 4.9	Processed data for a mixed helium-iodine plume at $t = 64$ ms: (a) Axisymmetric spline fit of LOS integrated absorbance at 530 nm (green dashed line) and the corresponding Radon inverted radial absorption coefficient, $\alpha(x, y)$, at 530 nm (purple), and (b) concentration of iodine gas calculated from $\alpha(x, y)$ using Equation 4.12.	61
Figure 4.10	Optimization of \bar{c}_{total} value to minimize difference in density values calculated for mixed helium iodine plume using purely spectrometer based and refractive imaging based data.	64

Figure 4.11 Comparison of density fields reconstructed using pure spectrometer data and ideal gas law: (a) density field calculated for a pure helium and a mixed helium-iodine plume with region of interest outlined by black box, and (b) a closer view of density behavior inside region of interest.	65
Figure 4.12 Pure helium plume comparison of density reconstruction methods: (a) density field calculated across plume using values obtained first through the spectrometer and then through schlieren imaging with region of interest outlined by black box, and (b) a closer view of density behavior inside region of interest.	66
Figure 4.13 Mixed helium-iodine plume comparison of density reconstruction methods: (a) density field calculated across plume using values obtained first through the spectrometer and then through schlieren imaging with region of interest outlined by black box, and (b) a closer view of density behavior inside region of interest. These were the final density values compared to optimize \bar{c}_{total}	67
Figure 4.14 Comparison of density field calculated through schlieren measurements of a mixed helium iodine plume, before versus after accounting for the addition of a small iodine concentration as measured through spectrometer data.	68
Figure 4.15 Comparison of density fields reconstructed using schlieren imaging in combination with spectroscopic measurements: (a) density fields calculated for a pure helium and a mixed helium-iodine plume with region of interest outlined by black box, and (b) a closer view of density behavior inside region of interest.	69
Figure 5.1 Flow chart detailing methods of data processing used for density reconstruction.	74
Figure 5.2 Baseline refraction angle of light was calculated using helium-only plume moving through in test section: (a) 530 nm view of plume, (b) 650 nm view of plume, and (c) calculated refraction angle (ϵ) values at both wavelengths. In parts a and b, the centerline is white, the edge of the plume is cyan, the end of the analysis region is magenta, and the center row analyzed is outlined in green and red for 530 nm and 650 nm (a and b) respectively.	76
Figure 5.3 (a) Schlieren view of mixed plume at 650 nm with analysis region shown by the red line. (b) Measured epsilon values across plume within outlined region.	77
Figure 5.4 (a) Schlieren view of mixed plume at 530 nm with analysis region outlined. (b) Predicted versus measured intensities from same region of image, calculated using angles of refraction (ϵ).	78

Figure 5.5 (a) Schlieren view of mixed plume at 530 nm with analysis region outlined. (b) Measured LOS integrated absorbance across analysis region of plume and spline fit of measured absorbance. . .	79
Figure 5.6 Processed schlieren data of a mixed helium-iodine plume at $t = 34$ ms: (a) Axisymmetric spline fit of LOS integrated absorbance at 530 nm (green dashed line) and the corresponding Radon inverted radial absorption coefficient, $\alpha(r)$, at 530 nm (purple), and (b) concentration of iodine gas calculated from $\alpha(r)$ using Equation 4.12.	80
Figure 5.7 Comparison of effects of line fitting: (a) single row, averaged rows, and spline fit of LOS integrated absorbance data at 530 nm, and (b) corresponding Radon inverted radial absorption coefficient, $\alpha(r)$, for each measurement.	82
Figure 5.8 Density reconstruction of plumes from color-filtered schlieren images of a helium-only plume (coral) and mixed helium-iodine plume (purple).	83
Figure 5.9 Density color map of pure helium plume using color-filtered schlieren method.	84
Figure 5.10 Iodine concentration color map of mixed helium-iodine plume using color-filtered schlieren method.	85
Figure 5.11 Density color map of mixed helium-iodine plume using color-filtered schlieren method.	86

NOMENCLATURE

Setup abbreviations

SL1, SL2	Schlieren lenses
LS	Light source
KE	Knife edge
SO	Schlieren object
BS	Beam splitter
C1, C2	Cameras
CL	Collimating lens
SPECT	Imaging spectrometer
FL	Focusing lens
BP	Bandpass filter

Flow rate variables

Re	Reynolds number
ρ	Density
P	Pressure
M	Molar mass
R_u	Universal gas constant
T	Temperature
V	Flow velocity
d_{pipe}	Pipe inner diameter
μ	Dynamic viscosity
A_{pipe}	Cross-sectional area
Q	Volumetric flow rate
ν	Kinematic viscosity

Refractive imaging variables

ϵ	Angle of refraction
n	Index of refraction
o	Object distance
i	Image distance
f	Lens focal length
p	Pixel size determined from distance calibration
I	Measured pixel intensity
I_{avg}	Average background intensity
R_x	Position in calibration lens
r_x	Displacement in calibration lens
r_{avg}	Position of zero refraction in calibration lens
x	Displacement on image plane
z	Distance along light path axis
κ	Gladstone-Dale coefficient

Abel inversion transform variables

$\delta(r_i)$	Deviation in refractive index
i	Radial position
j	Azimuthal angle
$D_{i,j}$	Matrix of difference values
ϵ_j	Local refraction angle
$A_{i,j}$	Matrix for Abel inversion calculation
$B_{i,j}$	Matrix for Abel inversion calculation
$n(r_i)$	Local refractive index field
n_0	Ambient refractive index

Absorption spectroscopy variables

I_0	Incident light
I	Transmitted light
b	Optical path length
c	Concentration
A	Absorbance
a	Absorption coefficient
T	Transmittance
σ	Absorption cross-section
N_A	Avogadro's number
$A(x)$	Line of sight integrated absorbance
$\alpha(x, y)$	Local absorption coefficient per unit length

Concentration, molar fractions, and density reconstruction variables

n_{I_2}	Moles of iodine gas
V_{plume}	Volume of plume viewed in test section
d	Approximate plume diameter
L	Overall plume length viewed in test section
c_{max}	Maximum theoretical concentration
$\rho(r)$	Local density field
P	Ambient pressure
$M(r)$	Local molar mass field
$T(r)$	Local temperature field
c_{total}	Total mass concentration within plume
X_{I_2}	Molar fraction iodine gas
X_{He}	Molar fraction helium gas
$n(r)$	Local refractive index field
$\kappa(r)$	Local Gladstone-Dale coefficient field

Error and uncertainty propagation variables

σ_A	Uncertainty in absorption
σ_I	Uncertainty in I , due to imaging noise
σ_{I_0}	Uncertainty in I_0
$\sigma_{\tilde{A}}(x)$	Uncertainty in smoothed LOS absorption
$\tilde{A}(x)$	Smoothed LOS absorption
σ_ρ	Uncertainty in density
σ_P	Uncertainty in pressure
σ_M	Uncertainty in molar mass
σ_P	Uncertainty in temperature
σ_{X_i}	Uncertainty in mole fraction X_i
σ_ε	Uncertainty in deflection angle
Δx	Displacement of light ray (from image calibration)
$\sigma_{\Delta x}$	Uncertainty in displacement measurement
Δn	Change in refractive index from background
$\sigma_{\Delta n}$	Uncertainty in Δn
σ_n	Uncertainty in refractive index
κ_{mix}	Mixed Gladstone–Dale constant (weighted by mole fraction)
$\sigma_{\kappa_{\text{mix}}}$	Uncertainty in κ_{mix}

This thesis is accepted on behalf of the faculty of the Institute by the following committee:

Michael J. Hargather

Academic and Research Advisor

Frank Austin Mier

Michelle J. Creech-Eakman

I release this document to the New Mexico Institute of Mining and Technology.

Maria J. Ortiz

May 31, 2025

CHAPTER 1

INTRODUCTION

1.1 Research motivation

Refractive imaging techniques have been widely used for the characterization of complex flow fields, however, these techniques largely assume a uniform species within the flow field. The presence of mixed species in unknown quantities introduces uncertainties into the measurements with these techniques. Spectroscopy has been used to track the chemical dispersion in a flow, however, these measurements tend to represent one region of the environment at a time and do not allow for visualization of the full flow field at once. This work aims to fill the gap in the understanding of these techniques and the manner in which they may be combined to achieve a measurement of density in a multi-species flow.

In order to characterize these complex mixed-species flow fields, a method was developed and experimentally validated for identifying and further quantifying the presence of mixed chemical species within laminar gas plumes using combined spectroscopic and refractive imaging techniques.

1.2 Optical experimental methods

Optical techniques can be highly effective for both qualitative and quantitative measurements during experimental testing. Their non-invasive nature allows for capturing an accurate representation of the event of interest without causing interactions or disturbances with the flow. Schlieren and shadowgraphy optical techniques, specifically, are of interest because of their ease of use and implementation. They allow for high-speed phenomena to be captured clearly and effectively using high-speed cameras for various scenarios with optically transparent flows.

1.2.1 Schlieren imaging

Schlieren imaging is an optical diagnostic method that is commonly used to visualize refractive index gradients in transparent media [1–3]. The gradients

visualized within schlieren images are caused by changes in density, temperature, pressure, and chemical species within the visualized flow field [4, 5]. The schlieren technique has been used and studied since it was developed in the 1600's by Robert Hooke, who first visualized the refraction of light through candle plumes [1]. Eventually it was developed further to the point of visualizing the first shock waves in the 1800's. Several comprehensive reviews of the schlieren technique have been written, including Settles (2001), Kleine (2010), and Settles and Hargather (2017) [1, 3, 4].

A schematic of a traditional lens-type schlieren setup is provided in Figure 1.1. The lens-type schlieren system uses achromatic doublets as the optics, or lenses (SL1, SL2). Light from a point source (LS) is collimated by the first schlieren optic and refocused by the second schlieren optic. The light is parallel throughout the test section, defined as the area between the two lenses. The light returns to a point one focal length away from the second schlieren optic. A knife-edge cutoff (KE) is placed at the focal point to create the schlieren effect. The light is then captured by a camera (C).

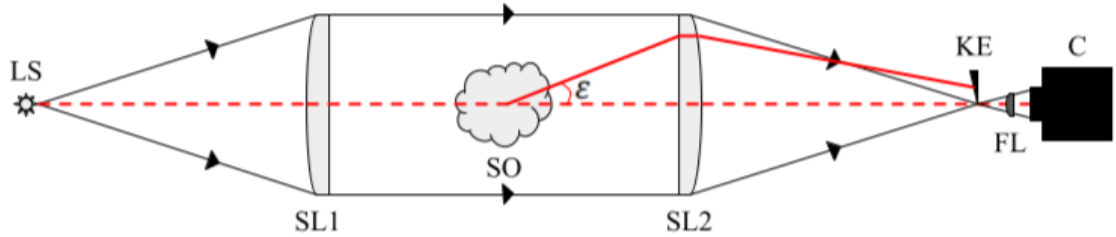


Figure 1.1: Basic setup design of a lens-type schlieren system. See text and nomenclature listings for detailed description.

The resulting schlieren image captures the refraction of the collimated light passing through any variations in refractive index existing within the test section. More specifically, the schlieren imaging technique captures the first spatial derivative of the refractive index [1]. Precise alignment of the components of the schlieren setup is required to accurately take quantitative measurements using this technique. The field of view of the images captured is also limited by the size of the lenses used to create the schlieren setup. These lenses also serve as stops in the system. The changes seen in the schlieren image are first related to changes in angle of refraction, ϵ . The angle of refraction is measured by relating the light intensity at each pixel location within the image to a reference object [2]. Using the small angle assumption for a paraxial system, the relationship between angle of refraction and refractive index is defined as [1]:

$$\epsilon_x = \frac{1}{n} \int \frac{\partial n}{\partial x} dz \approx \frac{Z}{n_\infty} \frac{\partial n}{\partial x} \quad (1.1)$$

$$\epsilon_y = \frac{1}{n} \int \frac{\partial n}{\partial y} dz \approx \frac{Z}{n_\infty} \frac{\partial n}{\partial y} \quad (1.2)$$

where n is the refractive index and z is the distance along the light path axis.

The schlieren technique has been widely applied in fluid research, but more recently it has been applied to the research of energetic materials and explosives due to its ability to resolve quantitative details during high-speed events that normal cameras and techniques cannot capture or resolve. Specifically, it has been used to visualize flow fields such as shock waves, boundary layers, and turbulence because all these can be related to changes in the refractive index within the flow field of interest [5, 6]. It has also recently been applied to optically transparent solids to study both shock wave responses within solids as well as stress field measurements under various loading types [7]. Quantitative schlieren techniques have been used for visualizing phenomena through both fixed length [2, 7] and axisymmetric [8] objects and flow fields.

A major advantage of schlieren imaging is its sensitivity to subtle changes within the gradients visualized as intensity changes within the image, making it well suited to applications like shock fronts and combustion zones. Other major advantages are its simple and repeatable optical setup and the ability to perform both quantitative and qualitative analysis [2, 8].

1.2.2 Shadowgraphy

Another popular method of refractive imaging is shadowgraphy. The shadowgraph technique was invented around the same time as the schlieren technique by Robert Hooke while visualizing the convection from candle plumes as shadows in the background [1]. In its simplest form, shadowgraphy can be performed with the sun as a light source and a surface to cast a shadow. Shadowgraphy can also be performed using the same setup as a schlieren, but without the knife-edge cutoff. This setup produces "focused shadowgraphy" [1]. Where schlieren visualizes the deflection angle, ϵ , of light in the test section, shadowgraphy visualizes the ray displacement resulting from that deflection [1]. In other words, shadowgraphy visualizes the Laplacian of the refractive field, $\frac{\partial^2 n}{\partial x^2}$. Therefore, thin, sharp refractive disturbances are best shown. A diagram of the most simple form of a shadowgraph setup is provided in Figure 1.2.

While shadowgrams are often used to visualize similar phenomena to schlieren images, they are better suited to some flow types than others. For example, shock waves are very clearly visualized in shadowgrams, but Prandtl-Meyer fans are better seen in schlieren images [9]. While the shock waves are better visualized, shadowgrams also de-emphasize other flow features. This is due in part to the lower sensitivity of shadowgraphy to subtle gradients within the flow field in comparison to schlieren imaging. Its sensitivity is proportional to the defocus

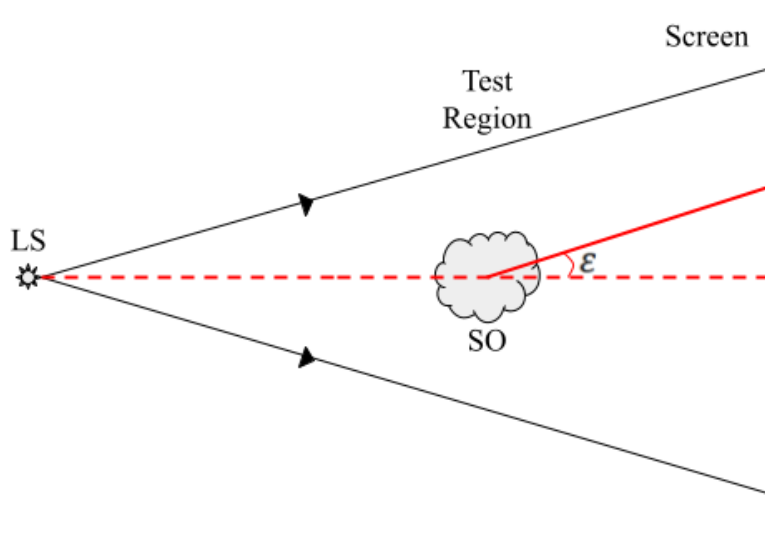


Figure 1.2: Diagram of the direct shadowgraph method in its simplest form. See text and nomenclature listings for detailed description.

distances times the Laplacian of the refractive index [10]. It also cannot be used for direct quantitative density measurement [1, 9, 10]. However, due to its simplicity of setup, shadowgraphy still has the advantage in larger-scale testing where a larger field of view is required to visualize the entire event [9].

1.3 Spectroscopy

The concept of scientific spectroscopy began as early as the 1700s with Newton's observation of white light breaking into colors as it passed through a prism [11]. The growth of the field of spectroscopy continued into the 1800s with the demonstration of distinguishing spectral lines emitted by an electric spark from metal diodes [12]. Around the same time, the emission lines of the sun were charted and the wavelengths of those emission lines were analyzed [12]. Since then, scientific spectroscopy has developed from simply visualizing colors to visualizing individual spectral responses of atoms within solids [13], but its fundamental goals remain the same as they did in the 1800s.

Spectroscopy is based in the study of matter and material properties based on interactions of various forms of radiation with the material of interest [14, 15]. The various analytical methods of spectroscopy rely on the interactions between electromagnetic energy or photons and the atoms or electrons in those materials being analyzed, most frequently looking at emission lines within the ultraviolet and visible ranges of the spectrum resulting from electron transitions between quantum shells [16, 17]. The atomic spectra produced by those interactions give a

simple and effective method of species detection and concentration measurement based on the wavelengths and intensities of the peaks of the spectra [11, 16].

Emission spectroscopy is based on measurements of the spontaneous emission of photons from atoms or ions in a material due to transitions of electrons [11]. The wavelength of the spectral lines emitted gives the sample element's identity and the intensities are proportional to the quantity of photons emitted. This technique has been used as a diagnostic tool in explosives testing for the detection of AlO within fireballs [18], where a time-resolved emission spectroscopy method was used to characterize the spectral evolution of the fireball over time [18]. Similar research was done to explore the spectra of fireballs using absorption spectroscopy [19]. Emission spectroscopy struggles to characterize optically dense or "thick" environments with high opacity and low native luminosity due to the absorption of photons through the sample. Emission spectroscopy essentially creates its own light, but when there is not enough emission from the excited gas species, it must be backlit to see the chemical species. Absorption spectroscopy was therefore chosen for that research because its measurements are line-of-sight averaged and allow characterization inside the fireball rather than just its surface effects [19].

Emission spectra were studied before absorption spectra because they are easier to detect [11, 20], but atomic absorption spectroscopy is the most popularly used atomic spectrometric technique for detecting and characterizing elements within a sample [16]. Absorption spectroscopy is based on the absorption of photons by electrons in the atoms in the material [11]. More specifically, it is the measurement of the process when electrons absorb electromagnetic radiation at a given frequency or wavelength, exciting the electrons to corresponding upper energy levels in the atom [16]. Absorption as a function of wavelength produces the absorption spectrum, which is characteristic of the given material and its concentration [20]. Absorption spectroscopy has been used widely in the literature for purposes ranging from detecting biomass and vegetation levels [20] to measuring product formation within high-temperature fireballs [21]. A basic principle of absorption spectroscopy, the Beer-Lambert Law, provides the fundamental theory for calculating absorption based on light attenuation through a medium [22, 23] and is most commonly seen in the following form [22, 24]:

$$\log_{10} \left(\frac{I_0}{I} \right) = A = l \sum_{i=1}^N c_i \varepsilon_i \quad (1.3)$$

where I_0 is the intensity of incident light, I is the intensity of attenuated light, A is the absorbance measured through the absorbing medium, l is the optical path length through the medium, N is the number of absorbing species within the medium, ε_i is molar extinction coefficient of the i^{th} absorbing species, and c_i is the concentration of each absorbing species. This principle has been applied in many of these instances, including to measure temporal variation of iodine concentration through a gas introduction system [25] and for methane gas plume detection in the environment [26]. Several reviews have been done of atomic spectroscopy methods and the many advancements in the field [27, 28].

1.3.1 Imaging spectroscopy

A popular technique for recording absorption measurements is using an imaging spectrometer. Imaging spectrometry is a growing technology with a wide variety of applications [29]. Historically, when taking spectroscopic measurements, wavelengths were separated into a monochromator, and the intensities at each frequency (wavelength) were registered on a photographic plate [16]. Today, light detection is electronically based, and observed intensities of emitted light are plotted versus wavelength electronically, either as a plot line or captured in an image [16]. Imaging spectrometers allow for a more detailed view of the spectral response of materials across a range of wavelengths at once [20]. The output of an imaging spectrometer is essentially a three-dimensional cube of data: wavelength, position, and intensity, with a sequence of images allowing for time-resolved data [14]. Imaging spectroscopy has been used for a wide range of applications, including but not limited to detecting basal cell carcinomas [30], imaging stellar spectra aboard the Hubble Space Telescope [31], mapping materials on the surface of Saturn's moons [32], measuring reflected solar energy for mapping Earth's surface [33], characterizing soil sample profiles and mapping elemental concentrations in high-resolution [34].

A massive advantage to imaging spectroscopy over other spectroscopic measurement techniques is its ability to perform material identification and characterization remotely and non-destructively [34, 35]. A major application of imaging spectroscopy is hyperspectral remote sensing for Earth science, which uses reflected and emitted energy to measure the physical properties of distant objects and materials [14, 36]. Remote sensing has been widely applied for distant terrestrial measurements and mapping Earth with aerial and space imagery [14]. These measurements have been applied to atmospheric studies, vegetation mapping, snow and ice hydrology [15], and gas tracing for public and environmental health monitoring [37]. As the field of spectroscopy develops, so does the technology used for imaging spectroscopy. Its popularity continues to grow as the instruments used become smaller and less expensive [29, 37].

1.4 Tomographic reconstruction

Tomographic reconstruction refers to the process of recovering spatially resolved information from line-of-sight (LOS) integrated measurements [38]. These techniques are vital to experimental research where LOS integrated measurements are preferred for non-intrusive visualization of complex environments. Tomographic methods are especially useful in optical diagnostics such as absorption spectroscopy and schlieren imaging where the measured signal is an integral over a path length through a medium [39, 40]. Inverting this path-integrated data allows for spatially resolved reconstructions of physical properties such as temperature, pressure, and concentration fields [8]. In particular, when applied

to axisymmetric systems, tomographic reconstruction makes use of mathematical transforms such as the Radon or Abel transform to recover radial profiles from projection data [41]. The diagram in Figure 1.3 depicts the relationship between three-dimensional fields, the measurements taken through them, and the way in which reconstruction techniques can be applied to deconvolve those measurements.

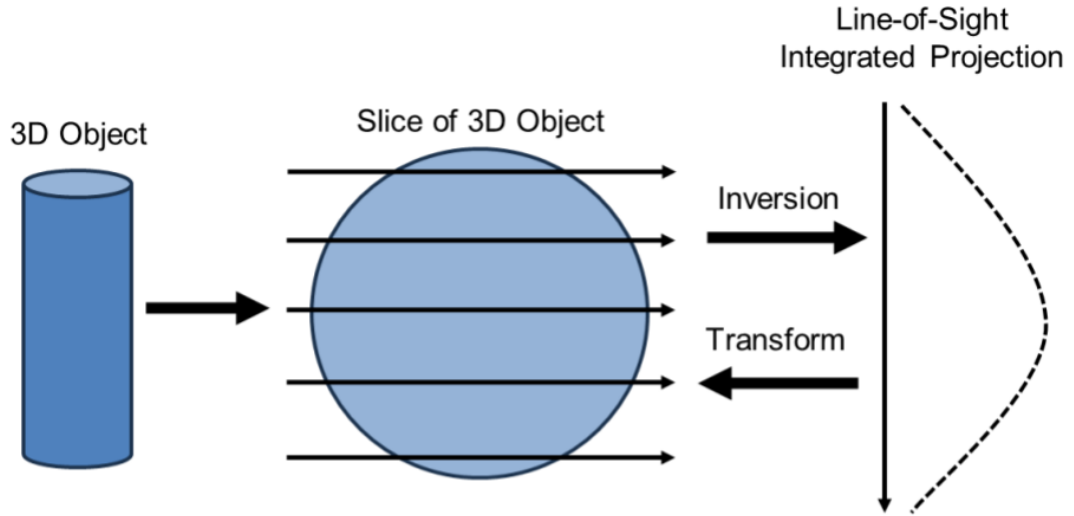


Figure 1.3: Diagram depicting the use of tomographic reconstruction inversions and transforms to deconvolve line of sight measurements.

The Radon transform process is used for reconstruction and deconvolution through three-dimensional objects and flow fields to two-dimensional projections of those objects [38, 42]. It allows for reconstruction from projections taken at arbitrary angles [42]. The Radon transform is generally defined as:

$$R(\theta, s) = \int_{-\infty}^{\infty} f(x \cos \theta + y \sin \theta - s) ds \quad (1.4)$$

where $f(x, y)$ is the scalar field to be reconstructed and $R(\theta, s)$ is the projection of f at angle θ . Unlike the Abel transform, which assumes cylindrical symmetry, the Radon transform can handle arbitrary two or three-dimensional fields [40]. The inverse Radon transform is computationally intensive and sensitive to noise, particularly when the number of angular projections is limited. This problem is common in experimental setups where physical access or optical constraints restrict the number of available views. To address this, regularization techniques such as Tikhonov regularization are commonly applied to stabilize the inversion [42].

Radon-based techniques are particularly relevant in tomographic absorption spectroscopy (TAS), where LOS integrated absorbance measurements are taken at different angles or views to reconstruct temperature and species concentration

fields [40, 43]. In these setups, the Beer-Lambert Law provides a relationship between the absorbance measurements and the target field. The inverse Radon transform has been used in combination with TAS to reconstruct water concentration fields within laminar jets using concentration gradients [40]. It has also been used with time-averaged TAS measurements to recover two-dimensional species fields within turbulent jets [43].

The Abel transform is another integral transform used to convert LOS integrated signals into radial distributions. Abel inversion methods eliminate the need for more than one projection of the field of interest. This makes it especially valuable in applications involving symmetric flame fronts, jets, and shock tubes [8, 39, 44]. Several forms of the Abel inversion have been developed for processing different LOS integrated measurements [41, 45, 46]. However, the various forms of the Abel transform only apply to axisymmetric flow fields [41, 45]. The forward Abel transform is given by [41]:

$$A(x) = 2 \int_r^R \frac{f(r) r}{\sqrt{r^2 - x^2}} dr \quad (1.5)$$

where $A(x)$ is the measured projection along a LOS offset from the axis by a distance x , and $f(r)$ is the unknown radial distribution to be recovered. The corresponding inverse Abel transform is:

$$f(r) = -\frac{1}{\pi} \int_r^R \frac{dA(x) / dx}{\sqrt{x^2 - r^2}} dx \quad (1.6)$$

Due to the integral's singularity at the lower limit $x = r$ [46], various methods of regularization have also been developed to stabilize the results of Abel inversions [45]. The two-point method, for example, approximates $A(x)$ between neighboring measurement locations, pixels in an image, and is known for its robustness against noise propagation [45].

In experimental studies, Abel inversion is widely applied to infer temperature or density profiles from optical diagnostics. In schlieren imaging, the refraction angle of light (ϵ) is first extracted from image intensity gradients and then related to the refractive index gradient using the Gladstone-Dale Law [8]. From this, the LOS-averaged refractive index can be calculated, which is then inverted using the Abel transform to obtain radial distributions of density or temperature [8, 39]. Similar approaches have been used to study shock waves in explosive events [8], where schlieren images are combined with pressure measurements to derive temperature and density fields. The Abel transform has also been used similarly to enable accurate reconstructions of supersonic jet density fields [44]. It has also been applied to the field of TAS, where LOS absorption measurements from axisymmetric flows were deconvolved to obtain temperature and concentration measurements with radial resolution in both uniform and mixed species flows [40].

1.5 Foundational research

The concept of a common path schlieren and imaging spectroscopy setup was first introduced by Smith [47] in 2016 to identify the presence of iodine at the shock fronts produced by Al/I₂O₅ thermite testing. A relative absorption and concentration measurement of the iodine gas at the blast time of arrival within the optical field of view was estimated using the common path imaging technique. This work was continued by Anderson [48] in 2017, who further developed the common path schlieren and imaging spectroscopy setup. The setup was again used to characterize a relative absorbance and concentration of iodine, this time within turbulent plumes with a focus on the presence versus absence of iodine rather than a quantitative measurement. This was applied to the study of turbulent mixing within the explosive post-detonation environment. Further research was recommended in both instances to improve upon the setup for higher accuracy and efficiency for the quantification of chemical species within the flow field of interest.

1.6 Objectives of the present research

It is evident from the existing body of research that an optical technique capable of spectroscopically characterizing mixed-species flow fields while simultaneously visualizing the full flow field has not been demonstrated. The quantitative schlieren technique is fully developed and widely applied for flow field characterization, but lacks the ability to separate the effects of varied chemical species versus density-based refractive gradients. Absorption imaging spectroscopy provides information regarding the concentration of the desired species within the flow field, but lacks the robustness to visualize a large area of a flow field, as well as ease of implementation. The combination of these techniques provides the foundational principles needed to develop a new method of characterization using only a modified schlieren setup, which is more easily applied to a wider range of experimental circumstances. The goal of this work is to advance the understanding of these techniques in combination. This research will be accomplished through experimental studies with the following objectives:

- Further develop the robustness of the common path schlieren and imaging spectroscopy technique for absorption measurements of laminar helium and helium-iodine plumes.
- Experimentally quantify iodine concentrations within laminar helium-iodine plumes.
- Demonstrate the relationship between absorption due to iodine presence and density-based refractive disturbances within the schlieren field of view.
- Develop and experimentally validate a modified schlieren technique for spectroscopic characterization without the use of a spectrometer.

The techniques and analysis methods developed in this work are applied to the specific scenario of a laminar iodine-laden gas plume under ideal conditions. The concepts developed here are intended to provide a foundation for further exploration of larger scale applications and varied species testing in the future.

CHAPTER 2

EXPERIMENTAL METHODS AND TESTING SETUPS

Density reconstruction within a test field of view containing multiple chemical species was a multi-step process requiring various phases of experimental testing and data analysis. The first step was to develop a method of correlating the schlieren technique with absorption spectroscopy using an imaging spectrometer. Gas plumes of known spectral responses, in this case plumes of both pure helium and mixed helium and iodine, were used to examine variations in absorption in the spectrometer. These variations in spectral response were correlated to spatial positions within the schlieren field of view to first show the connection between these two components. The goal of the next section of the research was to resolve similar data to the combined schlieren and spectroscopy setup without the use of an imaging spectrometer. A method of extracting quantitative schlieren data while still accounting for differences caused by mixed gas species was desired.

2.1 Imaging diagnostics for simultaneous schlieren and imaging spectroscopy

The experimental setup utilized for the simultaneous schlieren and imaging spectroscopy section of the research was a combination of both traditional schlieren imaging and imaging spectroscopy. A diagram of the overall structure of this combined setup is provided in Figure 2.1. For the traditional schlieren setup, light from a point source is directed forward into a collimating lens. This creates a region of parallel light in the test section. The light is then refocused by a second lens at the end of the test section. This brings the light back down to a focal point, where a knife edge is then placed in either a horizontal or vertical orientation perpendicular to the direction of light travel. This creates the schlieren effect in the light moving into a camera of the user's choice. Two 700 mm focal length schlieren lenses were used to visualize the events of these experiments (SL1 and SL2).

A beam splitter (BS) was placed before the focal point of the light exiting the test section. This beam splitter was a 50-50 splitter which passed half of the light and reflected the other half at a 90° angle. This was done so that light from the same test section could be viewed by two different cameras. A vertical knife edge (KE) was placed at the focal point of the light turned 90° off the direct schlieren imaging path. The schlieren field of view was captured by a Photron Mini-UX high-speed camera (C1). The camera was run with a frame rate of 2000 frames

per second (fps) and an exposure of 1.11 microseconds. The light directed straight forward was first recollimated by a 60 mm focal length lens (CL) before entering into the front entrance slit of the imaging spectrometer (SPECT). The entrance slit was set to approximately 1 mm in height and maintained its fixed 8 mm in width. The light exited through the spectrometer's rear port and was immediately refocused by a 75 mm focal length lens (FL) before being captured by a Photron Nova S12 high-speed camera (C2). This camera was also operated at 2000 fps with an exposure of 14.3 microseconds. The various elements of this imaging diagnostics setup are displayed in Figure 2.2 a and b.

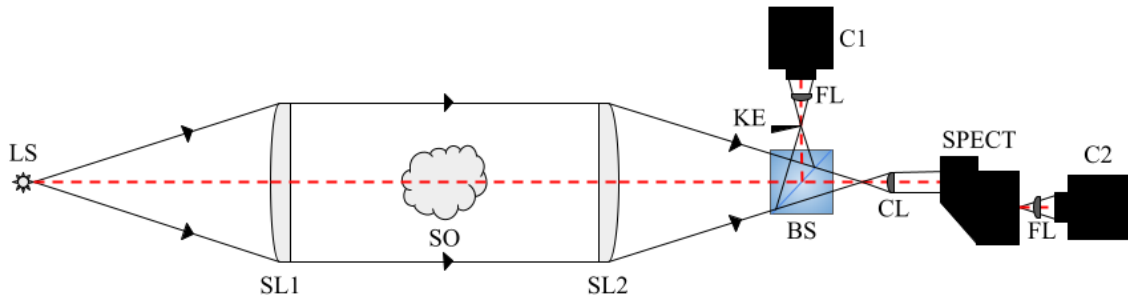


Figure 2.1: Setup diagram for simultaneous schlieren and imaging spectroscopy. See text and nomenclature listings for detailed description.

It should be noted that a shadowgraph effect was produced in the spectrometer images. Shadowgraphy visualizes the second spatial derivative (Laplacian) of the refractive index field [3]. This effect is unavoidable with the parallel arrangement and the refractive index variations within the plume.

2.1.1 Imaging spectrometer

For this work, a Horiba MicroHR imaging spectrometer (labeled "SPECT" in Figure 2.1) was used. The Horiba MicroHR is a Czerny-Turner style imaging spectrometer. The Czerny-Turner spectrometer style resolves the spectral intensity of radiation imaged across a spatial dimension. It is a widely used style for fluorescence analysis, atmospheric remote sensing, ultra-short pulse measurement, and stand-off detection of biological agents due to its flexibility and effectiveness in dispersing light over a broad spectral range [49, 50]. Spectrometers of this style are typically designed with two concave mirrors and a rotatable plane diffraction grating to achieve high spectral resolution. Light entering through an entrance slit is collimated, dispersed, and refocused onto a detector by a focusing mirror [49, 50]. In this case the detector is a high-speed camera positioned at the exit of the spectrometer. A schematic of a typical Czerny-Turner spectrometer setup is provided in Figure 2.3.

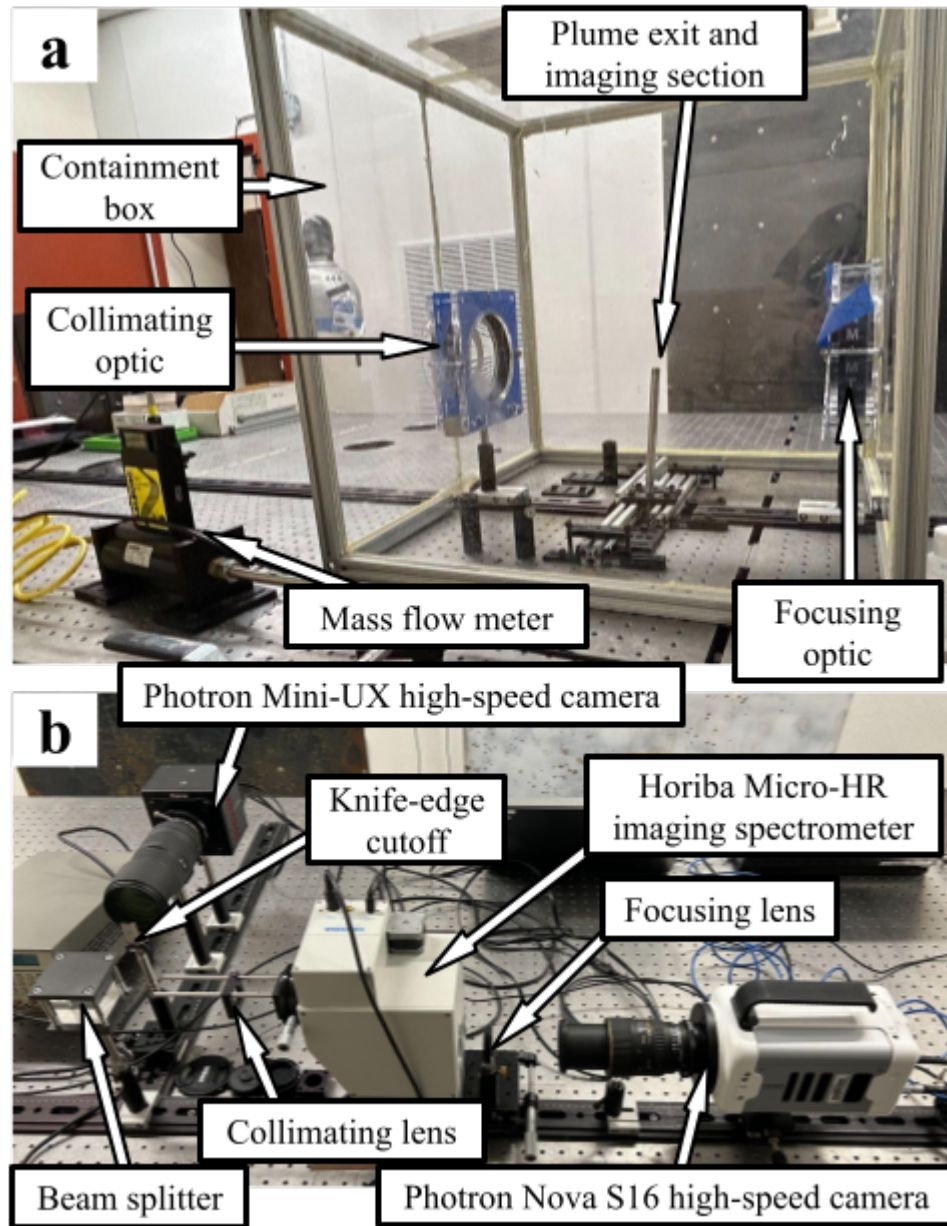


Figure 2.2: Experimental setup images for simultaneous schlieren and imaging spectroscopy: (a) iodine containment box with test section and optics, and (b) optical diagnostics setup. See text and nomenclature listings for detailed description.

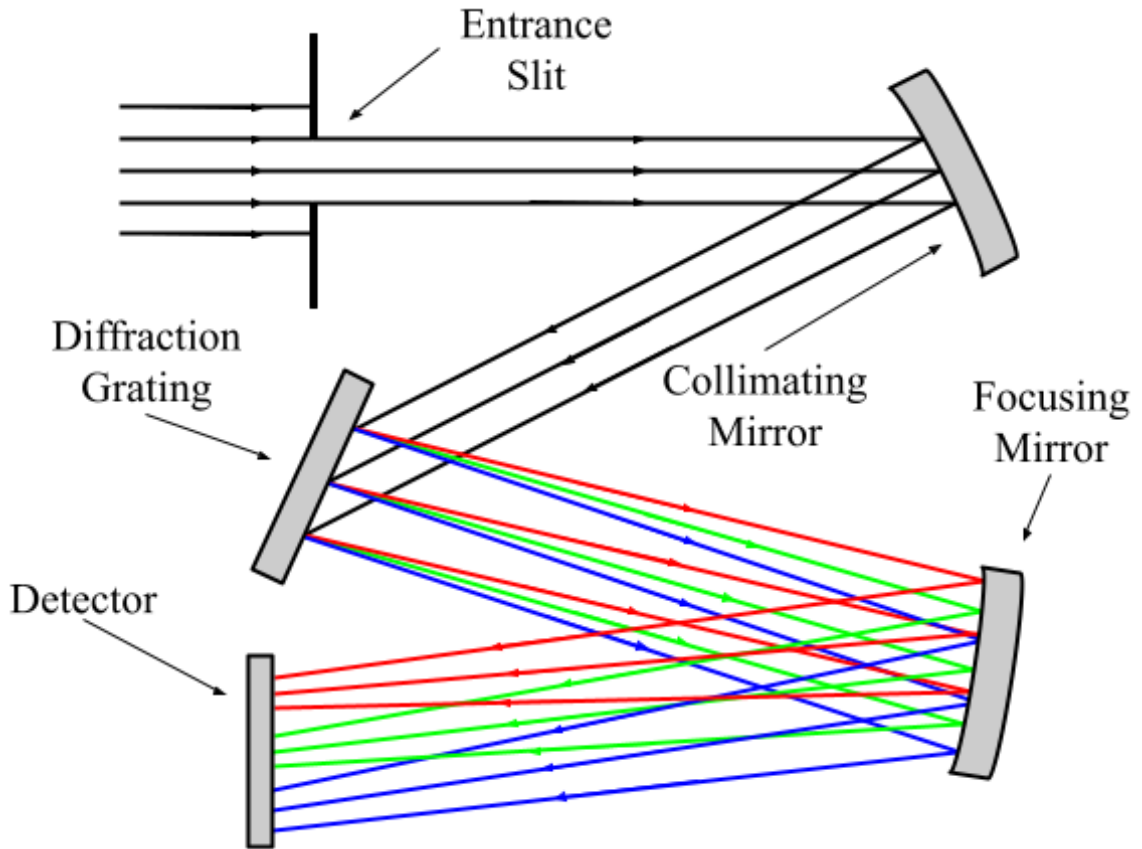


Figure 2.3: Schematic of internal setup of typical Czerny-Turner style imaging spectrometer.

One of the major advantages to the Czerny-Turner style is its ability to correct for coma aberrations through a symmetrical mirror arrangement. This improves image quality and therefore spectral accuracy. However, conventional Czerny-Turner designs suffer from astigmatism due to the off-axis positioning of the mirrors. This can degrade the overall performance when using a linear detector array [51]. Certain trade-offs therefore exist when using this spectrometer style. A lower f-number of the system increases light collection efficiency, however, it may also introduce additional aberrations. Additional care must therefore be used during the calibration and component alignment steps of using the spectrometer [50]. When using the Horiba MicroHR imaging spectrometer, additional considerations for data collection included optimizing the entrance slit width, ensuring proper grating selection for the desired wavelength range, and correcting for variations in instrument and camera response, which is discussed later. Environmental factors such as changes in temperature and mechanical vibrations were minimized to ensure as much measurement stability as possible. The Horiba MicroHR was equipped with grating 51019. This grating has 300 grooves per millimeter, a blaze wavelength of 600 nm, and a blaze angle of $5^{\circ}10'$. The recommended range of

wavelengths for this grating is 350-1300 nm. The resolution is approximately 500 at the wavelengths of interest for this work. The spectrometer was also equipped with a vertical entrance slit. For the purpose of this work, a horizontal entrance slit was required. Therefore, the Horiba MicroHR was rotated by 90° to accommodate the vertical flow direction of gas plumes through the field of view.

2.2 Imaging diagnostics for color-filtered schlieren

The experimental setup used for the color-filtered schlieren section of the research was similar to the setup used for simultaneous schlieren and imaging spectroscopy. However, as shown in Figure 2.4, the imaging spectrometer was removed and was replaced with a second Photron Nova S12. This allowed for two simultaneous views of the same schlieren test section. It should be noted that the cameras were independently focused. It should also be noted that the schlieren lenses served as the stops of the system. No additional stops or baffles were required inside the camera or lenses.

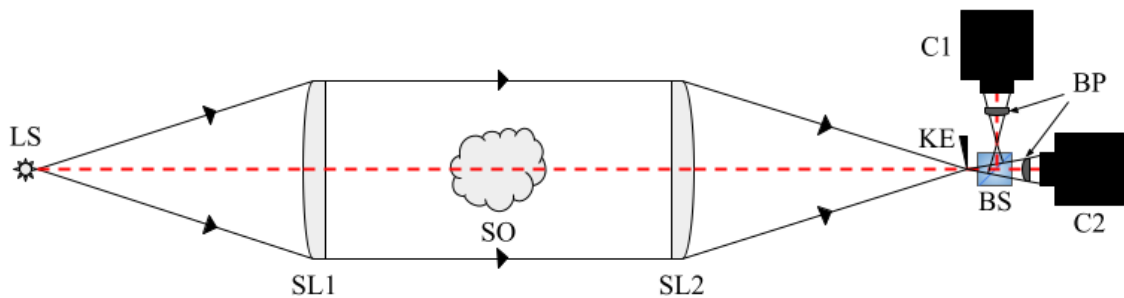


Figure 2.4: Setup diagram for simultaneous color-filtered schlieren. See text and nomenclature listings for detailed description.

Another change to the system was in the positioning of the knife edge (KE). The data analysis for this section of the research was heavily reliant on the quantitative schlieren methods, where it was ideal to have the same amount of knife edge cut-off in both views to reduce the amount of error introduced during the quantitative schlieren calibration process. In order to do this, a single knife edge was placed at the focal point of the light exiting the test section. The beam splitter (BS) was then placed after the knife edge instead of before it. This ensured the same cut-off light was observed by both cameras.

Immediately after the beam splitter, a color bandpass filter (BP) was placed before each camera. The wavelengths of these filters were the same wavelengths of interest: 530 nm and 650 nm. The selection of these wavelengths is discussed later. The filters used were produced by ThorLabs (part number FKB-VIS-10).

Filtering each camera at these wavelengths meant only changes at those individual wavelengths within the field of view would be visualized. In theory, the changes viewed at each wavelength would differ under the influence of iodine gas due to its absorption peak existing at the 530 nm interest point, whereas a helium-only plume would show no significant differences between the two wavelength views due to its lack of significant absorption at either 530 nm or 650 nm. This is discussed in more detail later.

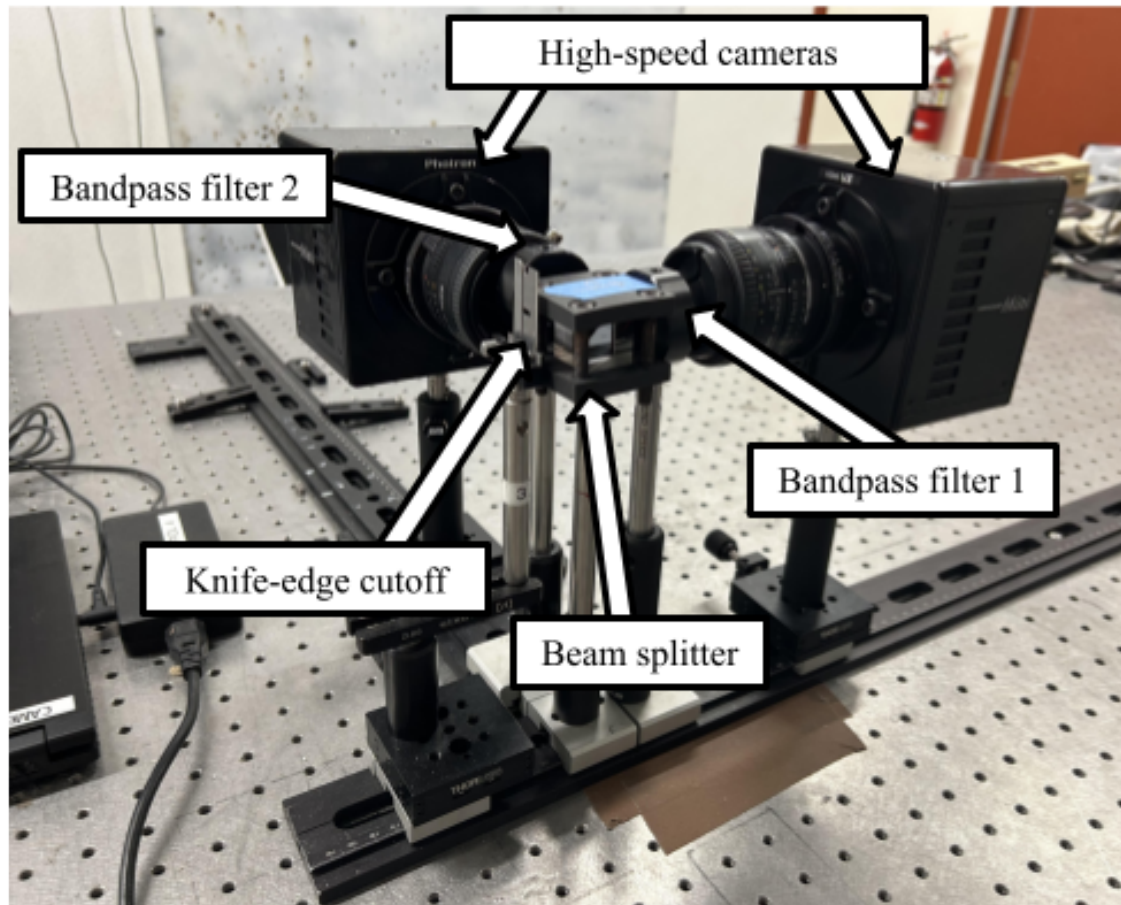


Figure 2.5: Optical diagnostics experimental setup images for color-filtered schlieren. See text and nomenclature listings for detailed description.

While color cameras could in theory be used for this application, monochrome cameras were exclusively used. This was done in order to limit the amount of error introduced by the camera itself due to the drop in resolution caused by the Bayer filter, which only allows each pixel to capture intensities for one color channel (red, green, or blue) as opposed to capturing an overall intensity value [52].

2.3 Light source

A SugarCube LED was used as the light source (LS) of the experimental setups. The SugarCube was chosen due to both its ease of use as well as its well-characterized spectral output, which is available upon request to the vendor (part #66-032 purchased through Edmund Optics). The spectral output is shown in Figure 2.6. This provided information regarding the expected background intensities at each wavelength of the light source for comparison to intensity values during testing. The SugarCube also had sufficient intensities at the two wavelengths of particular interest for this work, which were 530 nm and 650 nm, and are displayed in Figure 2.6 and will be discussed later.

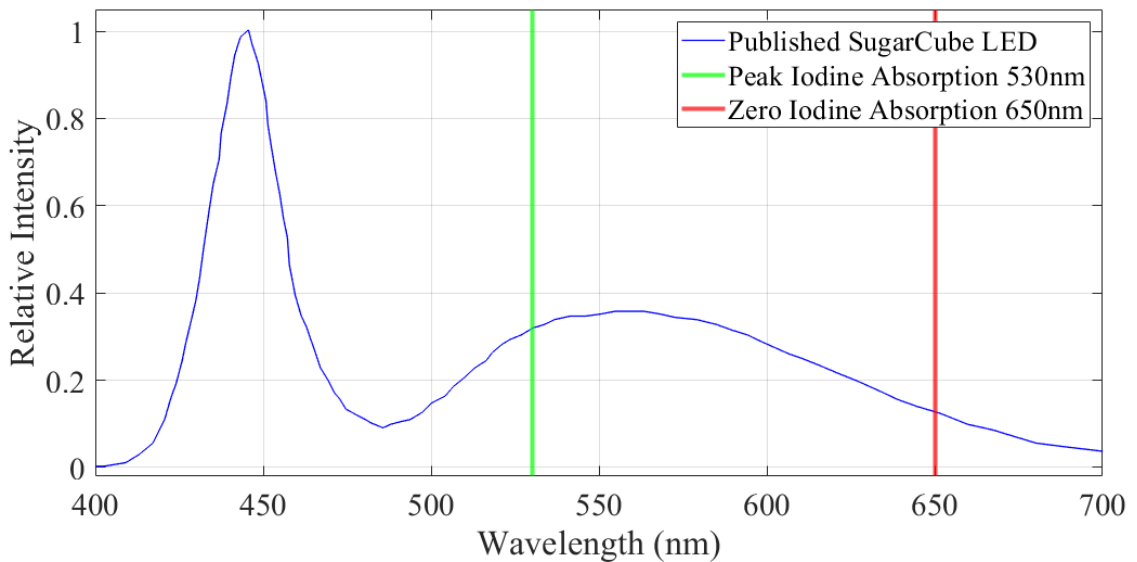


Figure 2.6: Plot of manufacturer provided SugarCube LED spectral output.

2.4 Camera syncing and triggering

During each experiment, two cameras were used to image events from the same test section field of view simultaneously. A goal of the data processing was to correlate the information extracted from one camera to the information extracted from the other. Because of this, it was crucial for the cameras to be synchronized during data capture.

In order to consistently capture synchronized data with the two cameras in the combined schlieren and spectroscopy setup, an external trigger source was used. A Stanford Research Systems (SRS) DG535 Delay Generator was used to send an initial external single trigger signal to both cameras. A wiring diagram of this camera triggering setup is shown in Figure 2.7. For later color-filtered

schlieren testing performed with matching cameras, the matched cameras were synced and triggered through the Photron PVF4 software. Image capture was triggered before the plume entered the test section, so the timestamp of the first visualization could be correlated to ensure simultaneous imaging between the two cameras.

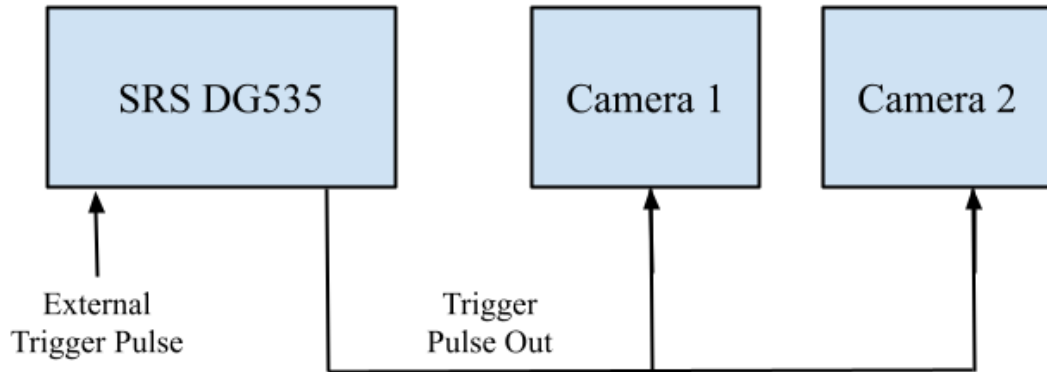


Figure 2.7: Schematic for camera triggering during simultaneous schlieren and imaging spectroscopy testing.

2.5 Chemical selection

Iodine was selected as the chemical of choice for this research because of its well-characterized and previously documented absorption spectrum. Several studies have been done using iodine gas as the medium of interest for absorption spectroscopy measurements, largely for the application of atmospheric and marine science [25, 28]. Figure 2.8 depicts the absorption profile as characterized by Tellinghuisen [53] and Saiz-Lopez [54]. Figure 2.8 shows the iodine gas absorption spectrum corresponding to the $B \leftarrow X$ electronic transition as described by Tellinghuisen, who focused on resolving the visible-infrared absorption spectrum of iodine into its contributing electronic transitions. This work provided insights into the peak absorption of iodine around approximately 530 nm. Also included is the iodine gas absorption spectrum as described by Saiz-Lopez, who aimed to determine the absolute absorption cross-section of iodine by conducting tests at room temperature (295 K) and standard atmospheric pressure (760 Torr) across wavelengths ranging from 182 nm to 750 nm. The results of this work aligned well with the findings of Tellinghuisen in 1973.

Iodine's absorption spectrum has a peak between approximately 520 nm and 530 nm. This peak absorption wavelength was of interest here and is depicted on Figure 2.8 in green since it presents as green on the visible light spectrum. Another

wavelength of interest was 650 nm, which is red on the visible light spectrum and is depicted in red on Figure 2.8. This was of interest as a region of negligible absorption on the iodine spectrum.

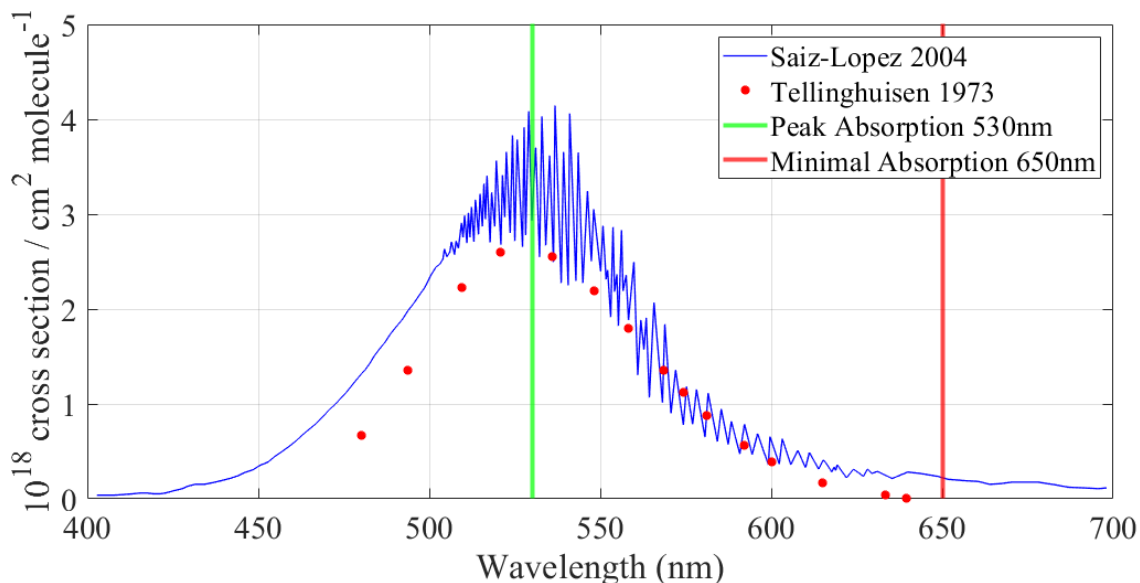


Figure 2.8: Digital recreation of iodine spectral response found by Tellinghuisen (1973) and Saiz-Lopez (2004). Curves normalized for comparison.

In addition to having well-characterized properties, iodine gas is also clearly visible to the naked eye. When heated to its gaseous state, it presents itself with a bright purple hue that is clearly distinguishable against the surrounding air and background. This property made iodine ideal for performing this experimentation so that its presence could be consistently verified by eye. Iodine is a solid at room temperature. A small amount of the solid grains was measured as needed for each individual experiment and ranged from 0.1 g to 1.5 g, depending on the desired iodine concentration level within the plume. The iodine used here was pharmaceutical-grade re-sublimed iodine crystals produced by Mallinckrodt Chemical Works.

Helium gas is optically clear and invisible to the naked eye. It has a small number of distinct but weak absorption lines in the visible spectrum. The most prominent visible absorption lines of neutral helium occur at 447.1 nm, 501.6 nm, 587.6 nm, and 667.8 nm, as documented in the NIST Atomic Spectra Database [55]. These bands, however, are significantly weaker than those of iodine. Helium's dominant absorption also occurs in the far-UV spectrum, not in the visible range where iodine's absorption peaks strongly. Regardless of strength, helium's absorption bands do not directly overlap with those of iodine. The bandpass filters used for this work also have a narrow enough bandwidth that overlap between the absorption bands of helium and iodine was not a concern. Helium and iodine also do not react with each other. Therefore, helium gas was an ideal candidate to carry



Figure 2.9: Solid iodine grains used in experimental testing.

iodine gas into the test section without disrupting or distorting light absorbance at iodine's wavelengths of interest and to provide a baseline for comparison of assumed zero absorption.

2.6 Gas introduction setup

The method of introducing both pure helium and mixed helium-iodine gas plumes into the test section consisted of a series of 9 mm (3/8") internal diameter stainless steel pipes. These were positioned to deliver helium directly from a helium tank through a mass flow meter to monitor the flow velocity during testing. This can be seen in Figure 2.10a. To measure the flow of helium through the system, an Aalborg Mass Flow Meter was used. This measured gas flow in units of L/min and was calibrated specifically to measure helium flow between 0 and 500 L/min. A goal during testing was to observe laminar gas plumes rather than turbulent plumes. This was to reduce the amount of light variation caused by

plume disturbances versus differences in gas species. Determination of gas flow and the laminar status of each plume is discussed later.

After passing through the mass flow meter, a valve was positioned to direct the helium flow in one of two directions. The first path directed the helium directly into the test section. This was used for creating pure helium-only plumes in the test section. The second path directed the helium through the iodine heating chamber. This heating chamber was used for placing solid iodine particles at the start of an experiment. Once the particles were placed in the chamber, the chamber was sealed and heated from the outside until the internal temperature reached above 185° Celsius (363° Fahrenheit), the vaporization temperature of solid iodine. The chamber itself is shown in Figure 2.10b. Once the iodine was vaporized, the helium was passed through the chamber to mix and carry iodine gas up into the test section in the same manner and position as the helium-only plume. An acrylic box was built to contain the test section and gases moving through the test section. This box had holes cut for the schlieren lenses to be fitted into and sealed around. The box was also used to minimize the amount of plume disturbances due to air currents within the testing room so that steady laminar plumes could be visualized more clearly. A ventilation fan was attached at the top of the box to promptly remove iodine gas following each test to prevent contamination of equipment and the surrounding area, as well as to prevent inhalation or excessive contact.

2.6.1 Plume flow rates

Laminar flow was desired for each gas plume visualized within the test section because of its natural symmetry. Turbulent flow exhibits many fluctuations in flow characteristics. The lack of symmetry within turbulent flow prohibits the use of the Abel inversion transform, therefore severely limiting the capabilities of data processing using existing methods. This also means that a baseline theoretical profile cannot be determined because the baseline is constantly changing with the turbulent features. A clean, symmetric flow is ideal for the extraction of data. To achieve consistent laminar features, the range of allowable gas flow rates was calculated. This range was used to determine whether the values measured by the mass flow meter were acceptable during each plume test.

As a general rule, pipe flow with a Reynolds number (Re) between 20 and 200 is considered to be fully laminar [56, 57]. For a similar setup to the one used here with a pipe exit diameter of 9 mm, fully laminar jet behavior was observed for Reynolds numbers up to 600 [58]. First, the density of the helium gas at the testing environment conditions was calculated using the ideal gas law:

$$\rho_{He} = \frac{P_{atm} \cdot M_{He}}{R_u \cdot T_{plume}} = 0.1407 \text{ kg/m}^3 \quad (2.1)$$

where P_{atm} was the atmospheric pressure in Pa, M_{He} was the molar mass of helium gas ($4.003 \cdot 10^{-3}$ kg/mol), R_u was the universal gas constant (8.3145 J/mol · K),

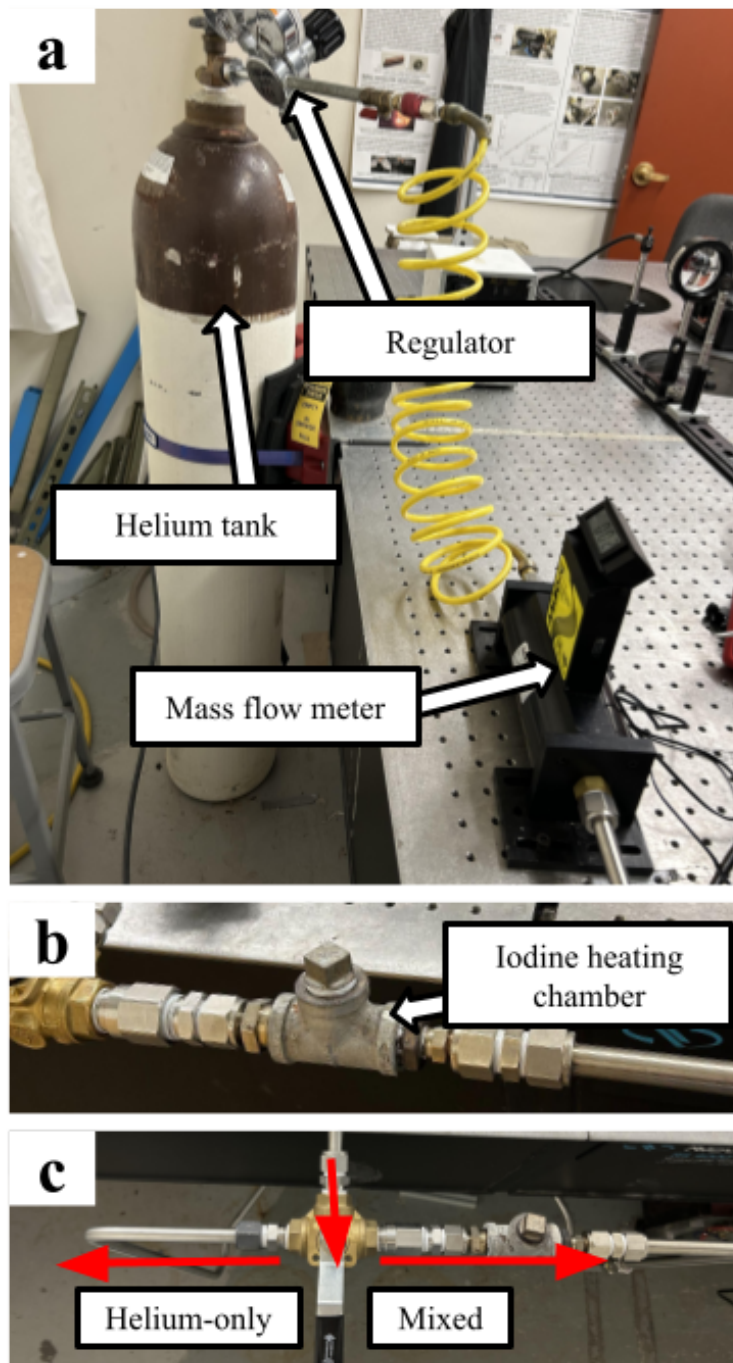


Figure 2.10: Experimental setup images for gas introduction setup: (a) helium gas introduction system overview, (b) iodine heating chamber, and (c) directional valve for switching between pure helium plumes and mixed helium-iodine plumes.

and T_{plume} was the average helium plume temperature previously determined (293.15 K).

The relationship between Reynolds number and other variables describing the flow exiting the pipe is:

$$Re = \frac{\rho \cdot V \cdot d_{pipe}}{\mu} \quad (2.2)$$

where ρ is the density of the helium gas, V is the flow velocity, d_{pipe} is the inner diameter of the pipe, and μ is the dynamic viscosity of helium gas. At the testing temperature and pressure conditions, μ_{He} is $1.96 \cdot 10^{-5}$ kg/m · s. After rearranging Equation 2.2, and using these values with a minimum Re of 20 and a maximum Re of 600 for laminar flow, the minimum and maximum flow velocities for laminar helium flow in this pipe system were calculated as follows:

$$V_{min} = \frac{Re_{min} \cdot \mu_{He}}{\rho_{He} \cdot d_{pipe}} = 0.3 \text{ m/s} \quad (2.3)$$

$$V_{max} = \frac{Re_{max} \cdot \mu_{He}}{\rho_{He} \cdot d_{pipe}} = 9 \text{ m/s} \quad (2.4)$$

From there, the volumetric flow rates, Q , associated with the minimum and maximum flow velocities were calculated by factoring in the cross-sectional area of the pipe:

$$A_{pipe} = \pi \left(\frac{d_{pipe}}{2} \right)^2 = 6 \cdot 10^{-5} \text{ m}^2 \quad (2.5)$$

$$Q_{min} = V_{min} \cdot A_{pipe} = 2 \cdot 10^{-5} \text{ m}^3/\text{s} = 1 \text{ L/min} \quad (2.6)$$

$$Q_{max} = V_{max} \cdot A_{pipe} = 6 \cdot 10^{-4} \text{ m}^3/\text{s} = 35 \text{ L/min} \quad (2.7)$$

As validation, a second method of calculating the desired volumetric flow rate was used [58]:

$$Re = \frac{4Q}{\pi \cdot v \cdot d_{pipe}} \quad (2.8)$$

where v is the kinematic viscosity of helium gas. This was calculated using the following equation [57]:

$$v_{He} = \frac{\mu_{He}}{\rho_{He}} = 14 \cdot 10^{-5} \text{ m}^2/\text{s} \quad (2.9)$$

Using the same maximum and minimum values of Re as above, the maximum and minimum volumetric flow rates for laminar jet behavior were calculated again:

$$Q_{min} = \frac{Re_{min} \cdot \pi \cdot v_{He} \cdot d_{pipe}}{4} = 2 \cdot 10^{-5} \text{ m}^3/\text{s} = 1 \text{ L/min} \quad (2.10)$$

$$Q_{max} = \frac{Re_{max} \cdot \pi \cdot v_{He} \cdot d_{pipe}}{4} = 6 \cdot 10^{-4} \text{ m}^3/\text{s} = 35 \text{ L/min} \quad (2.11)$$

Therefore, it was determined that flow rates measured between 1 L/min and 35 L/min on the mass flow meter were appropriate and usable for data processing. To avoid using flow rates outside the acceptable range during testing, the flow rate was set between 5 L/min and 30 L/min. Any tests performed where the flow rate reading rose above 30 L/min or dipped below 5 L/min were not used for data processing.

2.6.2 Plume temperatures

The temperature of the testing environment was measured for each data set. The temperature within the gas plume itself was more difficult to measure. Taking temperature measurements inside the plume during testing would have created unwanted disturbances within the plume. Therefore, measurements of several plumes were taken and averaged to better predict the conditions of each plume used for the final data processing.

Temperature measurements were taken using an AMPROBE AM-530 multimeter with an attached thermocouple. Before taking measurements inside any plumes, the thermocouple was set to rest for several minutes to acclimate to room temperature. This was also done between each plume test to ensure the testing environment had not changed significantly over time. The temperature was checked every 30 seconds over several minutes and the readings were averaged together. The room temperature measured before each plume test is recorded alongside the plume temperatures in the following tables.

To measure temperatures within the plumes, the end of the thermocouple was positioned at different locations within the gas plume. The two locations of the greatest interest were immediately above the pipe exit and approximately 40 mm above the pipe exit. These two locations were chosen to compare the plume temperature immediately upon entry into the test section and the temperature after traveling a significant way into the test section and reaching the main field of view of interest. The thermocouple was positioned using the schlieren imaging system to visually confirm it was centered in the flow. Examples of the thermocouple positioned in a helium plume are provided in Figure 2.11.

For the pure helium plumes tested, the thermocouple was positioned inside the plume and left for approximately 20 seconds to ensure the thermocouple

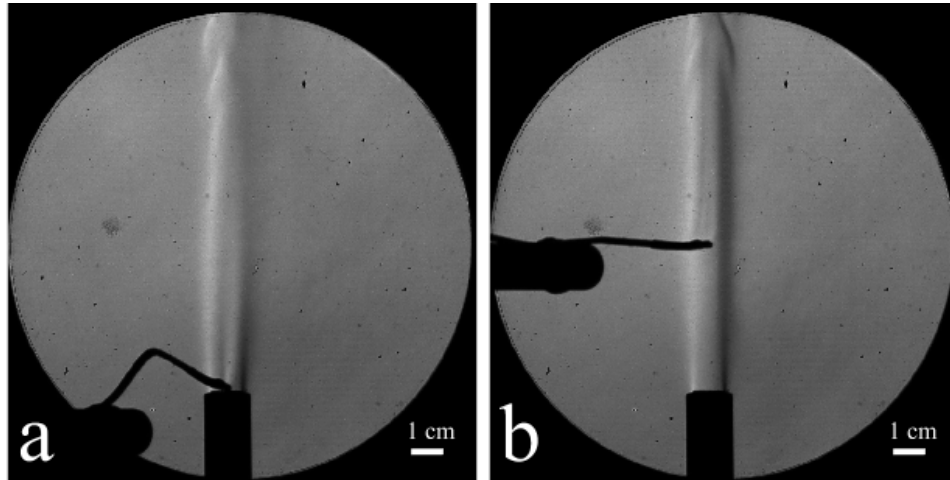


Figure 2.11: Example of thermocouple positioning within a pure helium plume for temperature measurements: (a) thermocouple positioned immediately above pipe exit, and (b) thermocouple positioned 40 mm above pipe exit.

reached a steady temperature reading at the desired flow rate. Each flow rate was tested six times and the values measured were averaged together. This was done for a range of flow rates as described in Table 2.1 at the two positions of interest. The gas flow was turned off and the thermocouple was allowed to re-acclimate to room temperature between each test. Measurements were also taken over a range of testing days to compare the relationship between ambient and plume temperatures.

For mixed helium-iodine plumes, temperature measurements were slightly more complicated. There was a limited amount of iodine in the heating chamber for each test, therefore, the temperature change caused by the introduction of that iodine was not maintainable over a long period of time for long-term measurement the way the helium plumes could be maintained. Instead, a larger number of short tests were run and the values measured were averaged together. The same two thermocouple positions were chosen as for the pure helium plumes. The thermocouple was again allowed to re-acclimate between tests. The same amount of solid iodine was placed in the chamber for each test and it was heated for the same amount of time each test. The results of mixed plume temperature testing is shown in Table 2.2. Again, measurements were taken over a range of testing days.

For both cases, pure helium and mixed helium-iodine, the flow rates used ranged between the minimum and maximum flow rates previously calculated in Section 2.6.1 and increased in increments of 5 L/min. The lowest flow rate was set to 10 L/min instead of 5 L/min because plumes observed at 5 L/min were especially weak and prone to disturbances due to air movement within the testing environment. The maximum flow rate was set to 30 L/min. A very small amount of variation was observed in the overall plume temperatures over a range of testing days. While a noticeable rise in temperature was expected in the

presence of heated iodine, the concentration of iodine within each plume was low enough that it did not cause significant measurable differences with the current setup. These concentration measurements are discussed at length later.

Table 2.1: Helium plume temperatures.

Height Above Pipe Exit (mm)	Average Flow Rate (L/min)	Average Room Temperature (C)	Average Plume Temperature (C)
5	10	20.5	19.7
5	15	19.9	19.4
5	20	20.0	20.0
5	25	20.1	19.4
5	30	20.0	19.3
40	10	20.0	19.3
40	15	20.0	19.1
40	20	19.9	19.6
40	25	19.9	19.6
40	30	20.0	19.8

Table 2.2: Mixed helium-iodine plume temperatures.

Height Above Pipe Exit (mm)	Average Flow Rate (L/min)	Average Room Temperature (C)	Average Plume Temperature (C)
5	10	21.0	23.0
5	15	21.4	21.2
5	20	21.0	20.4
5	25	21.1	20.1
5	30	21.4	20.7
40	10	21.2	21.4
40	15	21.1	19.3
40	20	21.0	19.1
40	25	20.9	18.5
40	30	20.9	18.1

CHAPTER 3

SYSTEM CALIBRATION AND IMAGE PROCESSING METHODS

Image processing was used to quantify the behavior of gas plumes as imaged through the schlieren system as well as by the imaging spectrometer. Quantitative information was extracted from the images using various MATLAB image processing techniques. The first step taken for each data set before any other processing steps were performed was to normalize each image by the bit depth of the image so that all pixel intensity values were ranged between 0 and 1. Following that, data taken from the schlieren system and the imaging spectrometer required individual separate calibration steps. These steps were followed by image registration steps to correlate one view to the other.

3.1 Background subtraction

Background subtraction is performed on each image taken of the field of view to remove any noise due to the camera sensor or particulates that may have been on the camera lens without knowing. To perform the background subtraction, an image of the empty test section was recorded before any flow was introduced (the "background" test section) without moving any of the data collection equipment. If the camera being used has a significant amount of variable pixel noise, several background images can be taken to create an average of that variable noise.

For schlieren images, after obtaining the background image, an average pixel intensity value of the test section background was determined. This was done by creating a binary mask of the background image where only pixel intensity values within the schlieren field of view were taken into account. These intensities were then averaged to determine an average background intensity value throughout the field of view. A simple image subtraction could then be performed to subtract the original background image from any desired test image. The average background value was then added back to the test image to return the appropriate background lighting to the image. An example of a schlieren test image before and after this process is provided in Figure 3.1.

A similar background subtraction process was performed on images captured through the spectrometer. However, unlike the schlieren images, the background

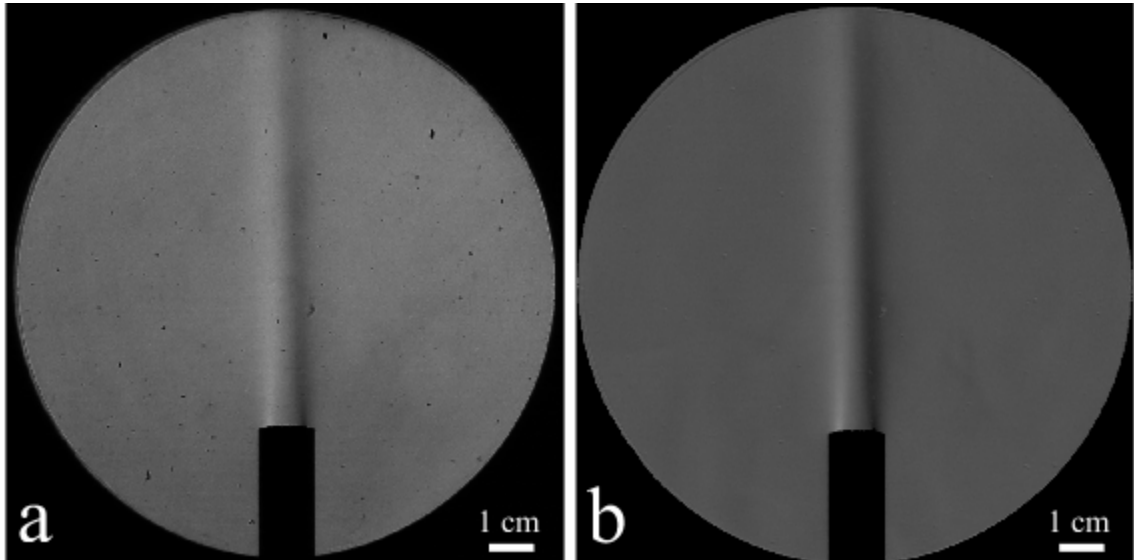


Figure 3.1: (a) Schlieren field of view before performing background subtraction. (b) Same field of view after background subtraction. It should be noted that the background is more uniform and specks on the lens have been removed.

was not one uniform intensity. Each wavelength of light captured in the image had a different average pixel intensity. Therefore, an artificial background image was created by averaging several spectrum background images together, and then taking the average value of each row in the spectrum to approximate the expected pixel intensity at each wavelength along the vertical axis. These row averages were then used to build an image of the same size as each test image. The original background image was subtracted from any desired test image, and the artificial background image was added back to the test image to return the appropriate background lighting at each wavelength. An example of a spectrometer test image before and after this process, along with the artificial background created for the background subtraction process, is provided in Figure 3.2.

3.2 Distance and sizing calibration

A simple length scale calibration of both the schlieren and imaging spectrometer data was performed for each individual test series. This was done by relating the length scale within an image in number of pixels to the length scale of a physical object of known dimensions. The chosen calibration object was placed into the test section and imaged, as pictured in Figure 3.3a, to extract the length scale relation. The main calibration object of choice was a lens holder with a known outer diameter of 45.0 mm. The lens holder was rotated in the test section so that its width in pixels was maximized when facing the camera head-on, indicating

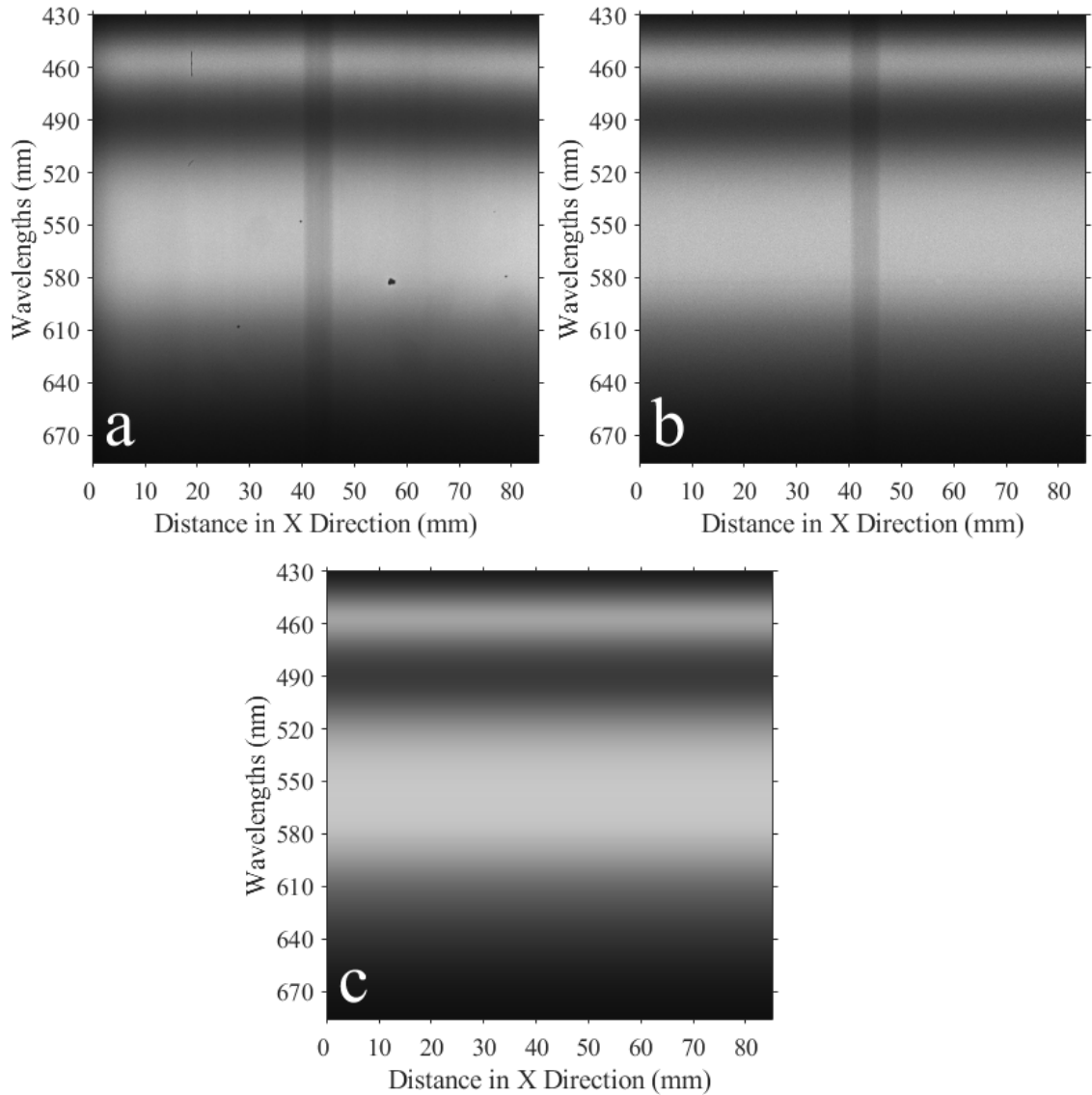


Figure 3.2: (a) Spectrometer field of view before performing background subtraction. (b) Same field of view after background subtraction. It should be noted that the background is more uniform along the horizontal axis and specks on the lens have been removed. (c) Artificial background image created to perform background subtraction.

that it was aligned perpendicular to the camera's cone angle. This provided the most accurate distance calibration possible.

MATLAB was used to find the outer boundary of the lens holder in the image. Specifically, the MATLAB function *imfindcircles* was used for this purpose. The resulting boundary detected is shown in Figure 3.3b. A straight line across that

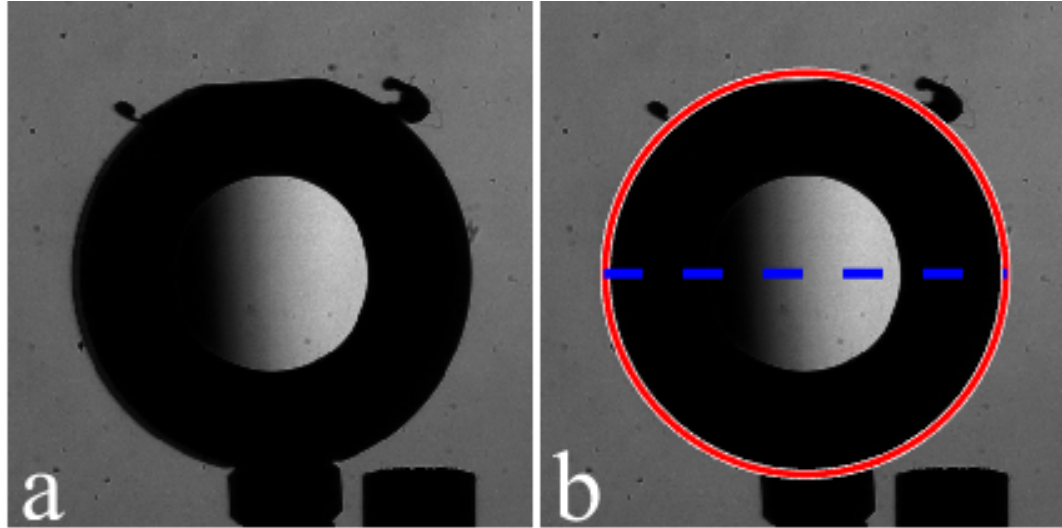


Figure 3.3: (a) Calibration lens holder in schlieren field of view for determining pixel to length ratio in images. (b) Outer boundary of calibration item (red) and center-line across for distance measurement (blue) determined from image processing. It should be noted that the boundary is drawn several pixels wide for visualization, but the true boundary used for measurement was a single pixel wide.

boundary circle was then taken to determine the number of pixels in the image equivalent to the physical length across the diameter of the lens holder. The MATLAB function *imfindcircles* outputs the boundary circle's radius and center point. The radius was doubled and used to calculate a pixel-to-mm distance calibration factor.

$$\text{Calibration Distance} = \frac{\text{Number of Pixels}}{\text{Object Length (mm)}} \quad (3.1)$$

A similar process was used to determine a distance calibration factor in the imaging spectrometer data. The lens holder was not a prime option in these images because the curved surface of the lens holder made it difficult to resolve an exact boundary from the spectral images. For that reason, a calibration object with straight edges was desired, and an optical post was used. Rather than using a circle detection function, the edges of the optical post were found, and the distance between them was measured for use in Equation 3.1.

Proper image calibration was important to avoid the introduction of excessive uncertainties in data processing. For this step of the calibration process, as a general rule, the uncertainty in the images was quantified as approximately 1 pixel based on the input parameter ranges of the MATLAB boundary detection functions. For each of the length scale calibrations determined, the uncertainty

was relatively small compared to the measurement. Tables 3.1 and 3.2 detail some of those distance calibrations made for one example data set of schlieren and spectrometer images, respectively.

Table 3.1: Calibration distances and corresponding uncertainties for images captured through schlieren.

Calibration Item	Distance (pix)	Distance (mm)	Scale Factor (mm/pix)	Uncertainty (mm/pix)
Optical Post	95	12.7	0.1337	0.0014
Wedge Block	442	59.63	0.1349	0.0003
Calibration Lens	333	45.0	0.1351	0.0004
Ball Bearing	375	50.8	0.1355	0.0003

Table 3.2: Calibration distances and corresponding uncertainties for images captured through spectrometer.

Calibration Item	Distance (pix)	Distance (mm)	Scale Factor (mm/pix)	Uncertainty (mm/pix)
Optical Post	74	12.7	0.1716	0.0023
Wedge Block	334	59.63	0.1785	0.0005

3.3 Image registration

While both cameras in the color-filtered schlieren setup view light from the same test section as previously described, there were slight discrepancies in alignment, meaning the field of view of the schlieren was not perfectly aligned in the exact same location between the two camera sensors.

In order to correct for the differences in sensor alignment, the MATLAB function *imregister* was used. This function reads two input images, a fixed (reference) image and a moving image that will be altered to match the fixed image. The function defines the quantitative measure of similarity between the two images, then optimizes that similarity and determines the best transformation process to perform and outputs the final registered image. Figure 3.4 depicts the difference in the data before and after performing the image registration process. It should be noted that the colors seen in Figure 3.4 are used to more clearly visualize the difference in the data correlation before versus after image registration. The

two colors used are automatically chosen by the MATLAB *imshowpair* function, which was used to show the frames overlaid in the figure. These two colors do not correspond to the wavelengths the data was captured at.

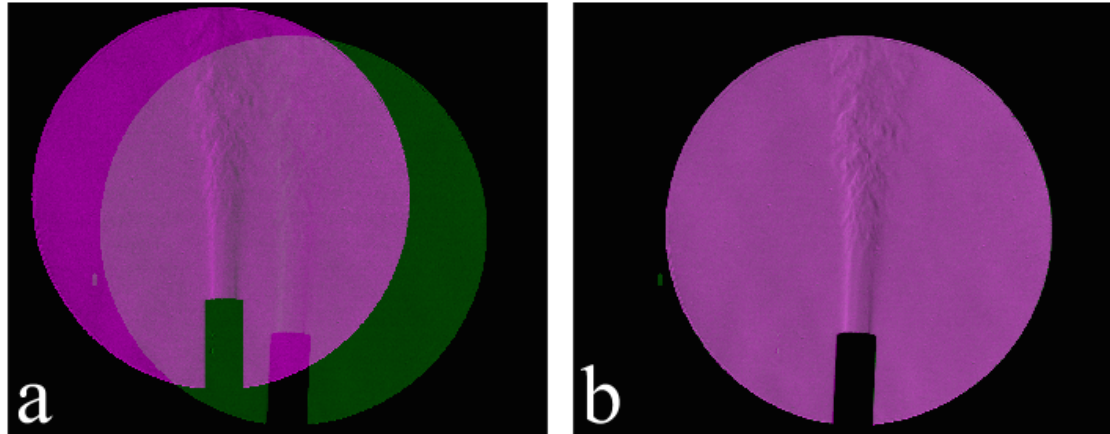


Figure 3.4: Example of schlieren images captured simultaneously with two-camera system: (a) frames overlaid before performing MATLAB image registration, and (b) frames overlaid after performing MATLAB image registration.

After image registration was performed, background subtraction and image length scale calibrations were performed before moving forward to the next steps of data processing.

3.4 Quantitative schlieren methods

Each schlieren image has a visible grayscale gradient captured across the given flow feature in the test section. Each of the intensities within that gradient correlates to an angle of refraction caused by that flow feature. In order to quantitatively evaluate the angle of refraction, a relation between the intensity values throughout the image and the angles of refraction was needed. A calibration process was used where a long focal length, small format plano-convex lens was placed into the test section with the flat side facing the camera [2]. Here, the plano-convex lenses came from CVI Laser Optics. Focal lengths of 5 m and 7.5 m were used. A calibration image of this calibration lens was taken with it in the schlieren test section. The calibration lens refracts light from the edges to the center of the lens. Due to the knife edge at the focal point of the system, a gradient is produced along the lens orthogonal to the position of the knife edge, i.e., a horizontal knife edge produces a vertical gradient, and vice versa. Because the focal length of the calibration lens in the test section was known, a theoretical profile for position within the lens versus refraction angle could be determined

using a variation of the thin lens equation [59]. The thin lens equation for change in refractive angle is given by [1]:

$$\frac{1}{o} + \frac{1}{i} = \frac{1}{f} \quad (3.2)$$

where o is the object distance, i is the image distance, and f is the lens focal length. The thin lens equation details the relationship between where the object to be imaged is located (o) and where the image forms (i). When a light ray is bent by an angle ϵ , it converges onto the image plane with a certain displacement x . From this understanding, the following is derived to calculate the angle of refraction:

$$\tan(\epsilon) = \frac{x}{f} = \frac{(I - I_{\text{avg}}) p}{f} \quad (3.3)$$

$$\epsilon = \tan^{-1} \left(\frac{(I - I_{\text{avg}}) p}{f} \right) \quad (3.4)$$

where I is the light intensity at a given location, I_{avg} is the average background intensity of the given test section, p is the size of each pixel in the image as previously determined through image distance calibrations, and f is the focal length of the calibration lens being used. The value of ϵ is calculated in radians.

The pixel intensity to lens position, R_x , calibration was performed by extracting a line of pixels across the calibration lens perpendicular to the gradient caused by the knife edge cutoff. A linear regression of pixel intensity versus radial position was performed on this line of pixels. Figure 3.5 provides an example of a calibration lens being used to determine a calibration curve relating pixel intensity to radial position. The average background intensity (I_{avg}) was taken as a value of zero refraction ($\epsilon=0$). The location within the lens corresponding to this background intensity (r_{avg}) was then found. Using the location of zero refraction, the lens geometry could be used to determine angles of refraction.

To use this calibration to determine the angle of refraction (ϵ_x) at a given location, the intensity at that location in the image must first be measured. The intensity was then used to determine where on the calibration lens curve that intensity exists, $R_x(I)$. The amount of displacement within the calibration lens (r_x) was then calculated using the location found within the calibration lens (R_x) relative to the location found of zero refraction (r_{avg}).

$$r_x = R_x - r_{\text{avg}} \quad (3.5)$$

$$\epsilon_x = \tan^{-1} \left(\frac{r_x}{f} \right) \quad (3.6)$$

Once the angle of refraction was calculated, it could then be related to an index of refraction (n). Light rays moving through an optically transparent medium of

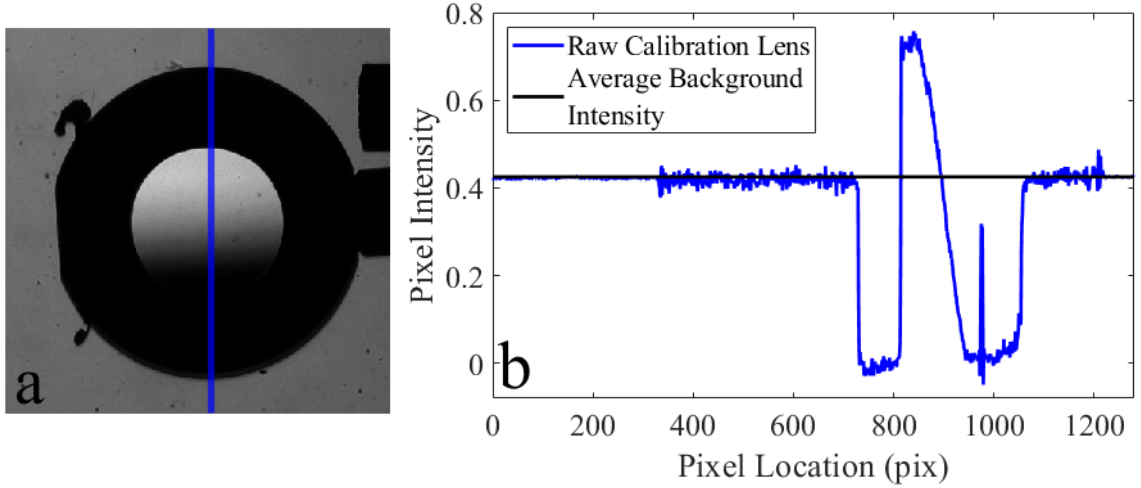


Figure 3.5: (a) Calibration lens in field of view with center column of extracted pixels highlighted. (b) Associated calibration curve for quantitative schlieren measurements.

varying index of refraction are bent based on the spatial refractive index gradients [1]. A light ray traveling in the z -direction (along the path of light through the test section) is refracted through an angle ϵ_x due to the refractive index gradient in the x -direction. This is represented for a two-dimensional schlieren as follows [2]:

$$\epsilon_x = \frac{1}{n} \int \frac{\partial n}{\partial x} dz \approx \frac{Z}{n_\infty} \frac{\partial n}{\partial x} \quad (3.7)$$

assuming $\frac{\partial n}{\partial x}$ is constant over x . From this, the index of refraction, n , can be related to the density of the flow field gas, ρ . This is done through the Gladstone-Dale Law [1]:

$$n = \kappa\rho + 1 \quad (3.8)$$

It should be noted here that the value of the Gladstone-Dale Coefficient, κ , varies for different gases.

3.4.1 Color-filtered schlieren calibration

For the simultaneous color-filtered schlieren setup, similar quantitative schlieren techniques were used with some added steps. For reference, an example of the data collected through this system is provided in Figure 3.6.

While each camera was only allowed to view light emitted from the test section at a single wavelength of interest, the same quantitative schlieren calibration process was still possible. A calibration lens was placed in the test section.

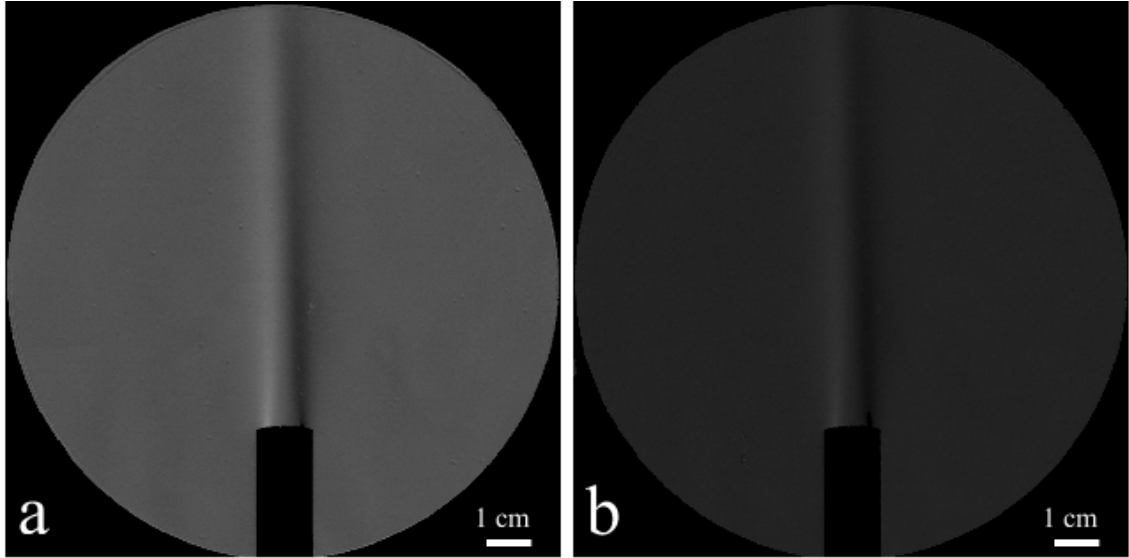


Figure 3.6: Example of the data collected through simultaneous color-filtered schlieren: (a) 530 nm filtered schlieren view, and (b) 650 nm filtered schlieren view.

Calibration images of the lens were taken simultaneously with the two cameras. Because a single knife edge cutoff was used to create a gradient in the calibration lens before the light was divided between the two cameras, the calibration curves produced by the lens in each camera view could be used to calibrate the data for each respective camera. Figures 3.7 and 3.8 depict a single calibration lens as seen by the cameras at 530 nm and 650 nm, respectively, along with their corresponding calibration curves. As seen, the average background intensity was higher at 530 nm than at 650 nm. This was due to the higher overall intensity emitted by the light source at 530 nm than at 650 nm, as seen in the spectral response plot in Figure 2.6. This was taken into account when calibrating the data from each camera. The goal was to maintain an appropriate range of pixel response to capture the highest and lowest possible intensities expected in the measurement region of each image. Therefore, the same exact dynamic range of overall intensities was not required. In this example, a calibration lens with a focal length of 7.5 meters was used. Because these calibration curves were produced using the same methods used for normal schlieren, values such as ϵ , n , and ρ could still be determined from each view of the event.

According to the material dispersion property, refractive index is inversely related to the wavelength of the light [59]. However, in the context of this work where both wavelengths of interest are relatively close together and both within the visible spectrum, this difference is less than 1% for the resulting angles of refraction measured [1, 60]. This was calculated for dry air, for example, using the following equations [60]:

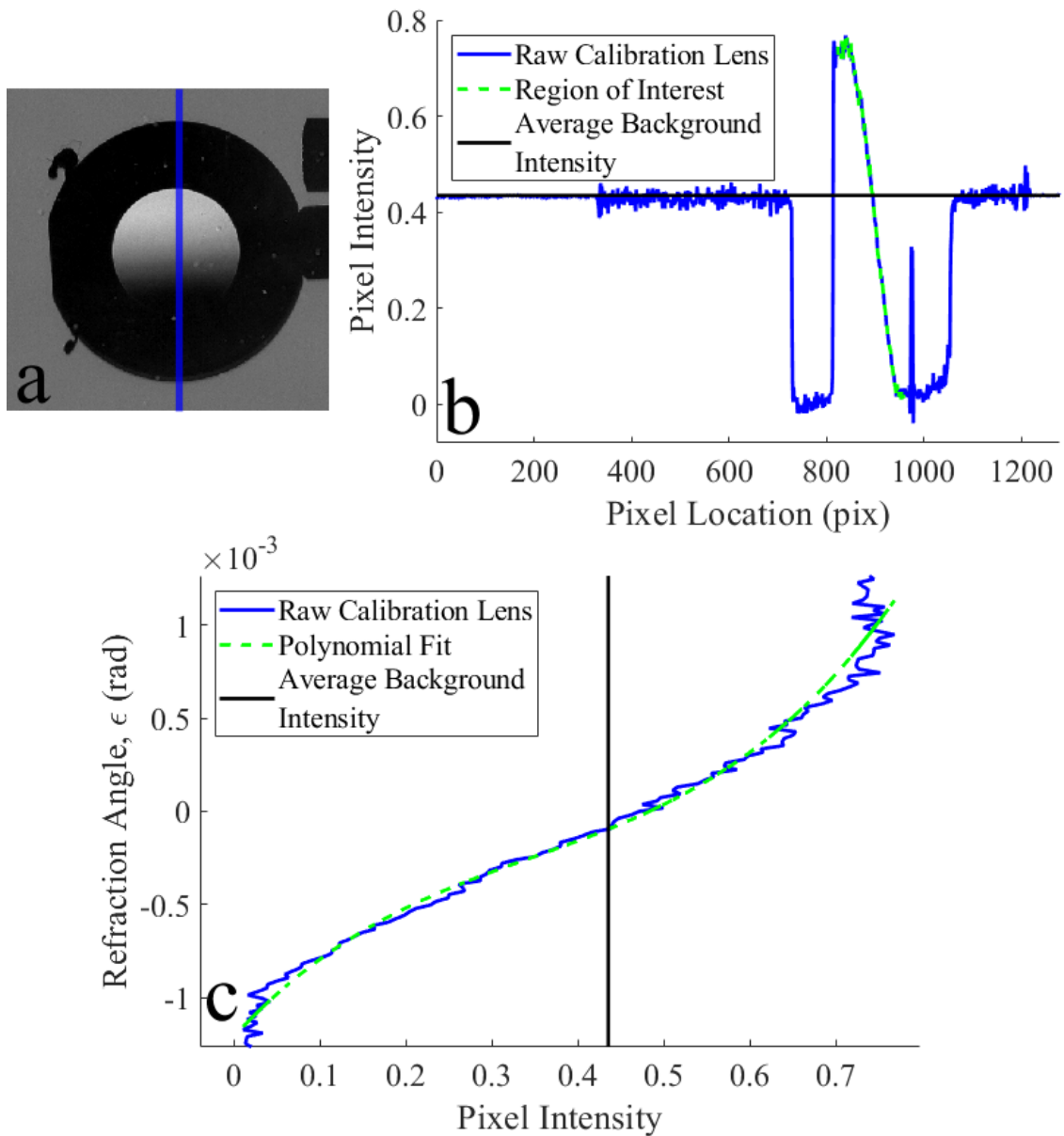


Figure 3.7: 530 nm color-filtered schlieren view of calibration lens for quantitative schlieren measurements: (a) calibration lens image, (b) corresponding pixel versus intensity calibration curve with region of interest outlined in green, and (c) corresponding refraction angle (ϵ) versus intensity with polynomial fit outlined in green.

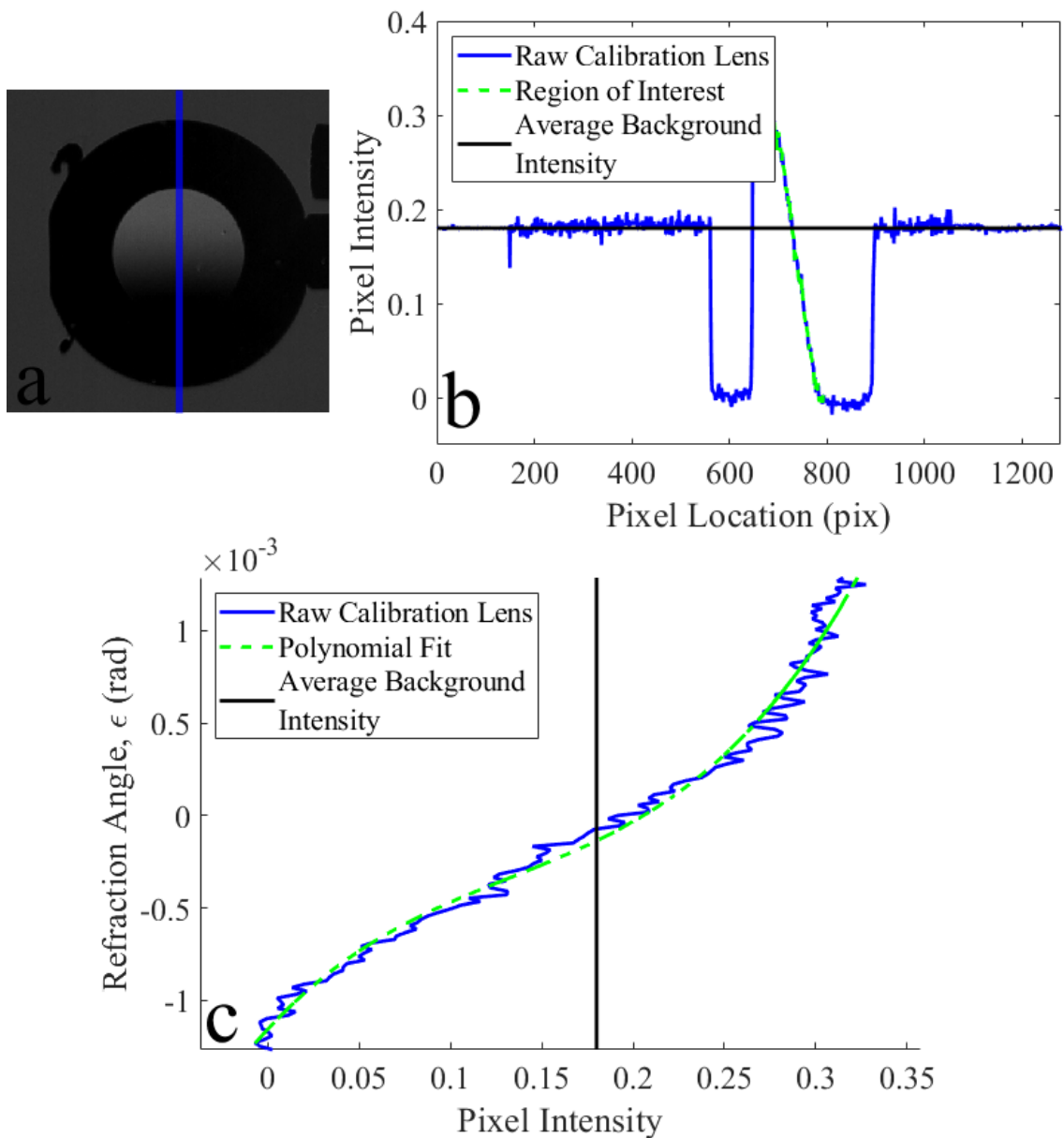


Figure 3.8: 650 nm color-filtered schlieren view of calibration lens for quantitative schlieren measurements: (a) calibration lens image, (b) corresponding pixel versus intensity calibration curve with region of interest outlined in green, and (c) corresponding refraction angle (ϵ) versus intensity with polynomial fit outlined in green.

$$(n_{\text{as}} - 1) \cdot 10^8 = \frac{k_1}{k_0 - s^2} + \frac{k_3}{k_2 - s^2} \quad (3.9)$$

$$(n_{\text{axs}} - 1) = (n_{\text{as}} - 1) \left[1 + 0.534 \times 10^{-6}(x_c - 450) \right] \quad (3.10)$$

$$n_g = n + s \frac{dn}{ds} \quad (3.11)$$

$$(n_{g,\text{axs}} - 1) \cdot 10^8 = \left[\frac{k_1(k_0 + s^2)}{(k_0 - s^2)^2} + \frac{k_3(k_2 + s^2)}{(k_2 - s^2)^2} \right] \left[1 + 0.534 \times 10^{-6}(x_c - 450) \right] \quad (3.12)$$

Here, n_{as} is the phase refractive index of standard dry air, n_{axs} is the corrected phase index for CO₂ concentration x_c (in ppm), n_g is the group refractive index, and s is the wavenumber in units of μm^{-1} where λ is the vacuum wavelength in micrometers. The constants are: $k_0 = 238.0185$, $k_1 = 5792105$, $k_2 = 57.362$, $k_3 = 167917$. These equations apply to standard dry air at 15 °C and 101325 Pa, with a baseline CO₂ content of 450 ppm. For calculations at specific wavelengths (e.g., 530 nm or 650 nm), convert the wavelength to micrometers, compute $s = 1/\lambda$, and substitute into the above equations to evaluate refractive index values.

3.4.2 Abel inversion transform

This method of relating the gradients seen through schlieren imaging to a density field assumes a two-dimensional schliere. However, the flow field of interest consists of a gas plume of non-uniform thickness through which the light must pass. A schematic of this concept is provided in Figure 3.9. As shown, some light rays passing through the gas plume have a shorter distance to travel than others due to the cylindrical nature of the plume. This affects the degree to which the light is bent, but this difference is not directly seen through the schlieren images captured. This is where the Abel process must be used to deconvolute the two-dimensional projection of a three-dimensional flow field. For this application, the two-point Abel method was used.

Traditionally, the Abel inversion transform is performed analytically under the assumption that the data follows a continuous function. However, due to the nature of the experimental setup used, data was instead collected at distinct radial positions (varied at each image pixel). The two-point Abel inversion method described by Tobin and Hargather (2016) and based on the work of Kolhe and Agrawal (2009) provides a discrete approximation of the Abel inversion that is well-suited for experimental datasets [8, 45]. The Abel transformation is performed by solving the following functions [8]:

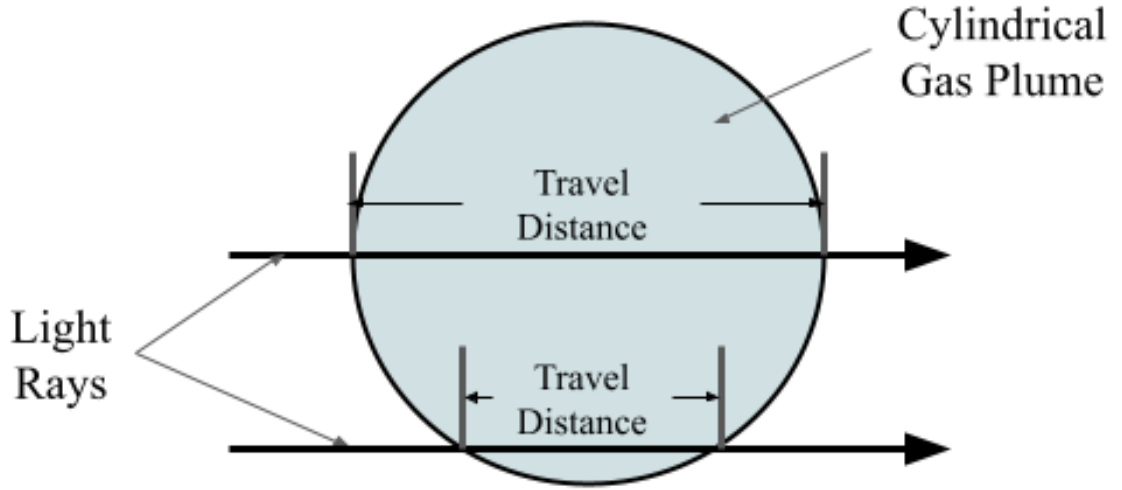


Figure 3.9: Diagram of light path through a circular plume cross-section.

$$\delta(r_i) = \sum_{j=i}^{N+1} D_{i,j} \cdot \epsilon_j \quad (3.13)$$

$$D_{i,j} = \begin{cases} \frac{1}{\pi} (A_{i,j} - A_{i,j-1} - jB_{i,j} + (j-2)B_{i,j-1}), & \text{if } j > i \text{ and } j \neq 2 \\ \frac{1}{\pi} (A_{i,j} - jB_{i,j} - 1), & \text{if } j > i \text{ and } j = 2 \\ \frac{1}{\pi} (A_{i,j} - jB_{i,j}), & \text{if } j = i \text{ and } i \neq 1 \\ 0, & \text{if } j = i = 1 \text{ or } j < i \end{cases} \quad (3.14)$$

$$A_{i,j} = \sqrt{j^2 - (i-1)^2} - \sqrt{(j-1)^2 - (i-1)^2} \quad (3.15)$$

$$B_{i,j} = \ln \left(\frac{j + \sqrt{j^2 - (i-1)^2}}{(j-1) + \sqrt{(j-1)^2 - (i-1)^2}} \right) \quad (3.16)$$

$$\delta(r_i) = \frac{n(r_i)}{n_0} - 1 \quad (3.17)$$

3.5 Imaging spectrometer calibration

The wavelength axis of the images taken through the imaging spectrometer had to be calibrated separately from the spatial axis of the images. This was done using a series of color bandpass filters. The bandpass filters used here were made by ThorLabs and came as part of a kit with ten different bandpass filters (ThorLabs FKB-VIS-10). The bandpass filters were each 25.4 mm in diameter. Each one is manufactured to allow between approximately 25 and 50 percent of the light at that wavelength through to the camera (depending upon the wavelength of interest), blocking out other outside wavelengths. This set was made with a wavelength bandpass of 10 nanometers, meaning the range of light allowed through from the central wavelength of interest was approximately ± 5 nanometers.

Four bandpass filters at 500 nm, 530 nm, 590 nm, and 650 nm were chosen for the calibration of the imaging spectrometer. These were chosen because they were well within the range of light emitted by the SugarCube LED light source and covered the full range of the area of interest. The SugarCube also had a high enough intensity at each of those four wavelengths to still see the light passed through the bandpass filter in the calibration image. If the intensity was too low, the filter would block too much of the light, and the signal-to-noise ratio would be too low to properly calibrate the pixels.

The test section was not large enough to place all four bandpass filters side by side for a calibration with a single image. Therefore, one bandpass filter at a time was placed in front of the entrance slit of the imaging spectrometer to filter the light before entering. This resulted in a thin horizontal strip of light being seen in each calibration image. These strips of light corresponded to the location of each of those wavelengths, respectively. Examples of these calibration images taken are provided in Figure 3.10. These examples were captured with a Nikon D780 DSLR camera to show what the filtered and unfiltered background spectral response looks like in color for easier description and understanding. Again, the rest of the data captured throughout this work was in grayscale.

Since no part of the test setup was moved or altered during this process, it was assumed that the location of each wavelength in each image could be compared to each other in one plot. Figure 3.11 shows an example of how this calibration works. It depicts the original background measured intensity of the SugarCube LED, as well as the intensity of the SugarCube after each bandpass filter has been applied. The peak of each bandpass filter curve was assumed to be the center point location of each individual wavelength. These peaks were used to determine a scale to be applied to each image from the imaging spectrometer to apply a consistent vertical wavelength axis. Because of the sensitivity of the imaging spectrometer and the system as a whole, it was vital that nothing be moved or adjusted from the start of the calibration process to the end of testing.

An important point to note is that the internal grating of the Horiba MicroHR imaging spectrometer can be rotated to change the central wavelength of interest. This is done using the accompanying Horiba software. This was done to ensure as much of the background light intensity was in the camera's view as possible,

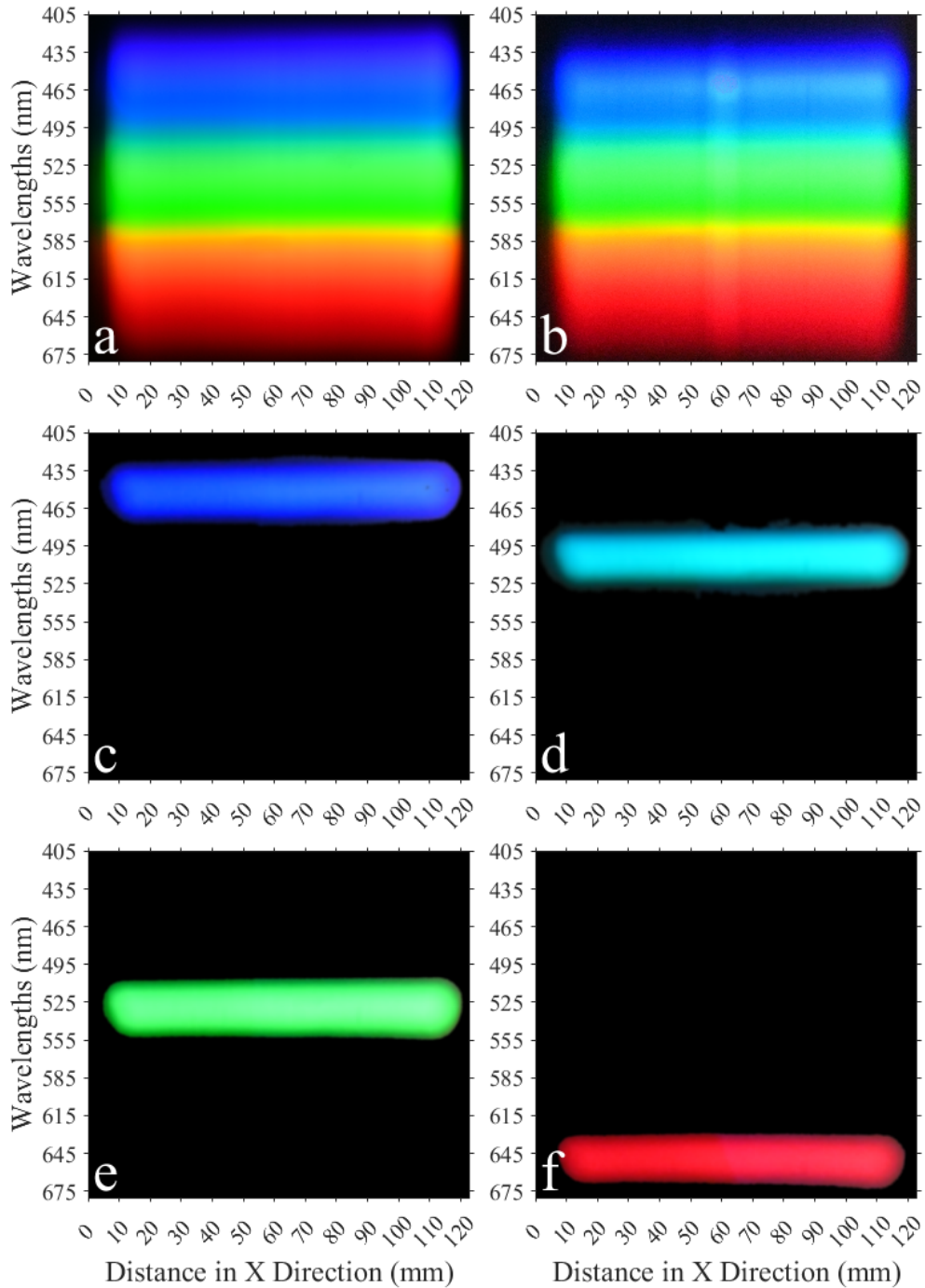


Figure 3.10: Color images of imaging spectrometer data: (a) Background spectral response of SugarCube LED, (b) spectral response with helium plume passing through test section, and bandpass filtered spectrum at (c) 450 nm, (d) 500 nm, (e) 530 nm, and (f) 650 nm.

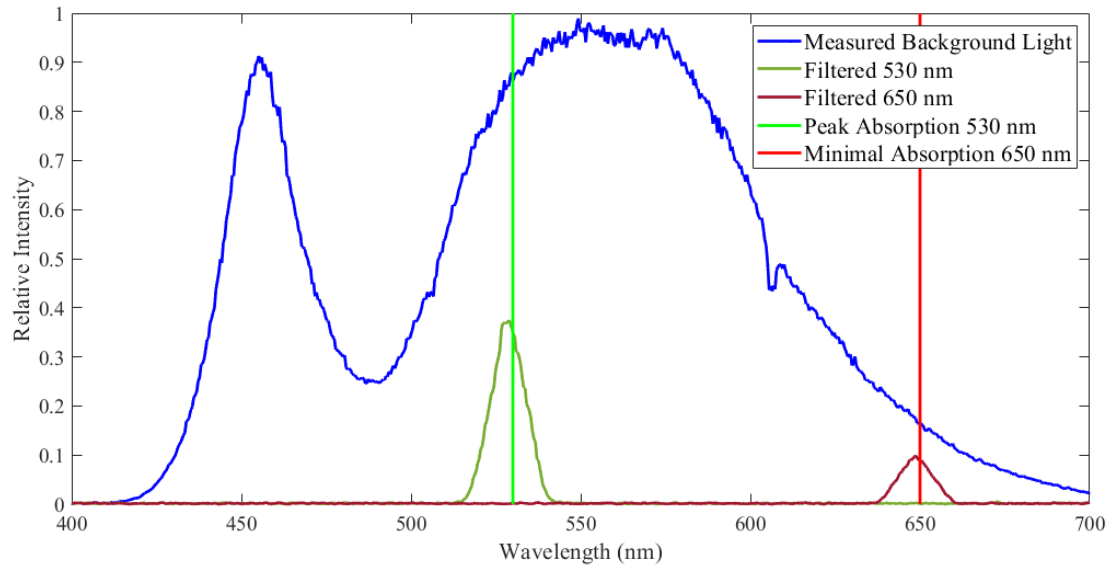


Figure 3.11: Relative light intensities of SugarCube LED before and after color bandpass filters are applied.

with the main focus on the two wavelengths of interest (530 nm and 650 nm). To achieve this, the grating was set to a center point of 650 nm.

3.6 Correlating fields of view between schlieren and imaging spectrometer

While both cameras viewed light from the same test section, there were inherent discrepancies in precisely what they viewed as well as the scaling of each. In order to quantitatively evaluate events and changes visualized during testing, the images from one camera had to be related properly to the images in the other. Described here are the processes by which these relationships were derived.

3.6.1 Aligning center position of both views

One step in the process of correlating positions in one view to the other was to use a calibration object in the test section that both cameras could see. One such example was the same optical post that was used to determine a length scale for the imaging spectrometer data. The length scale in the two views was different as a product of different lens zoom amounts and how light moved through the imaging spectrometer. However, the same calibration object could still be seen in both views. The center line of that object could also be determined in both views, similarly to the process described above for calibrating the imaging spectrometer.

These matching center lines were used as baseline locations. Positions within the field of view could be measured outward from there using the individual length scales determined for each camera's data set. An example of this correlation process with the center lines drawn and position axes determined is provided in Figure 3.12.

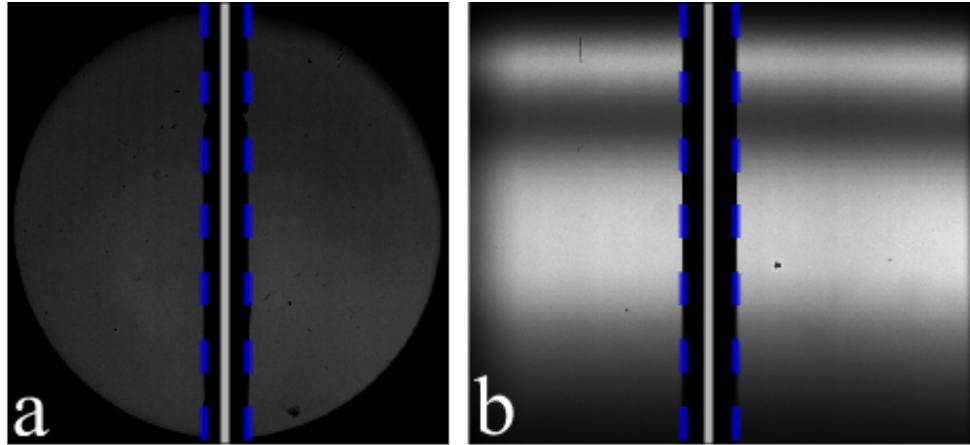


Figure 3.12: Calibration optical post in both schlieren and imaging spectrometer field of view for determining spatial position correlation. Object edges are outlined in blue and their center-lines are drawn in white.

3.6.2 Imaging spectrometer field of view within schlieren images

While the imaging spectrometer records light from the same test section as the schlieren images, the outer boundaries of the field of view seen by each camera are not the same. The imaging spectrometer entrance slit has a set width with an adjustable height that is kept relatively narrow to limit the amount of background light entering the spectrometer. Because of the geometry of the entrance slit, the imaging spectrometer records a narrow rectangular strip of light from the schlieren field of view corresponding to the width and height of the entrance slit. The edges of that slit were found in the schlieren field of view by slowly moving a flat edged reference object into the field of view until a corresponding change was visible through the imaging spectrometer. This was done for all four edges of the rectangle. A small lab jack was positioned on each side of the field of view so that its platform could slowly be raised and lowered into the field of view to find the corresponding edges. An example of this process being performed in the schlieren field of view is provided in Figure 3.13.

The imaging spectrometer field of view is indicated by the light blue rectangle drawn over the schlieren image in Figure 3.14a. As previously mentioned, for these experiments the entrance slit was set to approximately 1 mm in height with

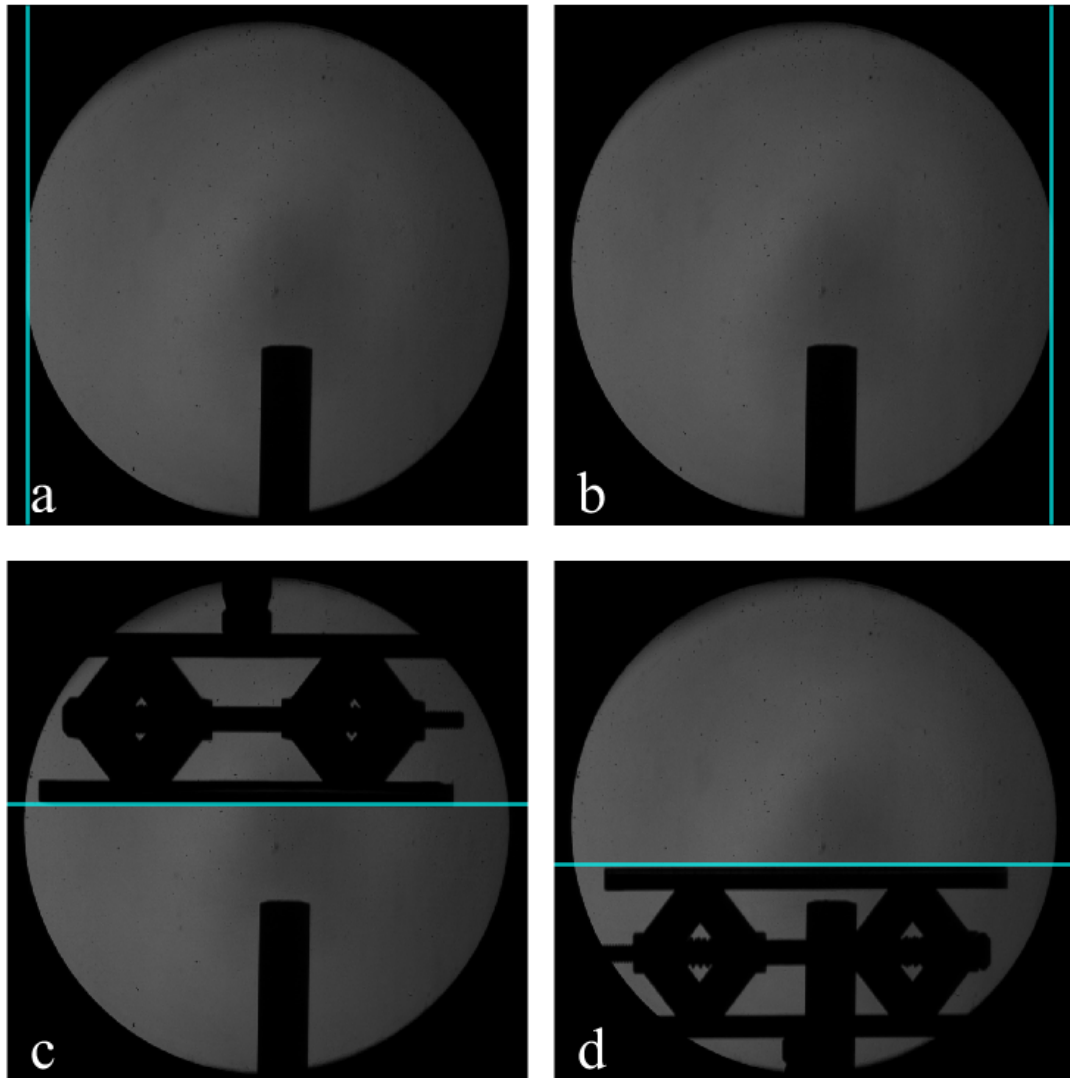


Figure 3.13: A small lab jack was used to find the edges of imaging spectrometer field of view within schlieren images: (a) left edge, (b) right edge, (c) top edge, and (d) bottom edge.

its fixed width of 8 mm. The height of the entrance slit was optimized to maximize the intensity of the spectrum while minimizing the size of the window viewed. The resulting spectrum from the corresponding region of the test section is shown outlined in red in Figure 3.14b. The horizontal axis denotes the spatial aspect of

the spectrum corresponding to the horizontal spatial axis of the schlieren image. The vertical axis of the spectrum image denotes wavelengths of light recorded by the spectrometer, measured in nanometers.

The pipe exit point for the gas plumes can be seen entering the field of view from the bottom of the schlieren image. An example of a gas plume exiting the pipe and flowing through the test section is shown in Figure 3.14c. The plume itself is outlined in green to show its path moving vertically through the test section. As the gas moves through the test section, the spectral response within that region of the test section changes due to the gas's presence and is recorded by the imaging spectrometer. This change is recorded as a darkened vertical strip within the spectrum. This response is also outlined in green as shown in Figure 3.14d. This dark region depicts the differences in light seen through the test section due to the presence of the plume. Similarly to how the position of a calibration object could be correlated to the same position between both fields of view, the position of the gas plume can also be correlated to the same position between both fields of view.

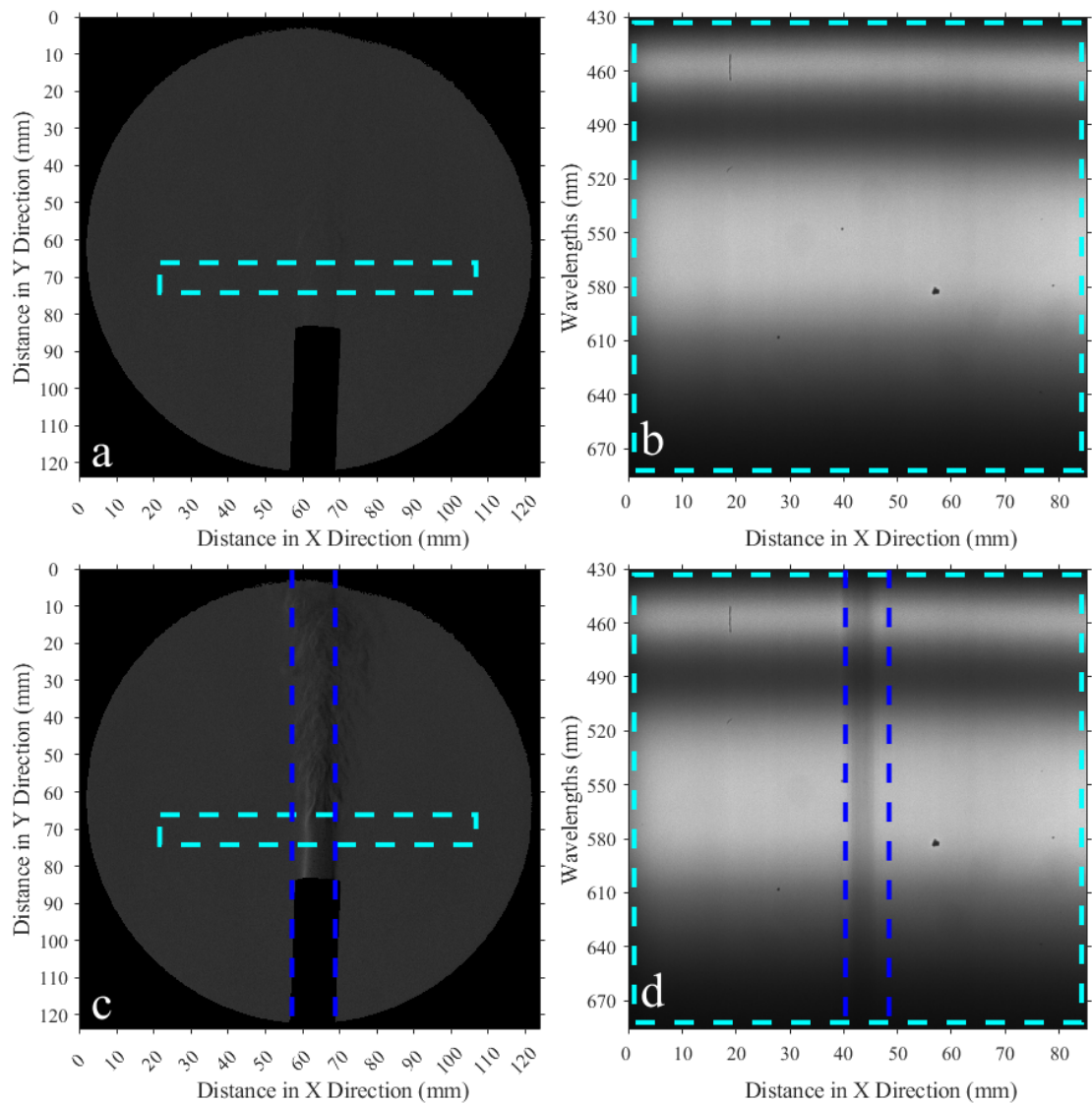


Figure 3.14: (a) Schlieren field of view with spectrometer view outlined in light blue. (b) Spectrometer view of light emitted by test section. (c) Schlieren view of plume moving through test section, with spectrometer view outlined in light blue. (d) Spectrometer view of light emitted by test section with plume region outlined in dark blue.

CHAPTER 4

RESULTS AND DISCUSSION FOR SIMULTANEOUS SCHLIEREN AND IMAGING SPECTROSCOPY

Data was captured using the simultaneous schlieren and imaging spectroscopy setup. After subtracting backgrounds of each image and calibrating both the spectrometer images and the schlieren images using the methods described in Chapter 3, the data was processed. Several tests were run with this setup to extract absorption and concentration measurements. Each test run used between 0.1 g and 1.5 g of solid iodine particles in the iodine heating chamber. The spectrometer data was processed first, and the correlation steps discussed in Chapter 3 were used to relate the changes observed to locations within the schlieren images captured.

4.1 Beer-Lambert Law and data processing

In atomic absorption spectroscopy, the Bouguer-Beer-Lambert Law (most often referred to as the Beer-Lambert or Lambert-Beer Law) is a fundamental principle used widely for processing spectroscopic data [11, 24, 61]. It is used to relate measured light intensities to overall absorbance, as the amount of light absorbed by a sample containing the absorbing substance is directly proportional to the substance concentration and path length of the light through the sample. This establishes a linear relationship between absorbance and concentration [11, 22, 24]. There are some known deviations from the linearity of the Beer-Lambert Law when considering high concentrations and high scattering within the absorbing material, however, the Beer-Lambert Law is overall considered an effective and practical approximation for calculations based on absorption of light [23, 24].

The intensity of the incident light emitted from the light source is I_0 . When passed through a medium (whether that be air, helium, etc.), with optical path length b (cm), the intensity of I_0 will decrease to the value I . This reduction in light intensity per differential length db is $-dI$. This value is directly proportional to the intensity value I , the length db , and the number of light-absorbing atoms present along db . The number of atoms is then directly proportional to the concentration of the absorbing species of interest in the test section, c (mol/cm³). This relationship is depicted in Figure 4.1 and mathematically described by:

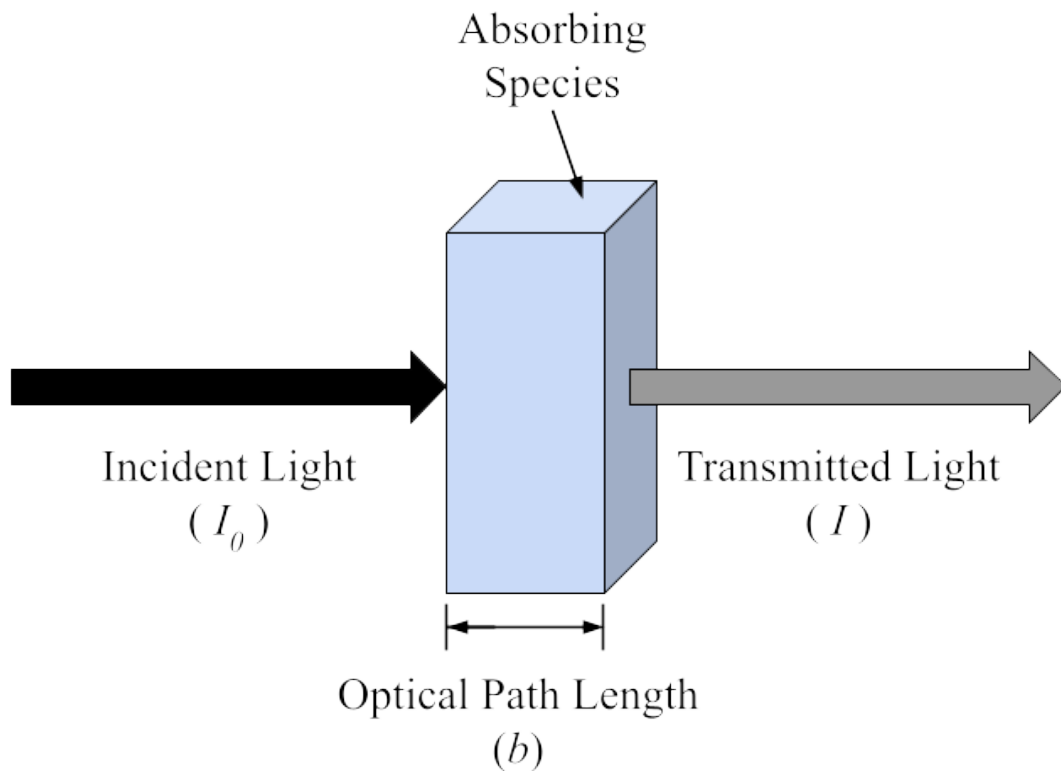


Figure 4.1: Visual depiction of the relationship between incident and transmitted light passing through an absorbing species of an optical path length, b .

$$-dI = k I c db \quad (4.1)$$

where k is the relative coefficient. The formal equation of the Beer-Lambert Law is further derived by integrating Equation 4.1 as:

$$-\int_{I_0}^I \frac{dI}{I} = \int_0^b k c db \quad (4.2)$$

which, assuming a uniform concentration profile and linear relation between concentration and absorption, further simplifies to:

$$\log \left(\frac{I_0}{I} \right) = k' c b \quad (4.3)$$

Breaking that down further, the typical appearance of the Beer-Lambert Law is:

$$A = a b c \quad (4.4)$$

where A is the unitless absorbance $[\log\left(\frac{I_0}{I}\right)]$ and a is the absorption coefficient, also referred to as the molar extinction coefficient. It should be noted that in the literature, the variable a is often replaced with ϵ . However, to avoid confusion here with the ϵ variable associated with the angle of refraction, a will be used to represent the absorption coefficient. For a series of measurements, a and b together determine the slope of the calibration graph [11]. The relationship between absorbance, A , and transmittance, T , is represented by Equation 4.5:

$$A = \log\left(\frac{I_0}{I}\right) = \log\left(\frac{1}{T}\right) \quad (4.5)$$

The light intensity measured by the detector, in this case the high-speed camera, at the exit of the spectrometer is directly proportional to the transmittance. The intensities of the images taken through the spectrometer during data collection were therefore related directly to transmittance and used to calculate absorbance using a modified version of Equation 4.5:

$$A = \log\left(\frac{\text{Background Image Intensity, Pixel } (i, j)}{\text{Test Image Intensity, Pixel } (i, j)}\right) \quad (4.6)$$

Figure 4.2 depicts what the spectrometer data set looks like after applying the Beer-Lambert Law in the form of Equation 4.6 to each pixel. A background spectrum image was taken before any testing was conducted to be used for the I_0 values at each location and wavelength.

Moving forward, several other variables were needed to calculate the concentration of iodine gas within the field of view. The value of the absorption coefficient, a , was needed. To find this, a relationship between the absorption coefficient and the absorption cross-section of iodine gas (σ) was used [62]:

$$\sigma = \frac{2303A}{c \cdot N_A \cdot b} \quad (4.7)$$

where N_A is Avogadro's number (approximately 6.023×10^{23} molecules/mol). The value of 2303 comes from the original form of the equation multiplying absorbance by $\ln(10)$, which equals 2.303. Here, 2303 is used to account for the conversion factor from L to cm^3 . The value of σ as determined by Saiz-Lopez et al. (2004) was $(4.24 \pm 0.50) \times 10^{-18} \text{ cm}^2 \text{ molecule}^{-1}$ at the absorption wavelength 533.0 nm [54]. Equation 4.7 was combined with Equation 4.4 and rearranged to calculate the absorption coefficient a :

$$\sigma = \frac{2303 a b c}{c \cdot N_A \cdot b} = \frac{2303 a}{N_A} \quad (4.8)$$

$$a = \frac{\sigma N_A}{2303} = 1109.08 \text{ L mol}^{-1} \text{ cm}^{-1} \quad (4.9)$$

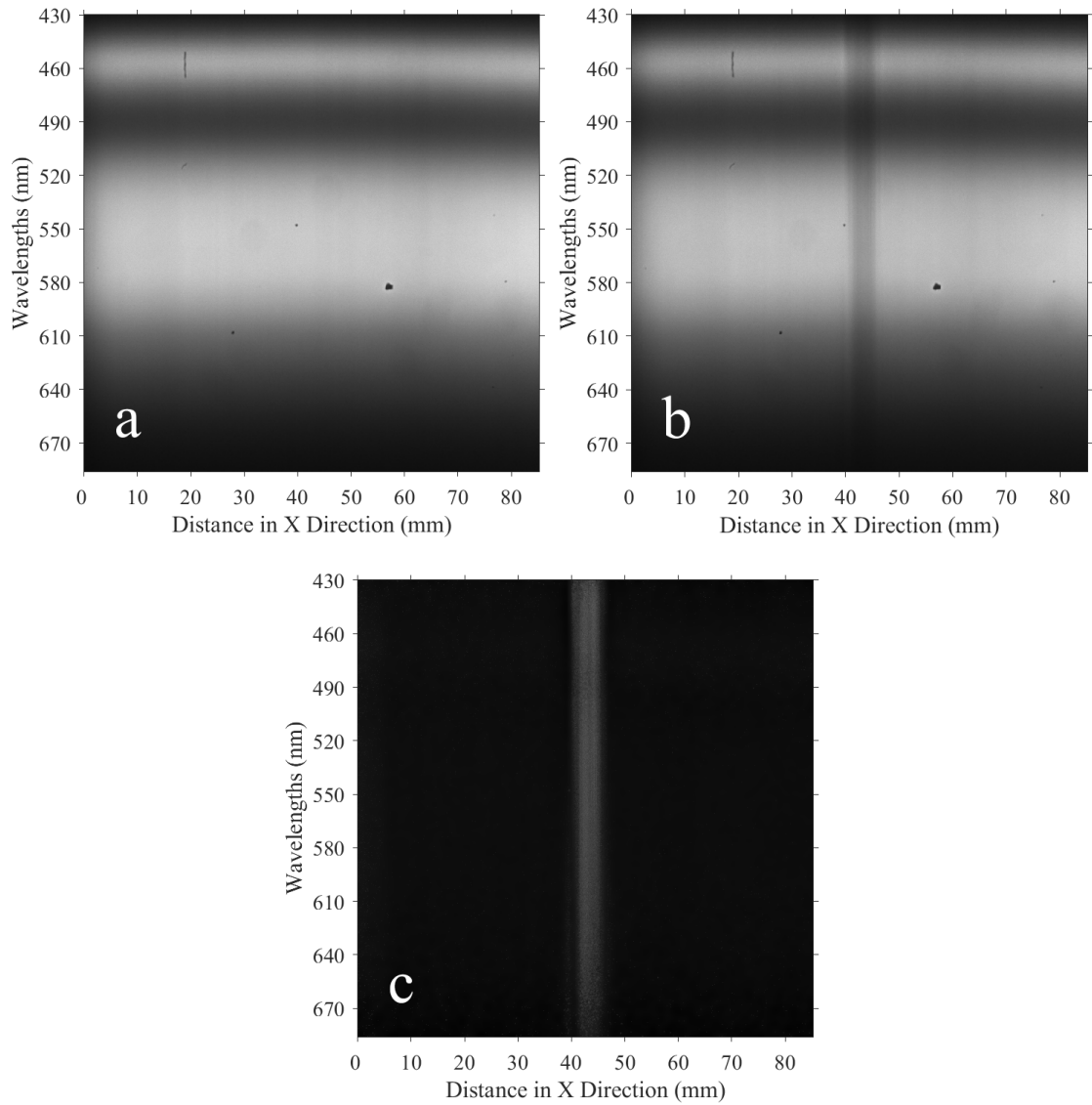


Figure 4.2: Examples of test images captured through imaging spectrometer of the iodine plume: (a) background image of spectral response of SugarCube LED, (b) spectral response resulting from presence of gas plume moving through test section, seen as a darkened vertical stripe across the spectrum, and (c) resulting absorbance map after applying Equation 4.6 to images (a) and (b).

After finding a , the next step in theory would be to rearrange Equation 4.4 to solve for concentration, c , as follows:

$$c = \frac{A}{ab} \quad (4.10)$$

However, here a problem arises. The optical path length, b , is variable when measuring at various points across the plume due to its cylindrical three-dimensional nature. This is where the inverse Radon transform is applied [63, 64].

The observed absorbance values at each pixel represent a line-of-sight (LOS) integrated measurement rather than the true local value at each point within the plume. This is due to the varied optical depth in the three-dimensional space of the plume being measured in a two-dimensional manner. In order to extract the true profile of these measurements at various locations within the plume, the data must be corrected for the plume's three-dimensionality. The plumes used were laminar and therefore assumed to be cylindrical and symmetric radially around the central axis. A modified inverse Radon transform can therefore be used to reconstruct the local absorption at each radial position by inverting the LOS integrated absorbance data. For this application, the following form of the Radon transform is used:

$$A(x) = \int \alpha(x, y) db \quad (4.11)$$

where the measured quantity $A(x)$ is the unitless LOS integrated absorbance $[\log \left(\frac{I_0(x)}{I(x)} \right)]$ taken from each test image and the scalar field of interest $\alpha(x, y)$ is the local absorption coefficient. $A(x)$ is equivalent to the Radon transform of $\alpha(x, y)$ evaluated at $\theta = 0$. Typically, a Radon transform is performed after capturing measurements at multiple angles, or views around the object of interest. However, under the assumption of axisymmetry and uniformity along the optical axis, projections at multiple angles are not physically required. They are mathematically equivalent due to symmetry. Therefore, a synthetic sinogram can be constructed by replicating the single absorption profile across a range of angles (e.g., 0° to 179°), enabling a full two-dimensional reconstruction using the inverse Radon transform.

Because the inverse Radon transform produces values in units of "absorption per pixel", the result must be scaled to physical units. If the pixel size is Δx cm, the reconstructed absorption field has units of cm^{-1} . Once the local absorption coefficient values are determined, they can be returned to the Beer-Lambert Law (Equation 4.4) to determine the local iodine concentrations. This was done by rearranging Equation 4.4 and including the new depth-corrected absorbance values:

$$c(x) = \frac{A}{ab} = \frac{\alpha(x, y)}{a} \quad (4.12)$$

4.1.1 Calculating maximum theoretical concentration

One step performed in order to qualify the calculated concentration values was to determine the theoretical maximum concentration of iodine gas for a given plume. It was assumed that the iodine was thoroughly and evenly mixed within the helium plume. This theoretical maximum iodine concentration was calculated using the amount of solid iodine heated inside the iodine heating chamber for a given test series in combination with known properties of the helium plume carrying the iodine gas into the test section. The first step was to calculate the approximate expected amount of iodine gas, measured in moles, produced by heating the iodine chamber during a given test using Equation 4.13:

$$n_{I_2} = \frac{\text{mass } I_2 \text{ particles}}{\text{molar mass } I_2} \quad (4.13)$$

where the molar mass of iodine is approximately 253.8 g/mol. The total mass of solid iodine particles used varied throughout each test series and was recalculated for each data set analyzed. The volume of the plume viewed within the test section was also approximated in cm^3 :

$$V_{\text{plume}} = \pi \left(\frac{d}{2} \right)^2 L \quad (4.14)$$

where d represents the approximate plume diameter (cm) at the region of interest and L represents the overall length of the plume visible within the field of view (cm). Combining Equations 4.13 and 4.14 allows for the maximum expected concentration of iodine within the test section to be calculated:

$$c_{\text{max}} = \frac{n_{I_2}}{V_{\text{plume}}} \quad (4.15)$$

where c_{max} is measured in mol/L. This maximum concentration value provided a reference for the scale of the cumulative concentration values expected over time after calculating the iodine concentration from each absorbance data set.

4.2 Helium-only plumes

The preliminary gas plume tests were performed with pure helium-only plumes entering the test section. This was done to develop the baseline absorbance expected at the two wavelengths of interest, 530 nm and 650 nm. Helium was expected to have negligible absorbance at both wavelengths. This was especially true in comparison to the absorbance predicted with the presence of iodine gas in later testing. The baseline values gathered for these helium-only plumes were also used to predict the effects of the plume geometry on the light absorbance. The behavior, precise location, and properties of the plumes, such as temperature

and velocity, differed enough with each test that a single baseline could not be universally subtracted from the data. The findings here were used to determine what steps should be taken for processing mixed helium-iodine plume data sets.

The first step in determining absorbance through the helium-only plume was to determine a frame of reference for the location of the plume between data sets. Since the imaging spectrometer does not view the same size field of view as the schlieren images, the center line correlation determined previously as shown in Figure 3.12 was used. This provided a quantified offset between the same region within the schlieren versus the spectrometer view. Then, the center line of the physical plume was determined from the schlieren images captured. The spatial offset determined in Figure 3.12 was then used to predict the center line of the same plume when seen through the imaging spectrometer. An example of the results of that correlation is shown in Figure 4.3.

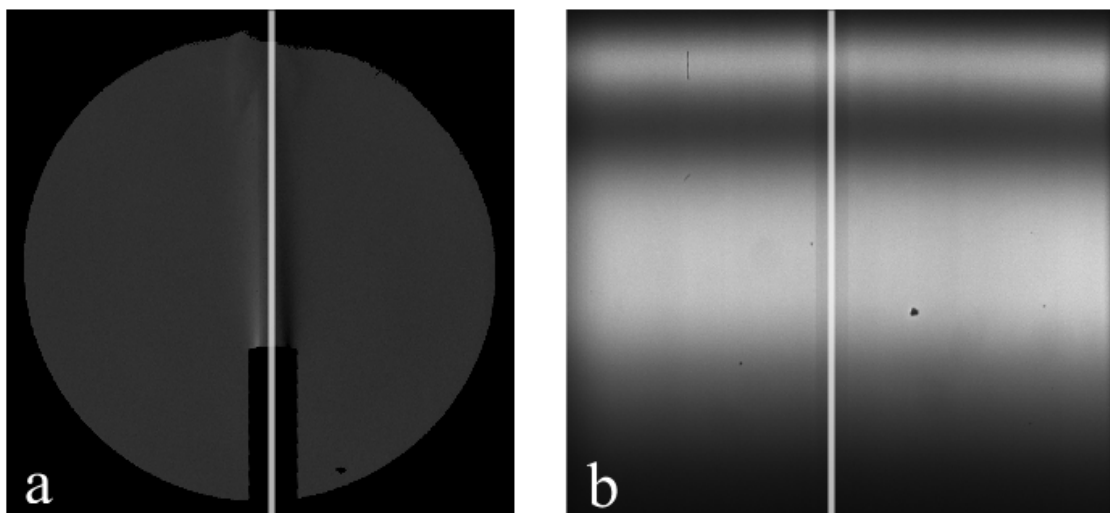


Figure 4.3: The center line of the plume traveling through the test section was correlated and aligned between the two data sets: (a) schlieren image with plume center line drawn in white, and (b) spectrometer image with corresponding plume center line drawn in white.

Next, the Beer-Lambert Law was applied to the imaging spectrometer data as described in Figure 4.2 using Equation 4.6. This resulted in a map of overall LOS integrated absorbance (A) across the entire spectrum image. The map of absorbance was evaluated at the two wavelengths of interest, 530 nm and 650 nm. The intensities represented at each pixel in the Beer-Lambert processed image are directly proportional to the transmittance of light in that region, and therefore were related to absorbance as previously described. The intensities were measured specifically within the pixel rows of the image that were previously calibrated and determined to be at 530 nm and 650 nm using color bandpass filters. Figures 4.4

and 4.5 detail the results of this data processing method at different points in time during the evolution of a helium plume moving through the test section.

As seen in these figures, the absorbance measured as a result of the presence of the pure helium plume was near zero. The raw values taken directly from the image in part b of the figures did show slight variation in the center region where the plume was present. The variations are explained by the inherent shadowgraph effect overlaid on the image as a result of the nature of the optical setup. The distortions caused by the shadowgraph effect were reduced by determining the average intensity change caused by this effect seen across all frames and then subtracting that intensity change from each individual frame. This removed large changes caused by the shadowgraph effect and left behind changes due to absorption. This was deemed appropriate because the absorbance of the pure helium plume was intended to be used as a baseline of zero absorbance at the two wavelengths of interest. The effects in the plot due to the setup rather than the absorbing species were thus resolved.

4.3 Mixed helium-iodine plumes

With the baseline of zero absorption in the helium plume verified, iodine gas was then introduced into the plumes. LOS integrated absorbance was measured through the mixed helium-iodine gas plumes using the same process as for the pure helium plumes. The center line of the plume moving through the test section was correlated between the schlieren and imaging spectrometer data sets. The Beer-Lambert Law was then applied to the spectrometer images to determine a map of LOS integrated absorbance. The resulting LOS integrated absorbance plots at both wavelengths of interest are detailed in Figures 4.6, 4.7, and 4.8. Each of these figures provides a look into the LOS integrated absorbance of the mixed helium-iodine plume at a different point in time as the plume entered the test section. An important assumption was that the iodine gas was fully mixed with the helium gas by the time it entered the test section due to the amount of time and distance traveled between the iodine heating chamber and the pipe exit within the test section. As observed in the images, however, the amount of iodine clearly varies with time, and the plume is not fully mixed.

Each LOS integrated absorption plot was normalized by the values measured at 650 nm. This was done by averaging the absorption measured across the 640-660 nm region of each spectrum image in the data set. This average baseline absorption was then subtracted from both the 650 nm and the 530 nm absorbance taken from each spectrum image. After normalizing the plot to the baseline of zero absorption, some of the shadowgraph effects of the plume were still visible. This effect can be seen as small dips at the outer edges of the plume region. Moving outward from the plume centerline, the absorbance dropped below the line of no absorbance and then stabilized back up to approximately zero in the background region. This plot shape mimics what would be seen in a shadowgraph image of the plume, where the edges of the plume would brighten before stabilizing back

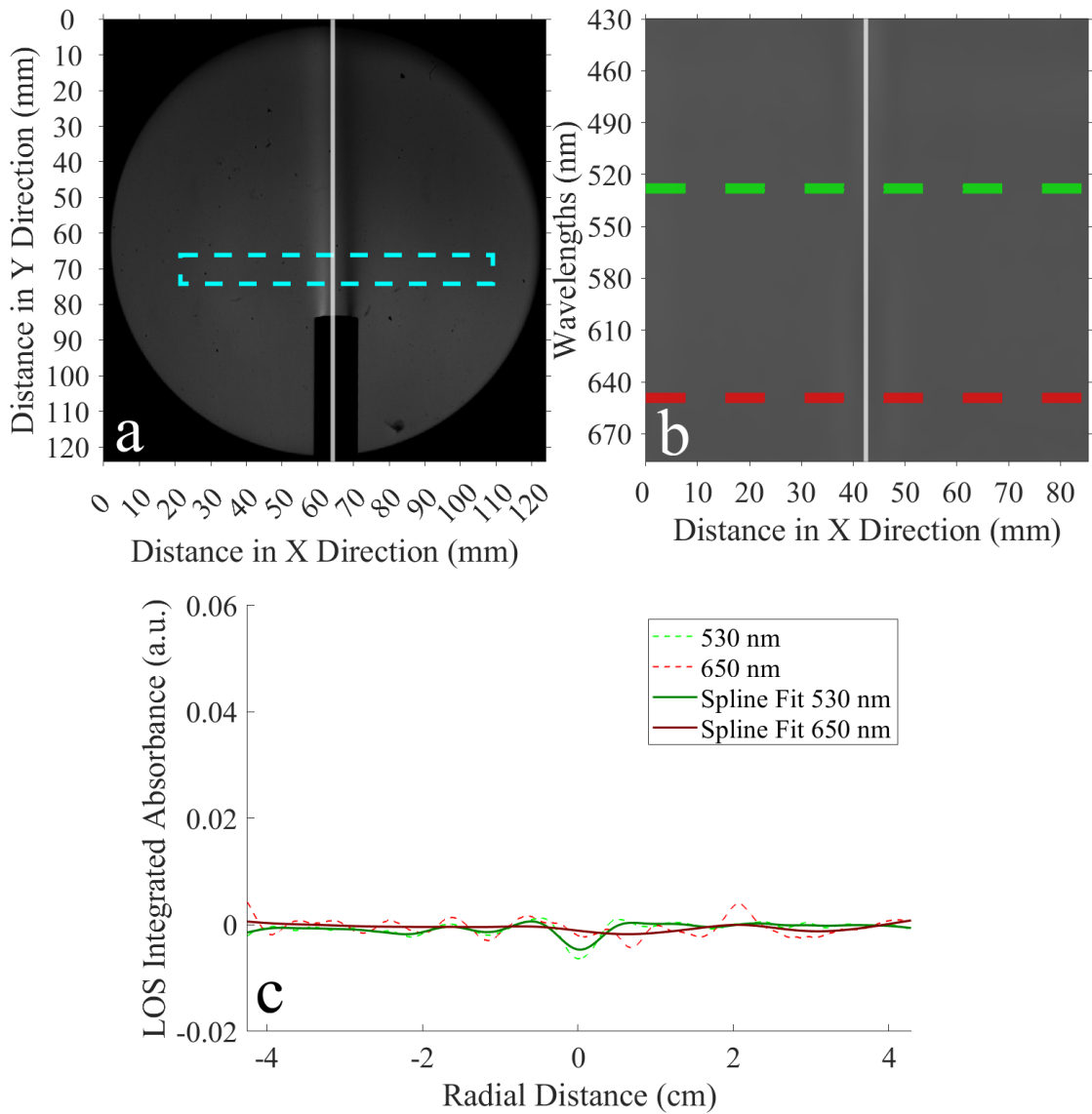


Figure 4.4: Processed data for a pure helium plume at $t = 0$ ms as the plume first enters the spectrometer field of view: (a) schlieren view with plume center line marked in white, (b) Beer-Lambert Law processed spectrometer view representing absorption with center line marked in white and regions of interest at 530 nm and 650 nm outlined in green and red, respectively, and (c) line plot of measured absorbance at both wavelengths of interest. It should be noted that the image in (b) has been brightened by a value of 0.3 for easier visualization.

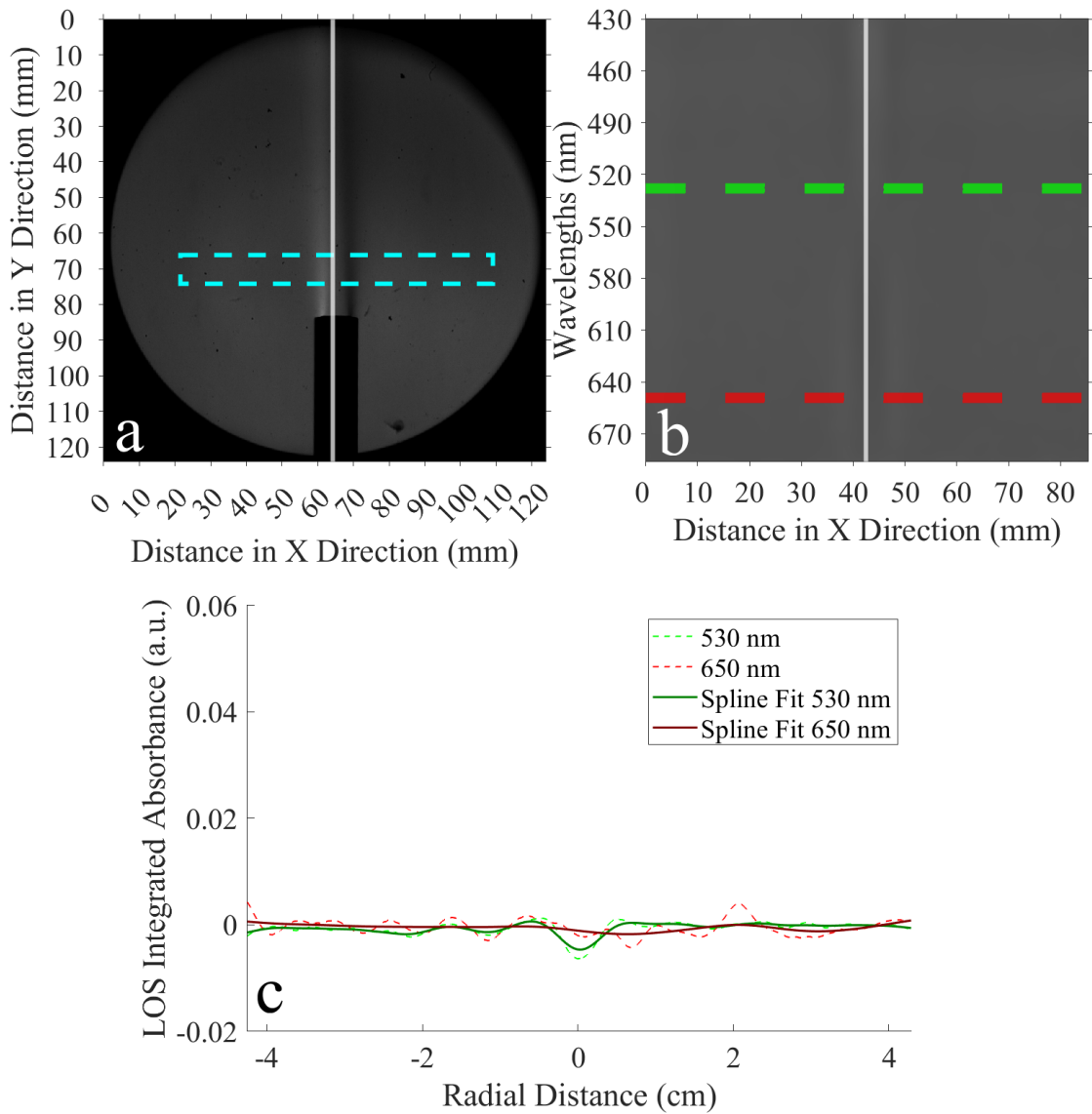


Figure 4.5: Processed data for a pure helium plume at $t = 30$ ms: (a) schlieren view with plume center line marked in white, (b) Beer-Lambert Law processed spectrometer view representing absorption with center line marked in white and regions of interest at 530 nm and 650 nm outlined in green and red, respectively, and (c) line plot of measured absorbance at both wavelengths of interest. It should be noted that the image in (b) has been brightened by a value of 0.3 for easier visualization.

to the background intensity outside of the plume. The light moving through the plume is affected by the non-uniform depth of the plume due to its cylindrical nature. This is where the inverse Radon transform is applied.

4.3.1 Local absorption coefficient and concentration calculation

To deconvolve the LOS integrated absorbance measurements across the plume, the inverse Radon transform equations were applied. Data from the plume in Figure 4.8 was used here to show the comparison of before versus after applying the inverse Radon transform. Data from this plume was chosen over the others shown because it represents the highest and most clearly visualized LOS integrated absorbance measurements during this testing.

As can be seen in Figures 4.6, 4.7, and 4.8, a lot of noise was present in the LOS integrated absorbance measurements. A spline function was applied to smooth each measurement. The spline function in MATLAB returns a vector of values using a cubic spline interpolation as a piecewise polynomial structure. This creates a continuous line through the relative center of each section of data. The spline fits are plotted as a single darker line overlaid over the original absorbance values in part c of each figure. The spline function was only applied to the regions outside the plume boundaries. This was done to smooth values in the ambient region around the plume while maintaining the shape and peak values of the raw absorption data measured through the spectrometer.

While the physical plume was assumed to be axisymmetric, the raw data was not entirely so. In order to produce an axisymmetric form of the data for use in the inverse Radon transform, the spline fit was taken from the right-hand side of the centerline and copied over to the left-hand side. This was done so that the full row of absorbance values could be replicated into a sinogram representing all 180 angles to mimic projections of the axisymmetric plume. Once this was done, the new axisymmetric spline plots, centered around the plume center ($r = 0$), were fed into the inverse Radon transform (Equation 4.11). Figure 4.9 a shows the spline fits for the LOS integrated absorbance measured at 530 nm and 650 nm. It also shows the local absorption coefficient resulting from applying the inverse Radon transform to the 530 nm spline. Figure 4.9 b shows the corresponding iodine concentration values measured across the plume after applying Equation 4.12 to the local absorption coefficient measurements.

The test series used to create the plots shown as examples of absorbance and concentration here used 1.5 grams of iodine in the heating chamber. Using the equations previously described, the maximum estimated concentration value of the plume in the test section was 0.87 mol/L. The concentration values calculated here are significantly lower than that. This was due to a range of circumstances. As the iodine gas traveled through the pipe system, small amounts of it could have cooled enough to stick to the walls of the pipe rather than traveling all the way to the test section. The travel distance from the chamber to the test section was

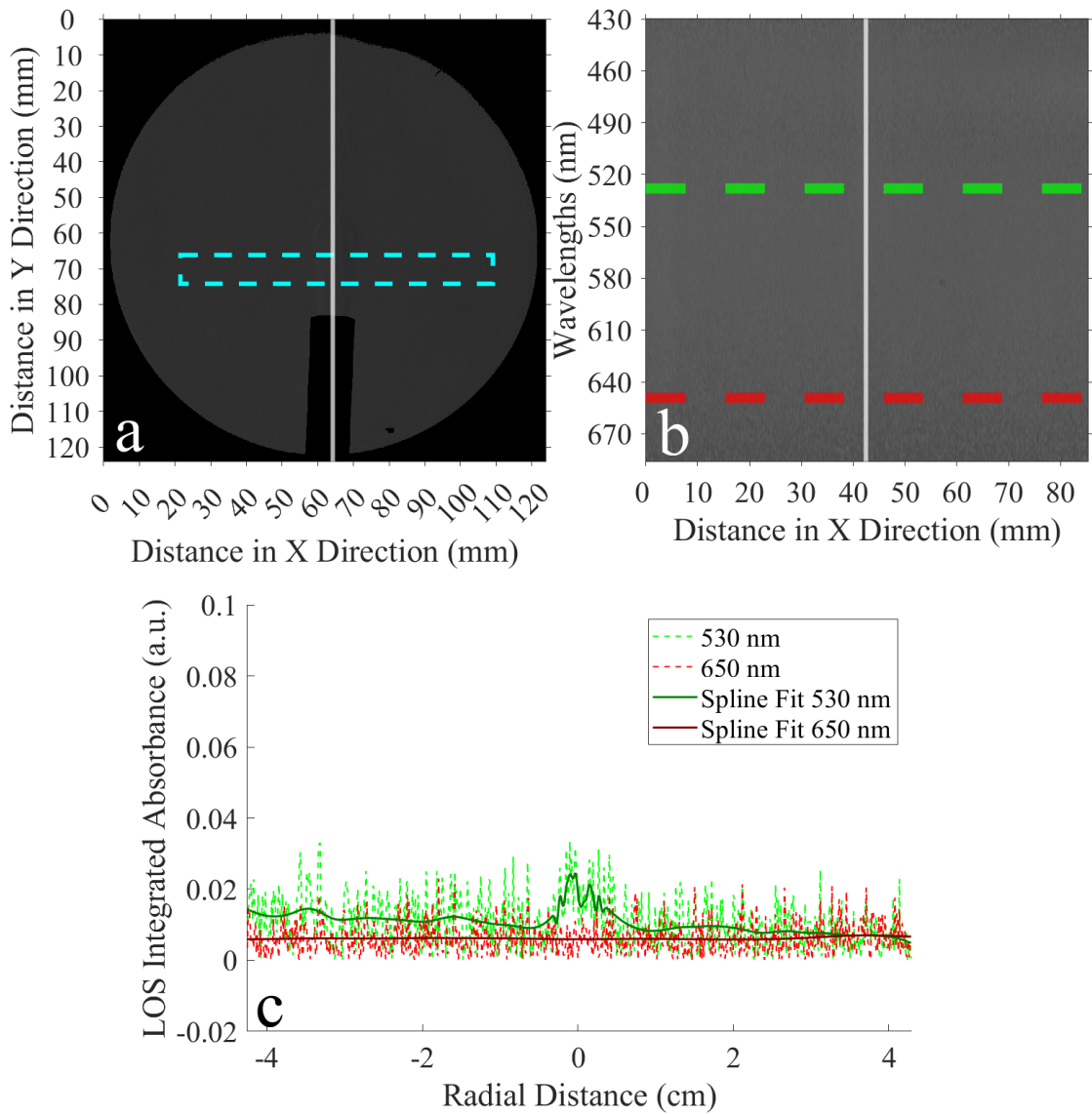


Figure 4.6: Processed data for a mixed helium-iodine plume at $t = 0$ ms as the plume first enters the spectrometer field of view: (a) schlieren view with plume center line marked in white, (b) Beer-Lambert Law processed spectrometer view representing absorption with center line marked in white and regions of interest at 530 nm and 650 nm outlined in green and red, respectively, and (c) LOS integrated absorbance at both wavelengths of interest. It should be noted that the image in (b) has been brightened by a value of 0.3 for easier visualization.

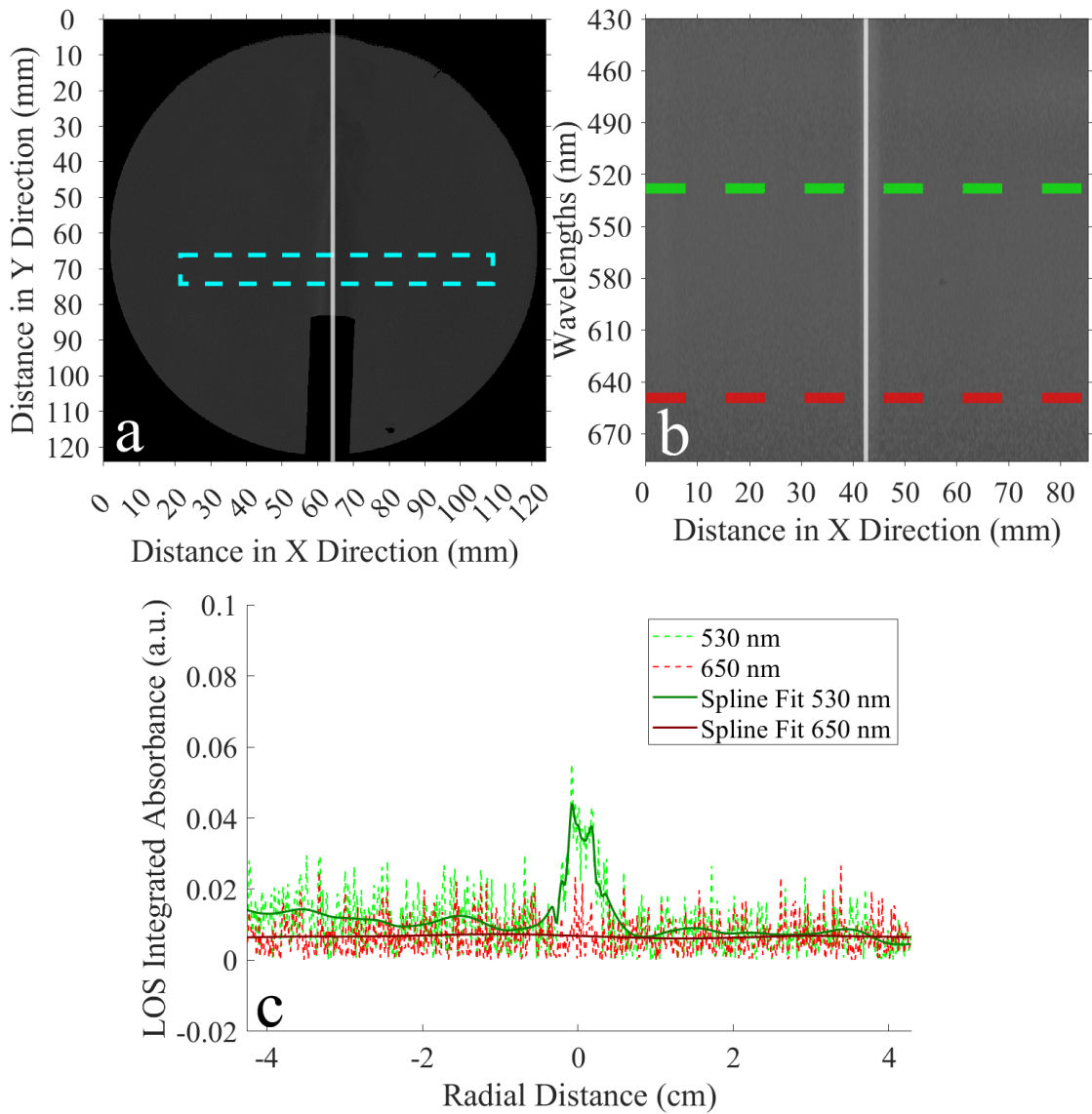


Figure 4.7: Processed data for a mixed helium-iodine plume at $t = 8$ ms: (a) schlieren view with plume center line marked in white, (b) Beer-Lambert Law processed spectrometer view representing absorption with center line marked in white and regions of interest at 530 nm and 650 nm outlined in green and red, respectively, and (c) LOS integrated absorbance at both wavelengths of interest. It should be noted that the image in (b) has been brightened by a value of 0.3 for easier visualization.

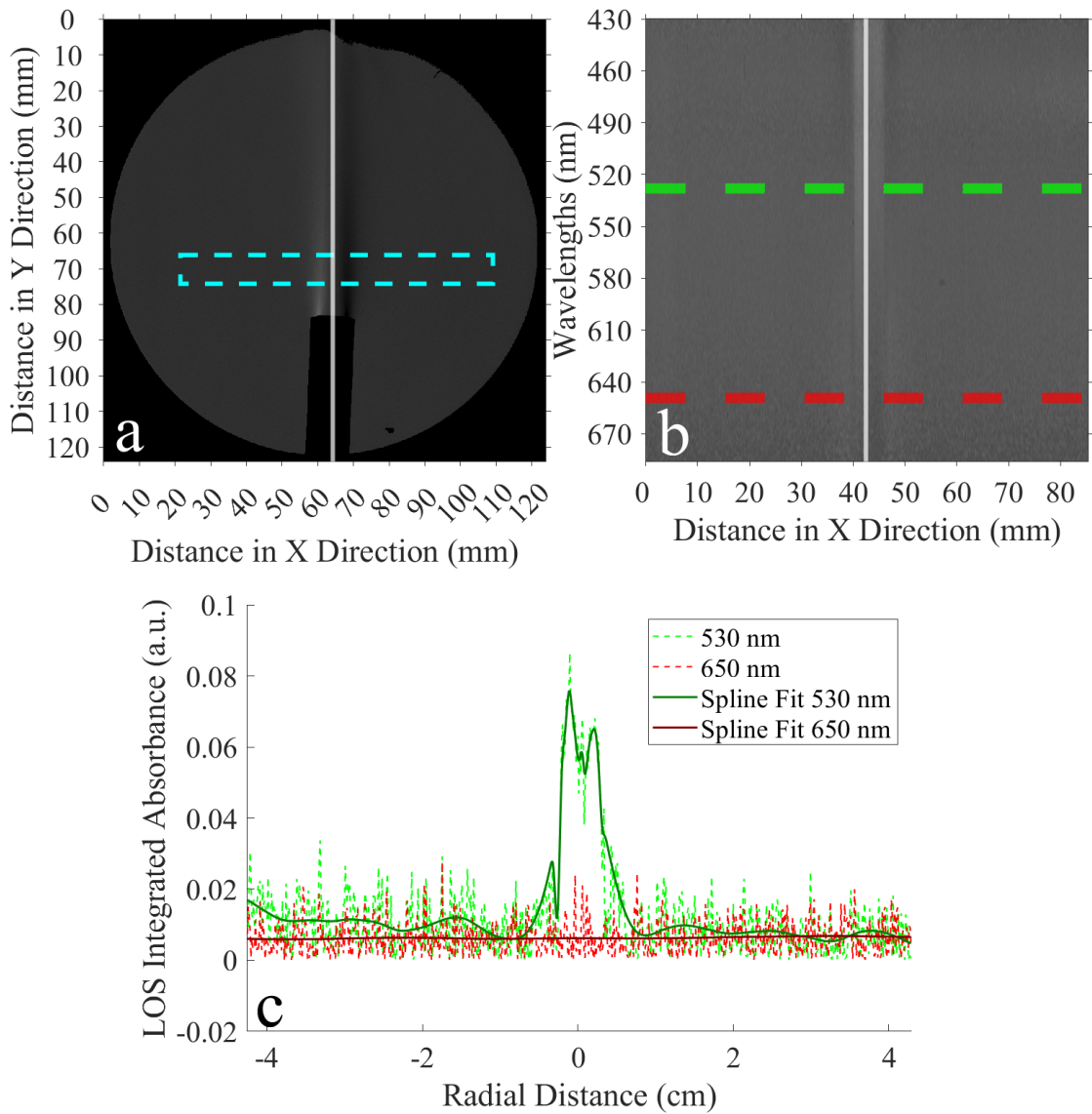


Figure 4.8: Processed data for a mixed helium-iodine plume at $t = 64$ ms: (a) schlieren view with plume center line marked in white, (b) Beer-Lambert Law processed spectrometer view representing absorption with center line marked in white and regions of interest at 530 nm and 650 nm outlined in green and red, respectively, and (c) LOS integrated absorbance at both wavelengths of interest. It should be noted that the image in (b) has been brightened by a value of 0.3 for easier visualization.

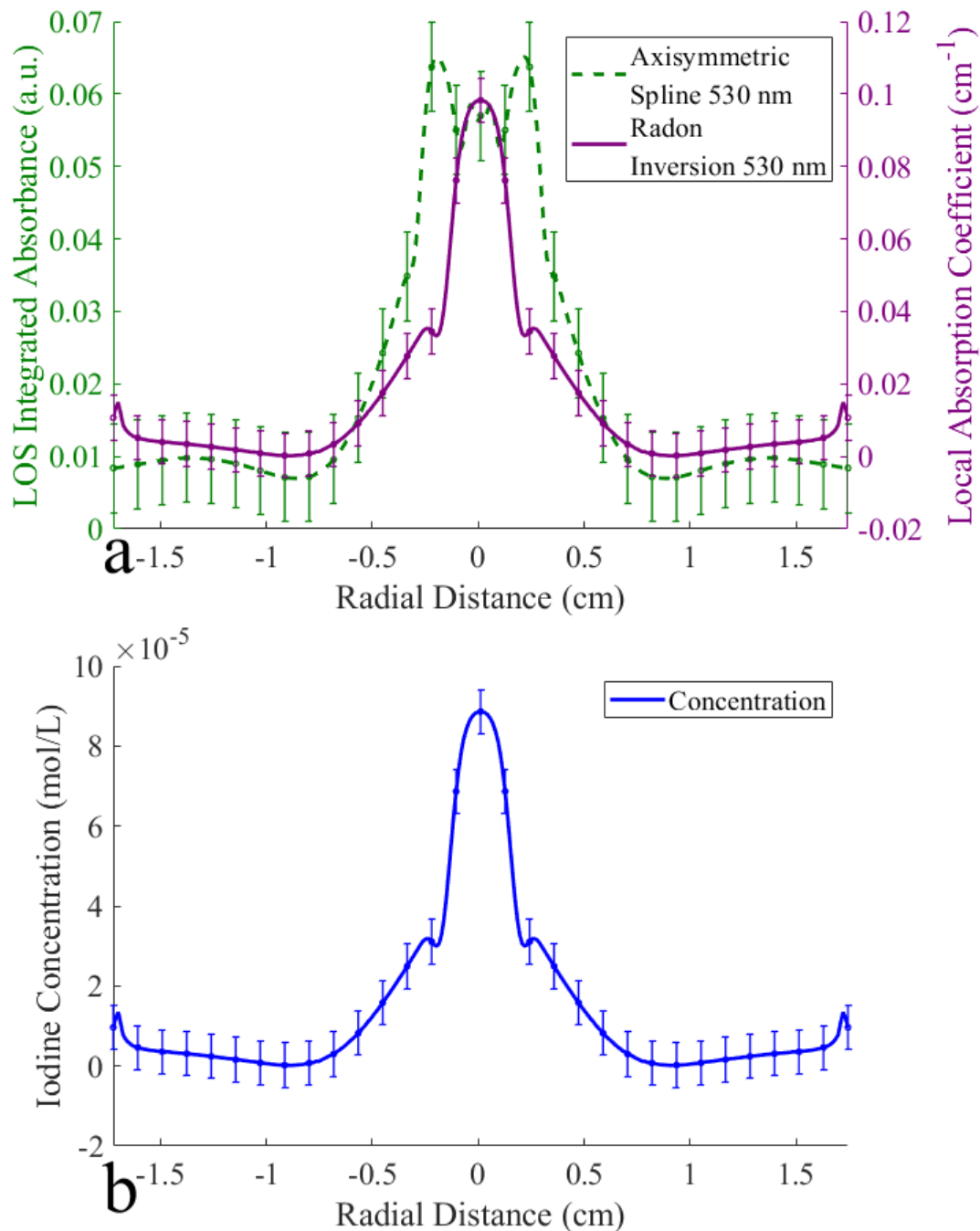


Figure 4.9: Processed data for a mixed helium-iodine plume at $t = 64$ ms: (a) Axisymmetric spline fit of LOS integrated absorbance at 530 nm (green dashed line) and the corresponding Radon inverted radial absorption coefficient, $\alpha(x, y)$, at 530 nm (purple), and (b) concentration of iodine gas calculated from $\alpha(x, y)$ using Equation 4.12.

approximately 200 cm, which was enough distance to promote mixing but also enough to deposit iodine along the way. Furthermore, the calculated maximum concentration value within the test section was determined based on an ideal circumstance where all of the iodine gas was picked up at once by the helium gas and carried at once to the test section. The more realistic scenario was that small amounts of the gas were picked up at a time by the helium gas passing through the iodine heating chamber. Therefore, smaller doses of iodine reached the test section at a time rather than all the iodine gas possibly produced by the amount of solid iodine particles used for that particular test, until eventually all of the iodine was carried into the test section. This was supported by visual inspection of the iodine chamber upon cooling, where a significant amount of iodine was layered on the walls of the chamber. Another factor was the significant difference in the size of the two elements physically. Iodine gas, as a diatomic molecule, is much larger than helium gas. leading to non-ideal mixing conditions, and therefore not as much iodine would be picked up by the passing helium flow as expected.

4.3.2 Mole fractions and spectrometer-based density reconstruction

With the concentration of trace iodine calculated across the plume, the density field was then reconstructed. This was done for both test cases of a pure helium-only plume and a mixed helium-iodine plume under the assumption of a sharp-edged plume boundary. The values calculated from the spectrometer data were used to predict what the measurements of density should be using a quantitative schlieren approach.

For both test cases, the gas density, ρ , at any given point inside or outside the plume was first calculated using the ideal gas equation:

$$\rho(r) = \frac{P \cdot M(r)}{R_u \cdot T(r)} \quad (4.16)$$

where P is the atmospheric pressure (Pa), $M(r)$ is the molar mass of the gas mixture at each point r across the field of view (kg/mol), R_u is the universal gas constant (8.3145 J/mol · K), and $T(r)$ is the local gas temperature (K) at each point across the field of view.

In the helium-only model, the plume was assumed to consist of purely helium with a known radius (inside r_{plume}), and purely air outside that region. The temperature and molar mass fields $T(r)$ and $M(r)$ vary between the plume region and the ambient surroundings, depending on the model. The molar mass was defined as:

$$M_{\text{He-only}}(r) = \begin{cases} M_{\text{He}}, & |r| \leq r_{\text{plume}} \\ M_{\text{air}}, & |r| > r_{\text{plume}} \end{cases} \quad (4.17)$$

Similarly, the temperature was defined as a step function:

$$T(r) = \begin{cases} T_{\text{plume}}, & |r| \leq r_{\text{plume}} \\ T_{\text{air}}, & |r| > r_{\text{plume}} \end{cases} \quad (4.18)$$

Using these definitions and Equation 4.16, the helium-only density profile was computed.

In the second case, the plume was assumed to be a helium–iodine mixture. Trace iodine concentration measurements $\bar{c}_{\text{I}_2}(r)$ (mol/m³) were obtained from spectroscopic absorption data and used to compute the local molar mass of the gas.

First, the total molar concentration of the gas mixture inside the plume was estimated using the ideal gas law:

$$\bar{c}_{\text{total}} = \frac{P_{\text{plume}}}{R_u \cdot T_{\text{plume}}} \quad (4.19)$$

where \bar{c}_{total} served as an appropriate starting point for iterating the true value of \bar{c}_{total} within the plume until the average difference in density values between schlieren and spectrometer data were minimized. The plot of schlieren versus spectrometer data for the mixed helium iodine plume is provided and discussed later in Figure 4.13. It was found that this initial approximation of \bar{c}_{total} was within approximately 2% of its ideal value. Figure 4.10 shows the range of \bar{c}_{total} values used and the corresponding density differences between the schlieren and spectrometer data. The following calculation steps were performed for each \bar{c}_{total} value until it was optimized.

Using the values of \bar{c}_{total} , the local mole fractions of iodine and helium were calculated as:

$$X_{\text{I}_2}(r) = \frac{\bar{c}_{\text{I}_2}(r)}{\bar{c}_{\text{total}}} \quad (4.20)$$

$$X_{\text{He}}(r) = 1 - X_{\text{I}_2}(r) \quad (4.21)$$

The local molar mass of the helium–iodine mixture was then calculated as:

$$M_{\text{mix}}(r) = X_{\text{He}}(r) \cdot M_{\text{He}} + X_{\text{I}_2}(r) \cdot M_{\text{I}_2} \quad (4.22)$$

Outside the plume region (i.e., for $|r| > r_{\text{plume}}$), the molar mass was set to that of air, and the local molar mass field was defined as:

$$M(r) = \begin{cases} M_{\text{mix}}(r), & |r| \leq r_{\text{plume}} \\ M_{\text{air}}, & |r| > r_{\text{plume}} \end{cases} \quad (4.23)$$

The local temperature was assigned similarly to the helium-only case:

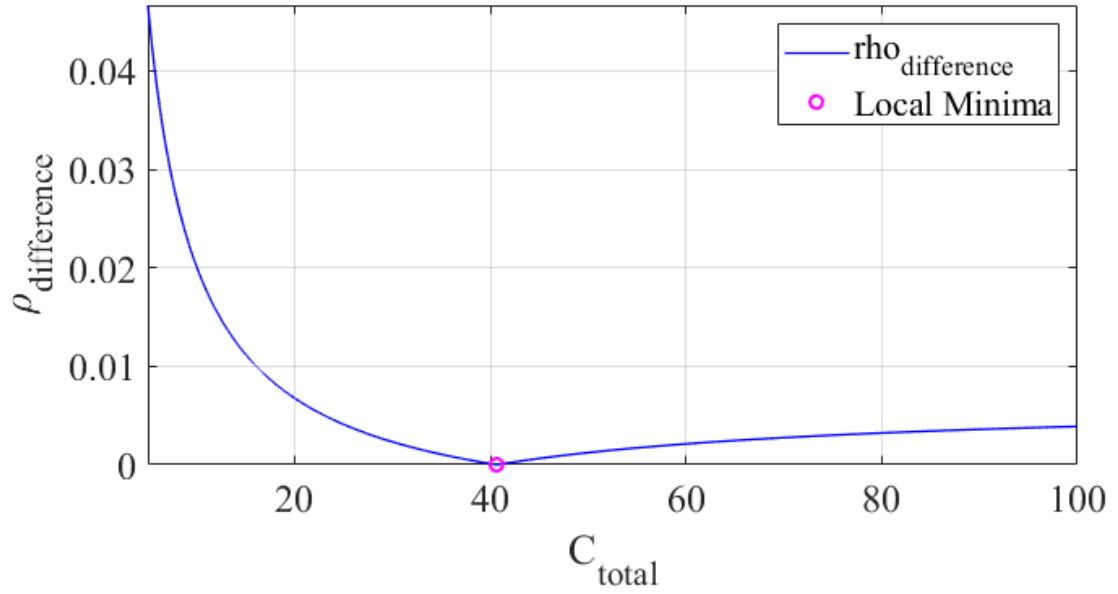


Figure 4.10: Optimization of \bar{c}_{total} value to minimize difference in density values calculated for mixed helium iodine plume using purely spectrometer based and refractive imaging based data.

$$T(r) = \begin{cases} T_{\text{plume}}, & |r| \leq r_{\text{plume}} \\ T_{\text{air}}, & |r| > r_{\text{plume}} \end{cases} \quad (4.24)$$

The resulting gas density profile incorporating iodine traces was then calculated using Equation 4.16. The densities resulting from these calculations, based exclusively on spectrometer measurements for a helium-only and a mixed helium-iodine plume, are shown in Figure 4.11.

4.3.3 Schlieren-based density reconstruction

With an initial prediction of plume densities made using purely spectrometer-based data, the densities were then reevaluated from the corresponding schlieren images of the plumes. The concentration values calculated from the spectrometer images were used together with basic refractive imaging concepts to reconstruct the local density field within gas plumes for both test cases. For both cases (helium-only versus mixed helium-iodine plumes), refractive index fields were derived from schlieren imaging and then related to local gas mixtures. Measurements were taken from the center row of the region of the schlieren image viewed by the imaging spectrometer to correlate measurements taken with the spectrometer versus the schlieren images. Measurements were also taken from the centerline of

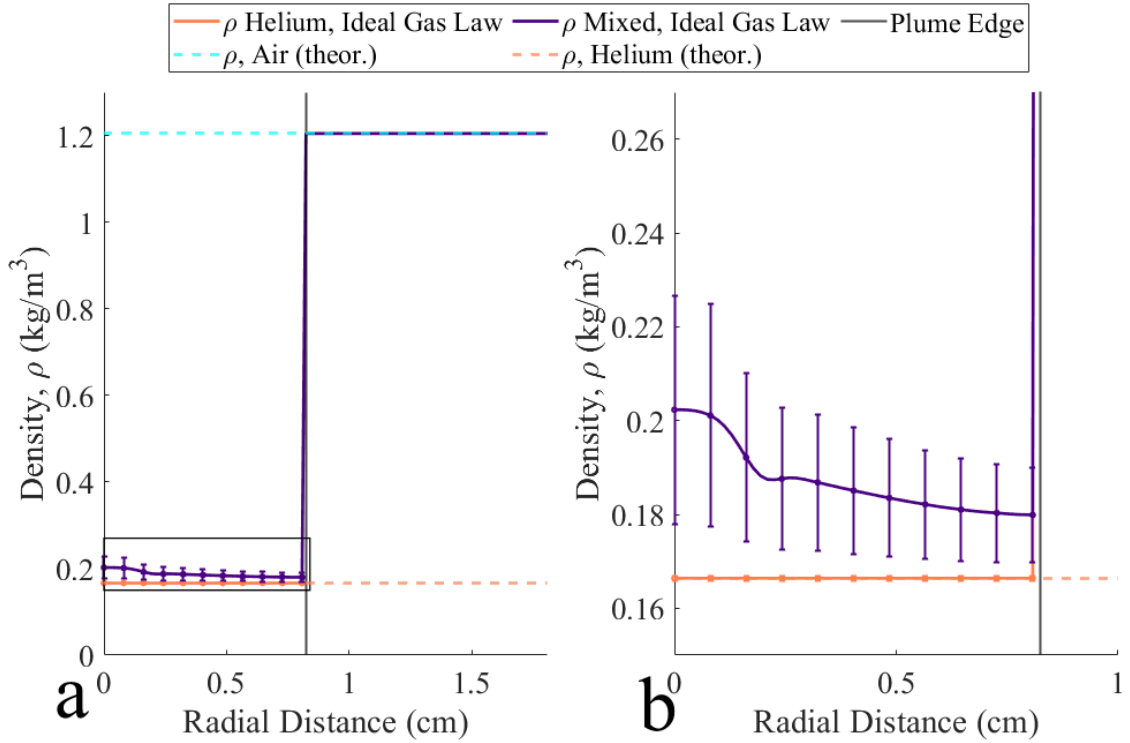


Figure 4.11: Comparison of density fields reconstructed using pure spectrometer data and ideal gas law: (a) density field calculated for a pure helium and a mixed helium-iodine plume with region of interest outlined by black box, and (b) a closer view of density behavior inside region of interest.

the plume outward in the schlieren image rather than across the entire plume in order to simplify data processing using the Abel inversion transform.

In the case of a pure helium plume, the Gladstone-Dale relation (Equation 3.8) provided a direct linear relationship between the refractive index and the mass density of helium. The refractive index deviation from the ambient background air was first obtained from the schlieren image of the plume using the process described in Section 3.4. The refractive index was then used in combination with the Gladstone-Dale coefficients (κ) of helium and air to calculate the density inside versus outside the plume:

$$\rho(r) = \begin{cases} \frac{n_{He}-1}{\kappa_{He}}, & |r| \leq r_{\text{plume}} \\ \frac{n_{air}-1}{\kappa_{air}}, & |r| > r_{\text{plume}} \end{cases} \quad (4.25)$$

The resulting density field across the pure helium plume is provided in Figure 4.12. It is shown alongside the helium density field calculated purely from spectrometer data for comparison.

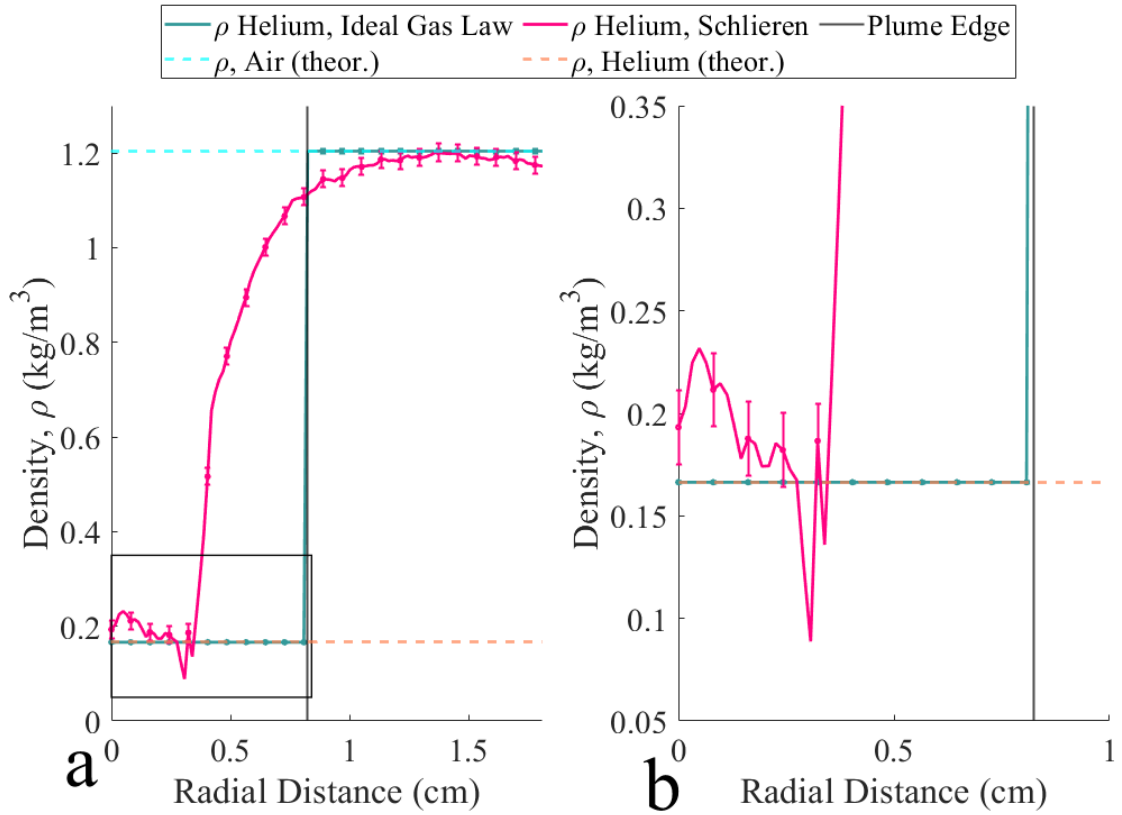


Figure 4.12: Pure helium plume comparison of density reconstruction methods: (a) density field calculated across plume using values obtained first through the spectrometer and then through schlieren imaging with region of interest outlined by black box, and (b) a closer view of density behavior inside region of interest.

When iodine was introduced into the helium flow as a trace species, the refractive index became a function of both helium and iodine densities. Because iodine has a much higher molar mass and Gladstone-Dale coefficient than helium, even small amounts were expected to significantly alter the refractive index field. This made it essential to account for iodine separately to avoid overestimating the plume density field.

In a binary mixture, the total refractive index is expressed as the sum of contributions from each species via the additive Gladstone–Dale law [65]. The total combined refractive index as well as the combined Gladstone-Dale coefficient were calculated using the same molar fraction values determined above from spectrometer measurements:

$$n_{plume}(r) = X_{He}(r) \cdot n_{He}(r) + X_{I_2}(r) \cdot n_{I_2}(r) \quad (4.26)$$

$$\kappa_{plume}(r) = X_{He}(r) \cdot \kappa_{He} + X_{I_2}(r) \cdot \kappa_{I_2} \quad (4.27)$$

Once the index of refraction and the Gladstone-Dale coefficient within the plume boundary were calculated, they were implemented as follows to calculate the total density field across the plume:

$$\rho(r) = \begin{cases} \frac{n_{plume}-1}{\kappa_{plume}}, & |r| \leq r_{plume} \\ \frac{n_{air}-1}{\kappa_{air}}, & |r| > r_{plume} \end{cases} \quad (4.28)$$

The resulting density profile across the mixed helium iodine plume is provided in Figure 4.13. It is shown alongside the mixed density field calculated purely from spectrometer data for comparison. The values of the two mixed plume density fields were compared to minimize the average difference in density at the plume centerline to iterate the value of \bar{c}_{total} as discussed previously.

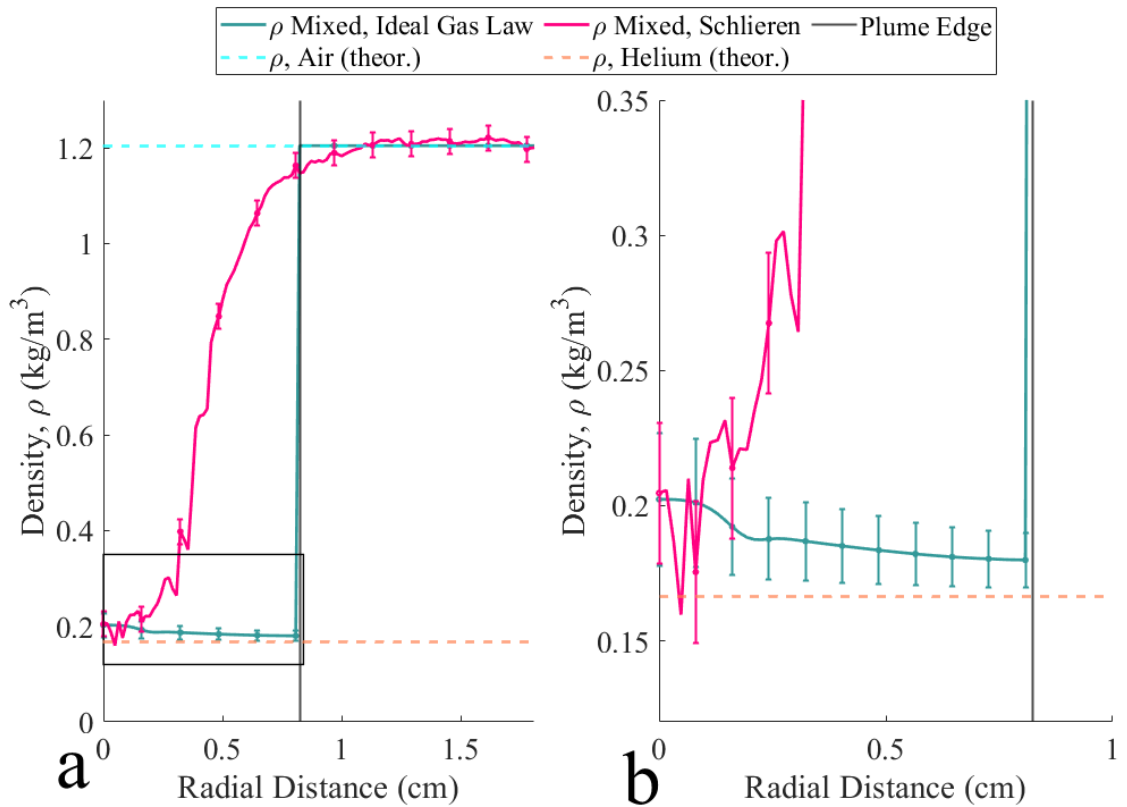


Figure 4.13: Mixed helium-iodine plume comparison of density reconstruction methods: (a) density field calculated across plume using values obtained first through the spectrometer and then through schlieren imaging with region of interest outlined by black box, and (b) a closer view of density behavior inside region of interest. These were the final density values compared to optimize \bar{c}_{total} .

To isolate the effect of iodine concentration on the local gas density calculated from schlieren measurements, a comparison of the density values calculated before versus after accounting for the addition of iodine in the mixed plume is also provided in Figure 4.14. While the concentration of iodine was small relative to the total amount of gas present, it still produced a visible and quantifiable difference in the calculated density field.

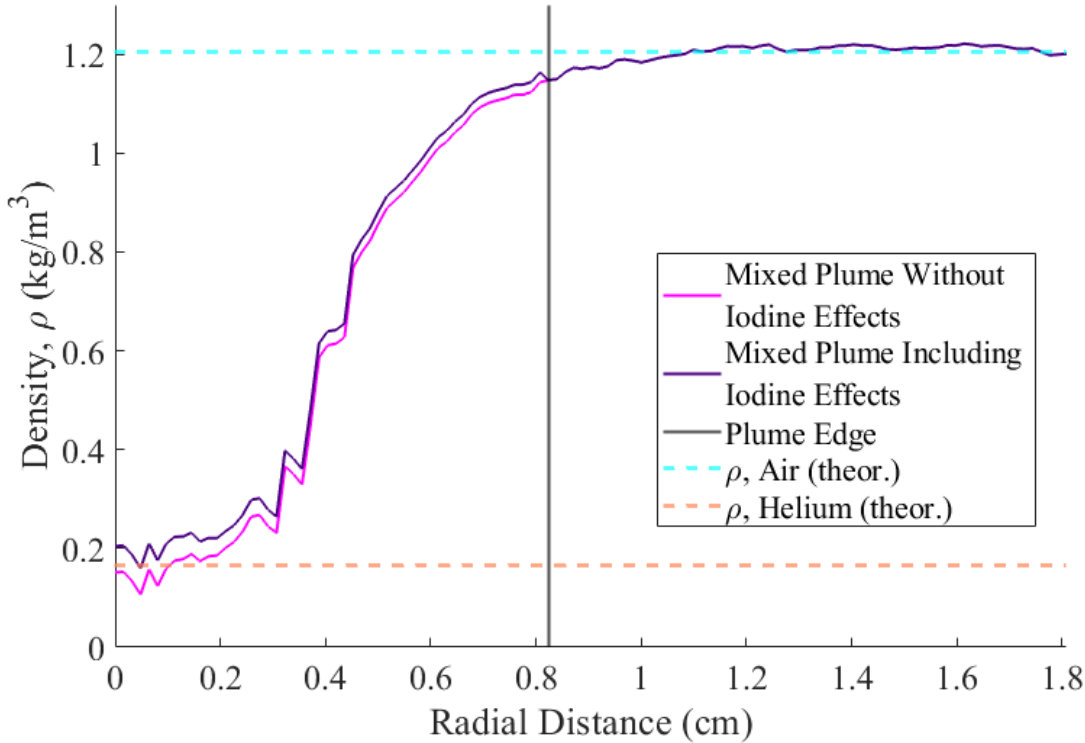


Figure 4.14: Comparison of density field calculated through schlieren measurements of a mixed helium iodine plume, before versus after accounting for the addition of a small iodine concentration as measured through spectrometer data.

A final comparison was then made between density field calculations produced for both test cases using the modified refractive imaging analysis. This comparison is shown in Figure 4.15.

4.4 Error calculations

As values were passed through each step of the calculation process, the propagation of errors was also tracked to quantify the uncertainty of the final values presented here. A statistical error propagation methodology was applied to the measurements to track this uncertainty.

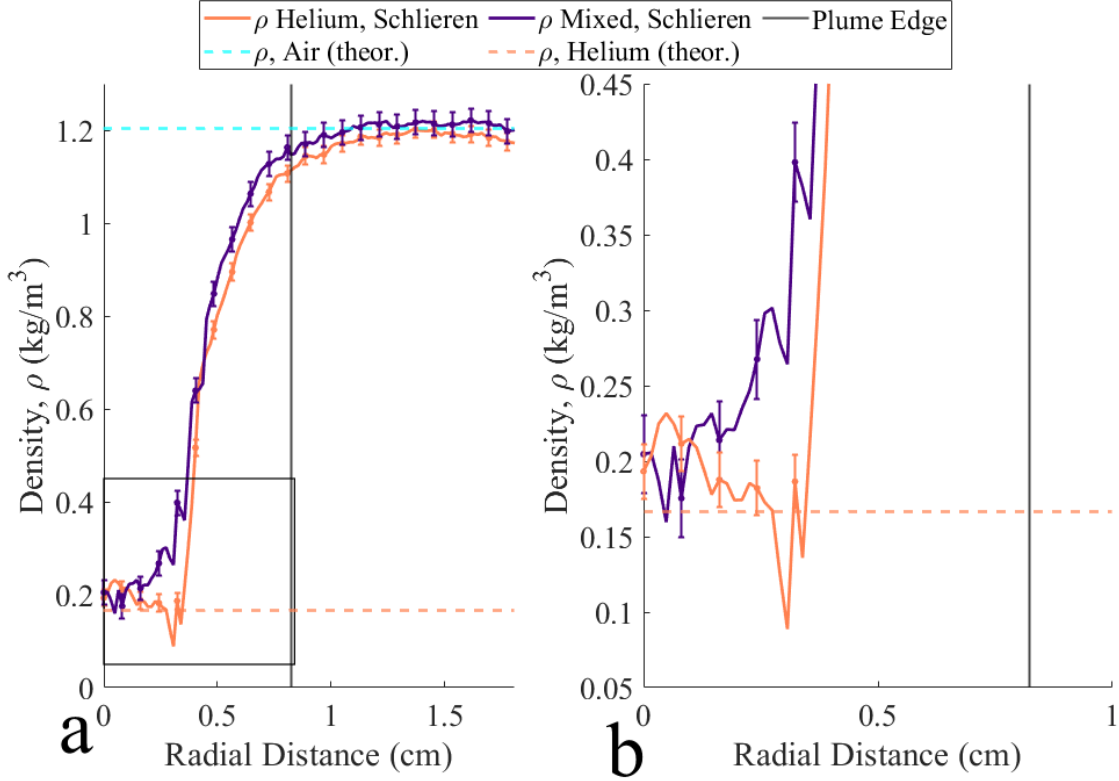


Figure 4.15: Comparison of density fields reconstructed using schlieren imaging in combination with spectroscopic measurements: (a) density fields calculated for a pure helium and a mixed helium-iodine plume with region of interest outlined by black box, and (b) a closer view of density behavior inside region of interest.

4.4.1 Error associated with spectrometer measurements

Sources of error associated with spectrometer measurements were due to background noise in the spectral images and the smoothing methods applied. Uncertainty propagation of measurements was performed under linear error assumptions. Uncertainties were calculated independently for measured values.

The uncertainty in absorption, A , is given by:

$$\sigma_A = \frac{1}{\ln(10)} \sqrt{\left(\frac{\sigma_I}{I}\right)^2 + \left(\frac{\sigma_{I_0}}{I_0}\right)^2} \quad (4.29)$$

where I and I_0 are statistically independent. The values σ_I and σ_{I_0} were determined experimentally from noise floor estimates.

To reduce noise and extract a smooth signal before applying the inverse Radon transform, the absorption profiles $A(x)$ were smoothed using the cubic smoothing splines. The uncertainty in the smoothed curve $\tilde{A}(x)$ was approximated by:

$$\sigma_{\tilde{A}}(x) = b_s \cdot \tilde{A}(x) \quad (4.30)$$

where b_s is an empirically chosen bias term representing the relative uncertainty introduced by smoothing. From there, the error propagation was considered linear through the Radon inversion and concentration calculations, and the uncertainty was scaled accordingly.

Following the determination of species concentration through absorption measurements, the density field was first calculated purely through the ideal gas law and spectroscopic measurements. Assuming P , M , and T are independent, the uncertainty in ρ was determined by standard propagation of errors of each:

$$\sigma_{\rho} = \rho \cdot \sqrt{\left(\frac{\sigma_P}{P}\right)^2 + \left(\frac{\sigma_M}{M}\right)^2 + \left(\frac{\sigma_T}{T}\right)^2} \quad (4.31)$$

where σ_P , σ_M , and σ_T are the uncertainties in pressure, molar mass, and temperature, respectively. The value of σ_M was calculated as follows:

$$\sigma_{X_I} = \left| \frac{\partial X_I}{\partial C_I} \right| \cdot \sigma_{C_I} = \frac{\sigma_{C_I}}{C_{\text{tot}}} \quad (4.32)$$

$$\sigma_M = |M_I - M_{\text{He}}| \cdot \sigma_{X_I} \quad (4.33)$$

where C_{tot} is the total molar concentration of the gas mixture. If C_{tot} is constant or known (e.g., from background air), this becomes straightforward to compute. The uncertainty in X_I is related to the uncertainty in measured iodine concentration C_I .

In addition to the analytical propagation, a conservative uncertainty estimate can be obtained by computing the density from the upper and lower bounds of inputs:

$$\sigma_{\rho} \approx \frac{\rho_{\text{max}} - \rho_{\text{min}}}{2} \quad (4.34)$$

This bounding approach is useful when input distributions are not known or are asymmetric. This method was implemented in this data processing as a fallback estimate.

4.4.2 Error associated with schlieren measurements

Sources of error from schlieren measurements were mainly associated with background noise and calculations of deflection angle and refractive index. Uncertainty in the deflection angle ε is given by:

$$\sigma_\varepsilon = \left| \frac{\partial \varepsilon}{\partial \Delta x} \right| \sigma_{\Delta x} = \left| \frac{1}{f \left(1 + \left(\frac{\Delta x}{f} \right)^2 \right)} \right| \cdot \sigma_{\Delta x} \quad (4.35)$$

where Δx is the pixel displacement in the calibration lens, f is the focal length of the calibration lens, and $\sigma_{\Delta x}$ includes contributions from background intensity noise and errors in the fit used to map pixel intensity to calibration lens location.

The change in refractive index is derived from Abel inversion of the refraction angle field. The uncertainty in this inverted value ($\Delta n = n(r) - n_0$) is approximated as:

$$\sigma_{\Delta n} \approx \sigma_\varepsilon \quad (4.36)$$

which assumes a linear relationship through the Abel inversion. The uncertainty in the local refractive index field ($n = n_0 + \Delta n$) is then defined as:

$$\sigma_n = \sigma_{\Delta n} \quad (4.37)$$

assuming n_0 , the zero refraction condition, is precisely known.

The uncertainty in the density field calculated from the Gladstone Dale law is then defined as:

$$\sigma_\rho = \sqrt{\left(\frac{\sigma_n}{\kappa_{\text{mix}}} \right)^2 + \left(\frac{(n-1) \cdot \sigma_{\kappa_{\text{mix}}}}{\kappa_{\text{mix}}^2} \right)^2} \quad (4.38)$$

This accounts for uncertainty in both the refractive index measurement and the empirical κ coefficient in relation to the concentration values used to calculate κ . The uncertainty of κ is then defined as:

$$\sigma_{\kappa_{\text{mix}}} = \sqrt{\sum_i \kappa_i^2 \cdot \sigma_{X_i}^2} \quad (4.39)$$

4.5 Final results and discussion

The results from the simultaneous schlieren and imaging spectroscopy setup showed strong agreement between density field values predicted through spectroscopy measurements and through the modified quantitative schlieren process for both test cases of a pure helium and a mixed helium-iodine plume. The imaging spectrometer data was first processed to quantify the local iodine concentration within mixed plumes. This information was derived from absorbance using the Beer-Lambert Law. These calculated concentration values were used to calculate

density with the basic principles of the ideal gas law. The concentration calculations were then combined with Gladstone-Dale coefficients to reconstruct the true refractive index field and therefore the density field across the plume.

Despite the small amount of iodine present relative to the total mass of the gas plume, the introduction of iodine caused a noticeable and measurable shift in the refractive index and gas density values. This indicated that even minor concentrations of heavier species, such as iodine, have significant visual and quantitative impacts on optical diagnostic results. Furthermore, it was observed that the density profiles reconstructed purely from spectrometer-based calculations and those obtained through the combination of schlieren imaging and spectroscopic concentration values were highly similar. Discrepancies between the two reconstructions were within reasonable uncertainty ranges and highlighted the capabilities of the combined imaging approach.

Several sources of error were identified and considered when interpreting the results. Both the schlieren and spectrometer images showed small intensity fluctuations that introduced uncertainty into the absorbance and refraction angle calculations. These fluctuations were quantified and included in error calculations. While these fluctuations were present, the errors they introduced were small in relation to the measurement signals being recorded, and therefore did not cause significant issues in data processing and interpretation. A more significant contributor to the error was the presence of the shadowgraph effect in the spectrometer data. This effect however was also isolated and accounted for through normalization and baseline subtraction as previously discussed. Uncertainties in spectroscopic calibration, refractive index determination, and concentration estimation propagate through to the final density field calculations. The final density uncertainty was approximated by standard propagation of error methods applied to the measurements of absorbance, path length, pressures, and temperature. Over the course of the approximately 15 tests performed using this setup, the range of calculated concentration and density values were within the same order of magnitude, as were the uncertainties calculated.

The assumption of full helium-iodine mixing was a non-negligible source of error leading to density calculations. The analysis performed here assumed that iodine was fully mixed within the helium by the time it reached the test section. However, fluctuations in concentration measurements observed suggest that localized variations in composition could have contributed to small deviations in density field reconstruction.

The successful validation between the two different quantification methods supports the reliability of the dual diagnostic approach further developed in this research. The combined method demonstrates potential for reconstructing density fields in other future multi-species optically transparent flows.

CHAPTER 5

DATA, RESULTS, AND DISCUSSION FOR COLOR-FILTERED SCHLIEREN FOR DETERMINING DENSITY FIELD OF HELIUM-IODINE PLUME

The goal of the color-filtered schlieren test setup was to obtain similar spectroscopic information as in Chapter 4 without the use of the imaging spectrometer. That information was then used to determine the overall properties within the flow field, including the density field throughout the plume. The steps to analyzing the gas plumes at each wavelength allow for leveraging the differences in light refraction and absorption at both wavelengths to calculate overall properties throughout the flow field. The entire process is outlined from start to finish by the flowchart in Figure 5.1. It should be noted that the plume images in Figure 5.1 are displayed in green and red to represent their color wavelengths of 530 nm and 650 nm, respectively. The actual images, however, were all captured in grayscale. Color filters were applied during image processing in order to more clearly describe the flow of each data type in the flow chart.

5.1 Determination of baseline refraction angles using helium-only plume

The first step in processing the simultaneous color-filtered schlieren data was to determine the approximate expected baseline refraction angles measured across a basic helium-only plume. To do this, the intensities of the pixels were measured in the region of the plume described in Figures 5.2 a and b. The values in this region were measured along a chosen center row (horizontal green and red lines on images captured at 530 nm and 650 nm, respectively) from the center line of the plume (white) outward past the plume edge (dashed cyan) to the analysis region end point (magenta). This select region was chosen as opposed to the entire image so that both the Abel inversion transform and the inverse Radon transform could be more easily performed during data processing. As shown in Figure 5.2 a and b, the same region was analyzed in both the 530 nm and 650 nm images. The measured intensity values were used to calculate the refraction angle, ϵ , across the plume. These were calculated using the previously described method of using the calibration lens curves to relate the intensity to the angle of refraction for each data set. These calculated ϵ values are shown in Figure 5.2 c. The ϵ values calculated from the 530 nm and 650 nm images are plotted with green and red

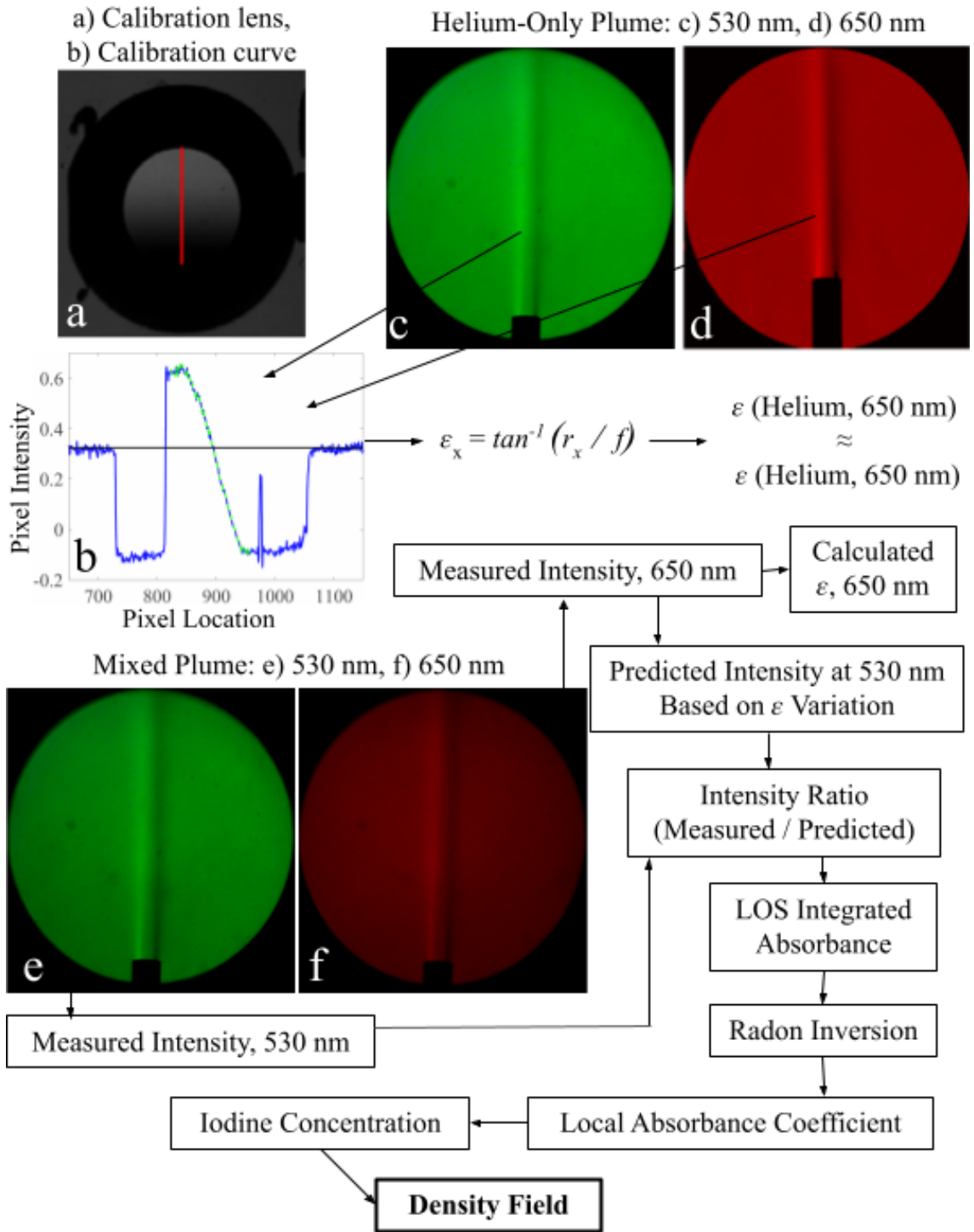


Figure 5.1: Flow chart detailing methods of data processing used for density reconstruction.

lines, respectively. The line colors match the visible color corresponding to those wavelengths.

The plume images in Figure 5.2 a and b, captured at 530 nm and 650 nm, respectively, visibly vary in overall pixel intensity. However, they each view the same moment of the event captured within the test section. Since the absorbance of the working gas (pure helium) was already deemed negligible at these wavelengths, any differences in the calculated ϵ values between the two images were deemed more the result of error propagation than absorption effects. This was because of the naturally low absorbance of helium at these two wavelengths of interest. The presence of helium resulted in different refraction values than what a pure air plume would have produced, however, this difference was taken into account in later data processing steps. Note here in Figure 5.2 c that the two curves representing calculated ϵ values are very closely aligned. This is due to the lack of significant change in refraction between 530 nm and 650 nm due to the gas species present. While the exact values calculated from each data set did vary slightly, these values provided an approximate baseline of the refraction expected due to the presence of a helium plume moving through the given test section.

Some of the differences between the two curves were attributed to differences in noise introduced in the individual data sets. Since they were taken by two separate cameras simultaneously, there was always some uncertainty between the two measurements, even when both cameras were viewing the same event. The matched cameras had the same type of sensor. However, each individual camera sensor naturally has minor differences. During data pre-processing, when the two images were aligned using MATLAB's *imregister* function as described in Section 3.3, a small amount of approximation and interpolation was performed in order to seamlessly transition one image to match the other in sizing and positioning. This could have adjusted the pixel values just enough to introduce additional minor value differences. Although this does cause more uncertainty within the data overall, the differences between the two plots were significantly smaller than the intentional differences that were expected later on in data processing, and therefore were largely negated. These differences were also captured when comparing the two views of the pure helium plume.

5.2 Refraction and image intensity prediction using helium baseline

Moving forward, the same process was used to measure pixel intensities and calculate ϵ values across the same region of an iodine-infused helium plume. The region of the plume analyzed for this data set is outlined in Figure 5.3 a. Only the 650 nm plume view was analyzed at first. It was known that there was trace iodine gas present within the plume moving through the test section based on visual inspection and identification. However, the 650 nm plume image was captured at the wavelength of assumed zero absorption due to iodine gas. Because of this, the intensity values measured across the plume were assumed to be unaffected by the

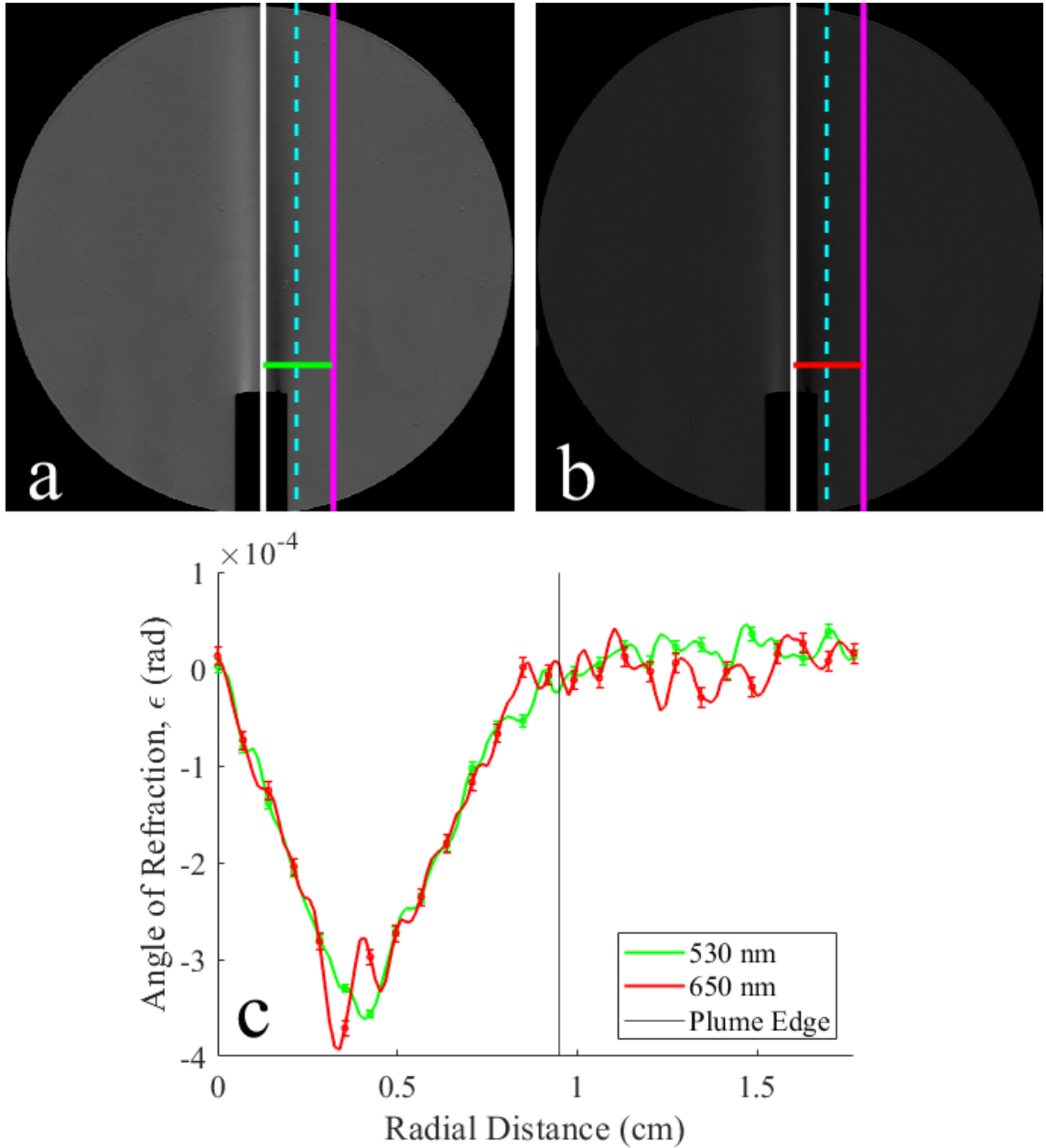


Figure 5.2: Baseline refraction angle of light was calculated using helium-only plume moving through in test section: (a) 530 nm view of plume, (b) 650 nm view of plume, and (c) calculated refraction angle (ϵ) values at both wavelengths. In parts a and b, the centerline is white, the edge of the plume is cyan, the end of the analysis region is magenta, and the center row analyzed is outlined in green and red for 530 nm and 650 nm (a and b) respectively.

presence of iodine. The calculated ϵ values from quantitative schlieren across the 650 nm iodine-infused plume are shown in Figure 5.3 b.

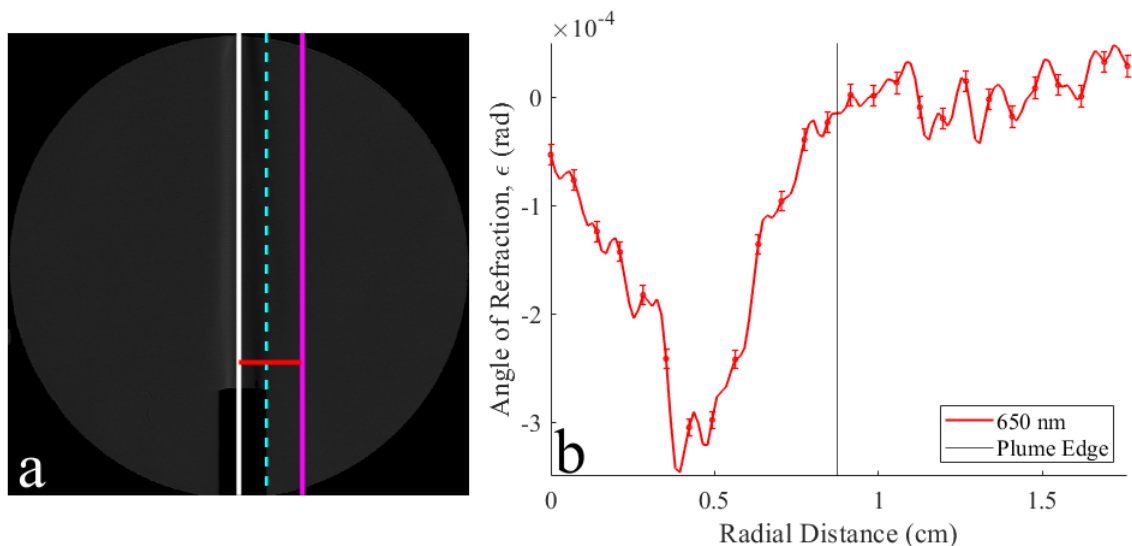


Figure 5.3: (a) Schlieren view of mixed plume at 650 nm with analysis region shown by the red line. (b) Measured epsilon values across plume within outlined region.

When there is no iodine gas present in the plume, the angle of refraction at 530 nm and 650 nm is expected to be the same when calculated from the measured intensity values across the plume. Since the calculated ϵ at 650 nm in Figure 5.3 b theoretically shows no iodine effects, the plot can be used to predict what the epsilon across the same plume at 530 nm would be when assuming no iodine effects.

Knowing this, the ϵ values across the same region of the iodine-infused plume at 530 nm were first set as equal to those measured at 650 nm. From there, the calibration curve used to determine ϵ values from pixel intensities was used again to calculate intensity values based on the predicted ϵ values. This was done by altering Equations 3.5 and 3.6 to input ϵ and output position within the lens (r_x) as demonstrated in Equations 5.1 and 5.2:

$$R_x = r_x + r_{\text{avg}} \quad (5.1)$$

$$r_x = f \tan \epsilon_x \quad (5.2)$$

It should be noted that when determining original ϵ values at 650 nm, the 650 nm calibration curve was used. But after ϵ values at 650 nm and 530 nm values were set equal, in order to back out radial position within the calibration lens for the predicted 530 nm ϵ values, the 530 nm lens calibration curve was used. From there, the radial positions within the 530 nm lens were used to determine

the corresponding intensity values at those positions in the lens. This essentially provided a method of predicting what the 530 nm view of the iodine-infused plume should look like, assuming no iodine effects, based on the appearance of the 650 nm iodine-infused plume. The intensity values across the plume at 530 nm were estimated using the intensity values in the same region at 650 nm. A comparison between these predicted intensity values and the actual measured intensity values across the mixed plume at 530 nm is shown in Figure 5.4 b.

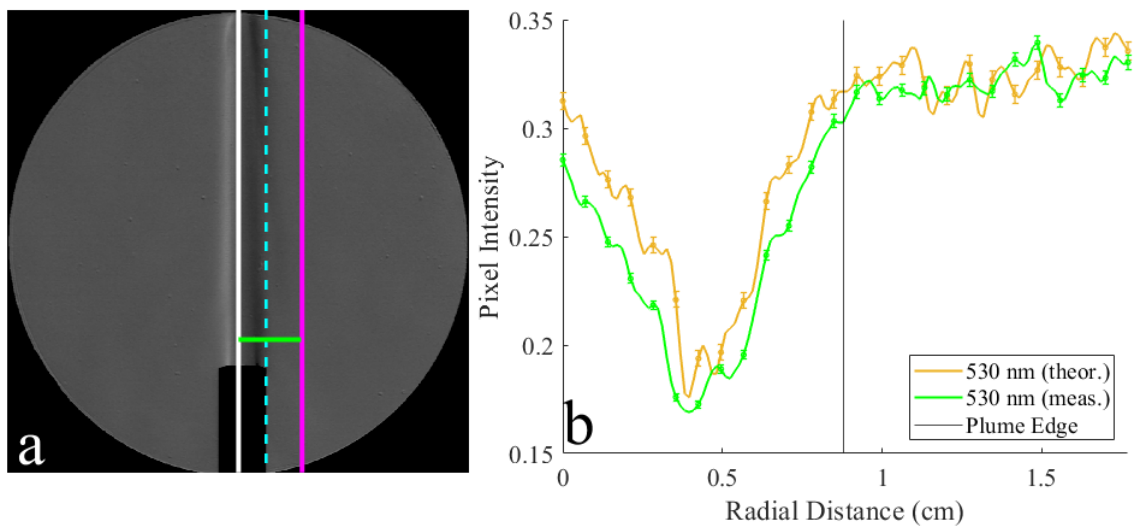


Figure 5.4: (a) Schlieren view of mixed plume at 530 nm with analysis region outlined. (b) Predicted versus measured intensities from same region of image, calculated using angles of refraction (ϵ).

The theoretically predicted intensity values were expected to be generally higher in value than the actual measured intensity values. The actual measured intensities from the 530 nm image were darker due to the added effect of light absorption due to the presence of iodine within the plume. A greater difference between the two plots was related to a greater concentration of iodine gas within the plume.

5.3 Absorbance deconvolution and concentration calculations

Determining both the baseline prediction of plume intensities assuming no absorption and the actual intensities of the plume allowed for a direct comparison to be made and related to light absorbance through the plume. A modified version of the Beer-Lambert Law was used here:

$$A = -\log \left(\frac{I_{530,measured}}{I_{530,theoretical}} \right) \quad (5.3)$$

Previously, the region of the spectrometer test image at 530 nm with refractive plume effects included was divided by the original transmitted intensity values at that wavelength. The same was true for values within the 650 nm range of the test image. Here, dividing simply by the background value of the schlieren image at each wavelength would not account for any of the refractive effects overlaid by the schlieren system. Instead, the intensity values predicted by those measured at 650 nm serve as a baseline of refraction effects without including absorption. Applying the Beer-Lambert Law to the ratio between the actual measured intensities and the predicted intensities highlights the differences in intensity caused by iodine absorption while effectively canceling out the effects caused exclusively by refraction. The 650 nm prediction serves as a “background” refractive condition, so that when the actual measurement is divided by that, the result leaves only absorption effects behind. This approach should thus yield a more accurate result. These LOS integrated absorbance values are shown in Figure 5.5 b.

With the LOS integrated absorbance calculated, the three-dimensional nature of the axisymmetric plume must still be taken into account. Similarly to how the raw spectrometer data was handled, a spline fit was developed for the raw LOS integrated absorbance data, and is shown in Figure 5.5 b alongside the original data. From there, the plot shape was reflected over the centerline to create an axisymmetric plot shape. Again, the inverse Radon transform was applied to these axisymmetric unit-less absorbance values to obtain the local absorption coefficient, α (cm^{-1}). The resulting α values are shown in Figure 5.6 a. The concentration values determined from α using Equation 4.12 are shown in Figure 5.6 b.

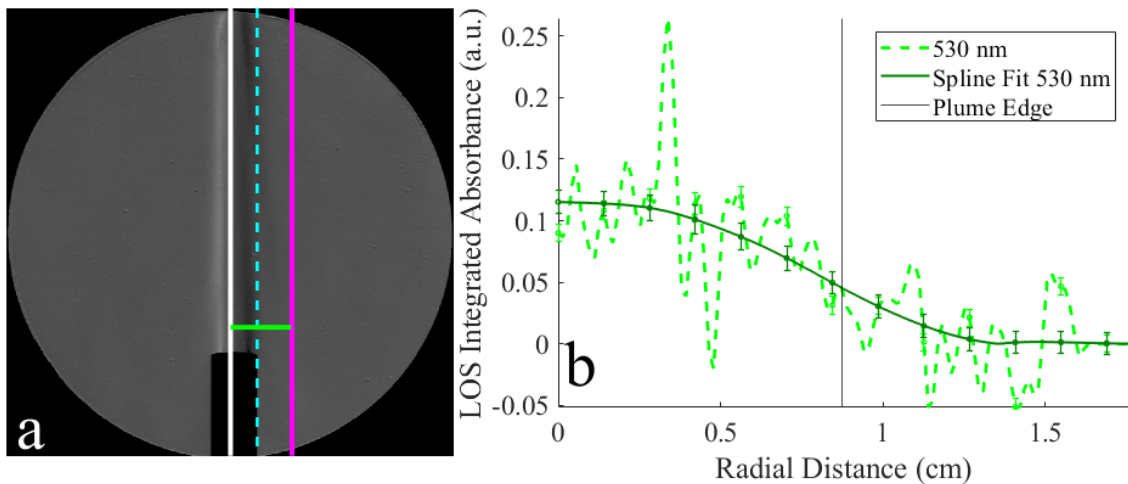


Figure 5.5: (a) Schlieren view of mixed plume at 530 nm with analysis region outlined. (b) Measured LOS integrated absorbance across analysis region of plume and spline fit of measured absorbance.

It should be noted that a comparison was also made between the absorption coefficient values calculated from the spline fit and those calculated from the raw,

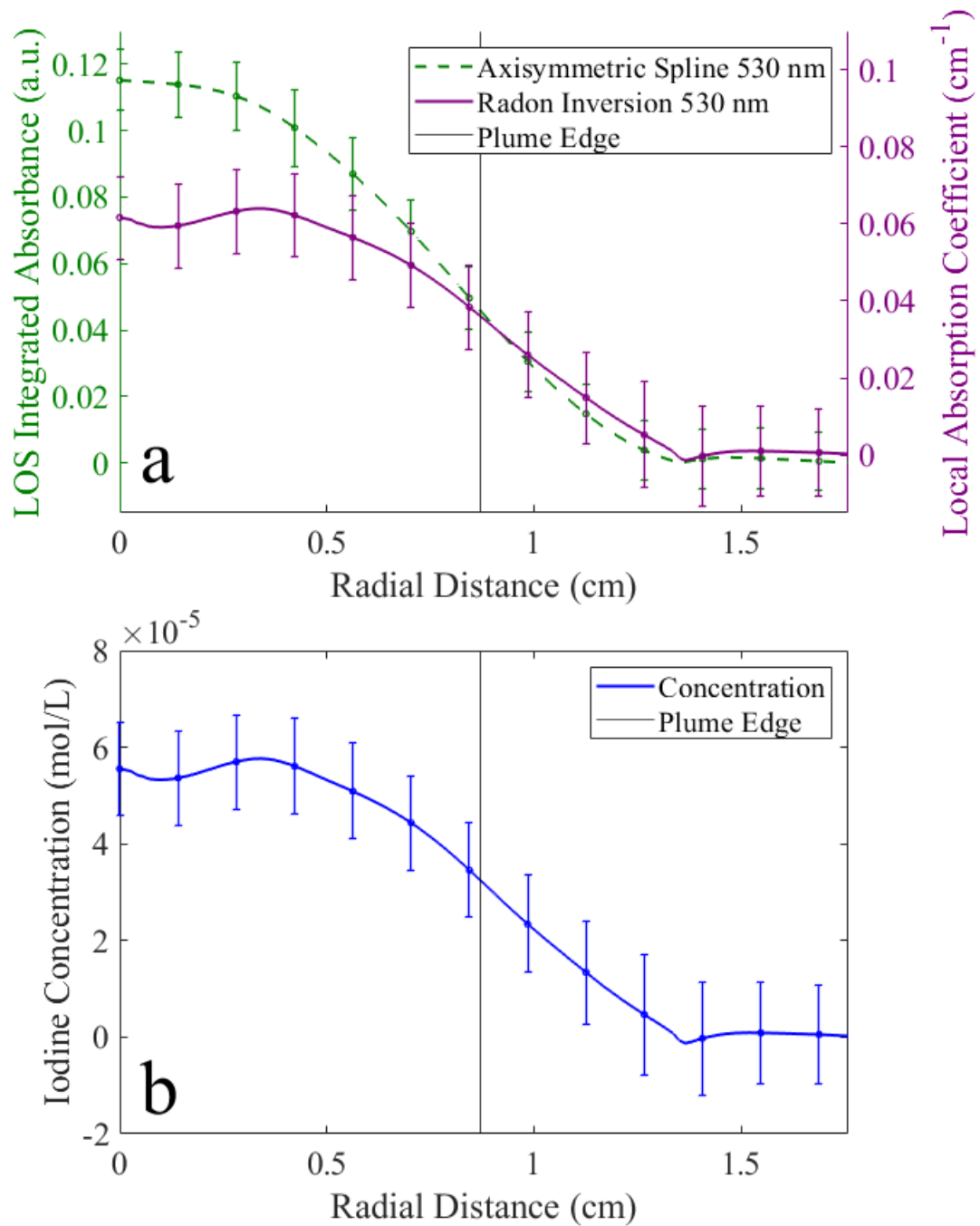


Figure 5.6: Processed schlieren data of a mixed helium-iodine plume at $t = 34$ ms: (a) Axisymmetric spline fit of LOS integrated absorbance at 530 nm (green dashed line) and the corresponding Radon inverted radial absorption coefficient, $\alpha(r)$, at 530 nm (purple), and (b) concentration of iodine gas calculated from $\alpha(r)$ using Equation 4.12.

unfitted data. Figure 5.7a provides a comparison between the LOS integrated absorbance values for a single row of the image, values averaged between 5 rows of the image, and the spline fit of those values. Figure 5.7b provides a comparison of each of those after applying the inverse Radon transform. It is clear that without applying a fit to the noisy data, the resulting local absorption coefficient has far too much variability to reasonably use in density calculations.

5.4 Density field reconstruction

Similarly to the schlieren data in Chapter 4, the iodine concentration values calculated were then used to reconstruct the overall density within the flow field. Equations 4.19, 4.20, 4.21, 4.26, 4.27 and 4.28 were used again here to calculate refractive indices and Gladstone–Dale coefficient values across the plume by accounting for the mole fractions of helium and iodine. The final density values calculated across the region of interest of the plume in this case are provided in Figure 5.8. While concentration calculations were made using a comparison of measurements taken at 530 nm and 650 nm, the final density calculations were made using refractive index values measured in the 650 nm view of the plume. This was because of the assumption that changes in refraction were captured at 650 nm without added absorption effects.

Once the process for evaluating concentration and density values was established, it was applied to a wider section of rows across the plume rather than a singular row. This was possible due to the axisymmetric and evenly mixed assumptions applied to the plumes. This resulted in concentration and density field maps across a larger region of the pure helium and mixed helium-iodine plumes. First, the density field for a pure helium plume was calculated and is pictured in Figure 5.9. The concentration of iodine throughout the mixed helium-iodine plume was then calculated and is pictured in Figure 5.10. The concentration values are all within the same order of magnitude as the values calculated for a single row of the plume, indicating iodine is relatively evenly mixed throughout the plume. The full density field for the mixed helium-iodine plume was then calculated and is pictured in Figure 5.11. For both plumes, the lowest density values were consistently measured along the centerline of the plume where the helium gas was most concentrated. In Figure 5.11, the density values approaching the centerline are visibly higher than those in Figure 5.9. This was due to the presence of the small concentration of iodine within the plume in Figure 5.11, demonstrating behavior consistent with Figure 5.8 throughout the plume. It should be noted that all calculations of error propagation were performed in the same manner as described previously in Section 4.4.

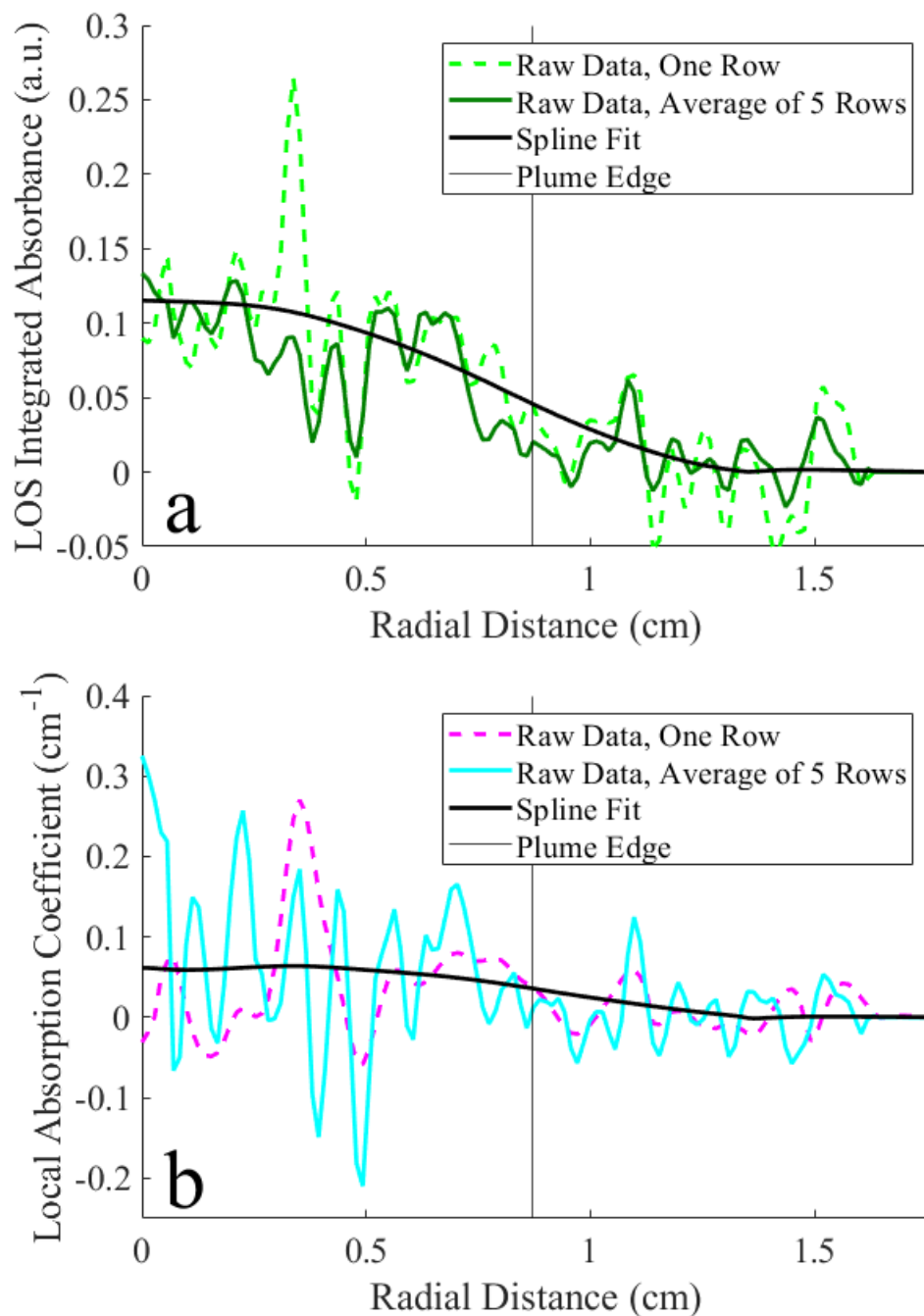


Figure 5.7: Comparison of effects of line fitting: (a) single row, averaged rows, and spline fit of LOS integrated absorbance data at 530 nm, and (b) corresponding Radon inverted radial absorption coefficient, $\alpha(r)$, for each measurement.

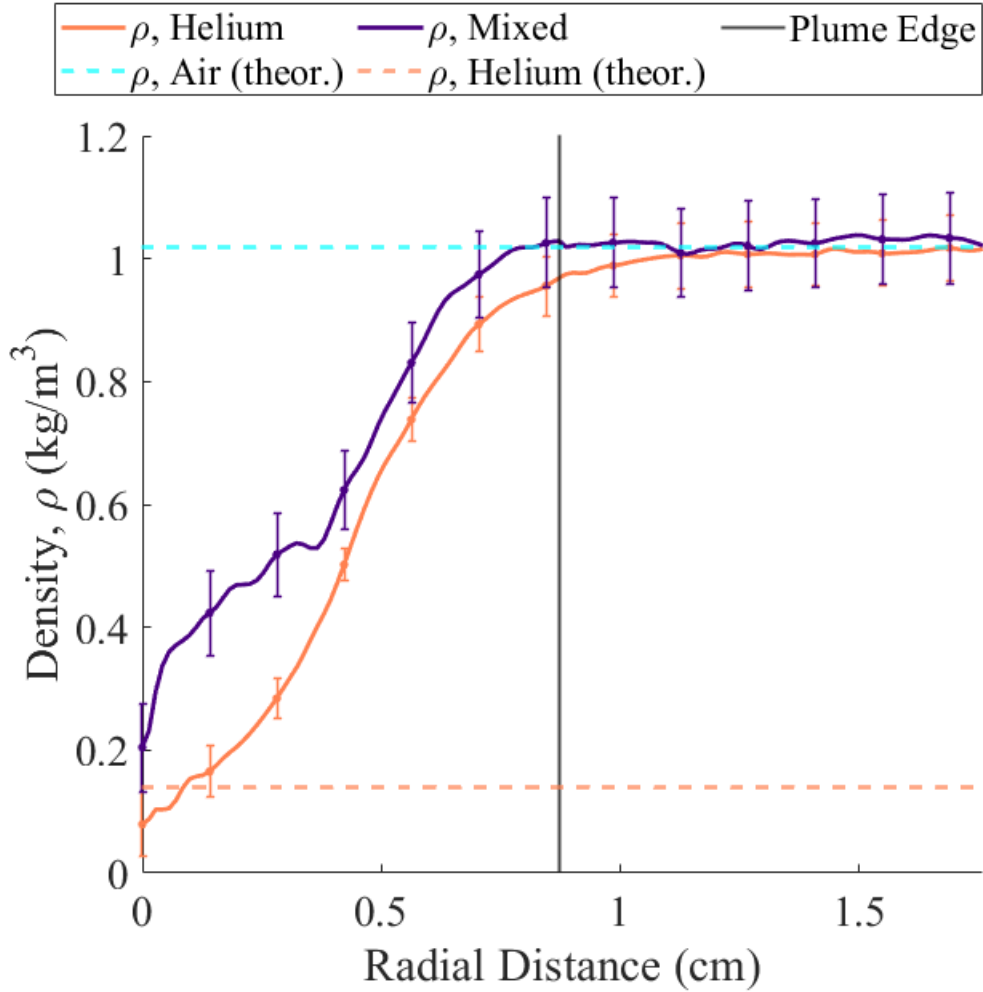


Figure 5.8: Density reconstruction of plumes from color-filtered schlieren images of a helium-only plume (coral) and mixed helium-iodine plume (purple).

5.5 Final results and discussion

The results of the color-filtered schlieren setup built upon the combined diagnostic methodology developed in Chapter 4 by applying it to the physically simplified setup of color-filtered schlieren. Rather than relying on spectrometer data for direct absorbance measurements, it was demonstrated that the dual-wavelength schlieren setup can replicate the same absorption-based insights for application to existing quantitative schlieren measurement techniques. By leveraging known differences in the absorption behavior of iodine gas between the same two wavelengths of interest, the modified schlieren system isolated the contribution of iodine gas to overall refractive changes within the flow field. The method developed here relies on calculating predicted intensity values from the 650 nm “background” view and comparing them to the 530 nm view, thereby

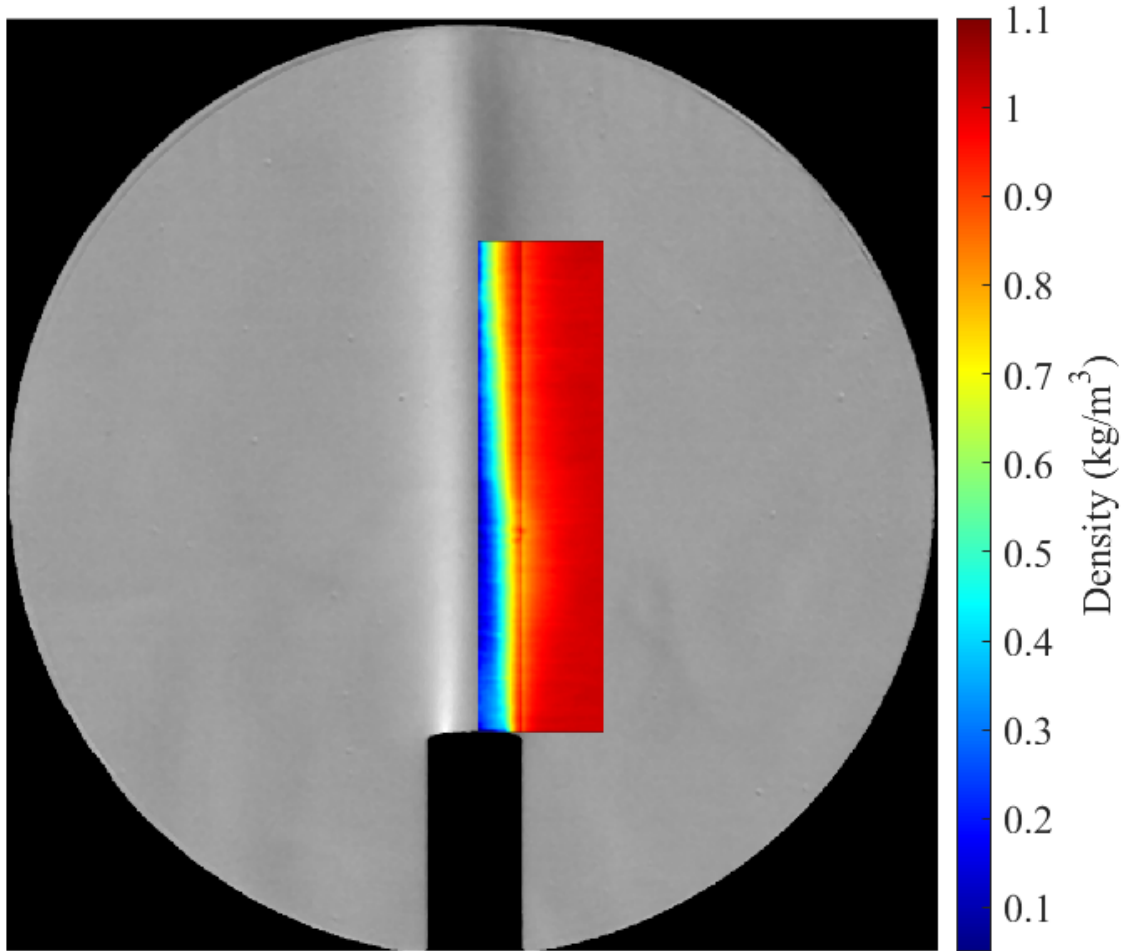


Figure 5.9: Density color map of pure helium plume using color-filtered schlieren method.

effectively canceling out refractive effects and isolating absorptive features within the plume. This enabled the calculation of LOS integrated absorbance and therefore iodine concentration using the same modified Beer-Lambert Law approach used previously. The calculated iodine concentrations were used in conjunction with Gladstone-Dale relations, similarly to Chapter 4, enabling density field reconstruction across the region of interest. Unlike the approach in Chapter 4, which averaged values along a defined center row, the color-filtered schlieren method allowed for spatially resolved reconstruction over an extended portion of the image plane. This spatial aspect provided a more detailed view of the helium-iodine plume's overall structure and composition.

However, limitations were also observed. The color-filtered schlieren approach showed slightly increased noise in the final density calculations, a result of several compounding factors. Concentration measurements were more prone to uncertainties due to the camera resolution limitation of approximately 1 MP. Still,

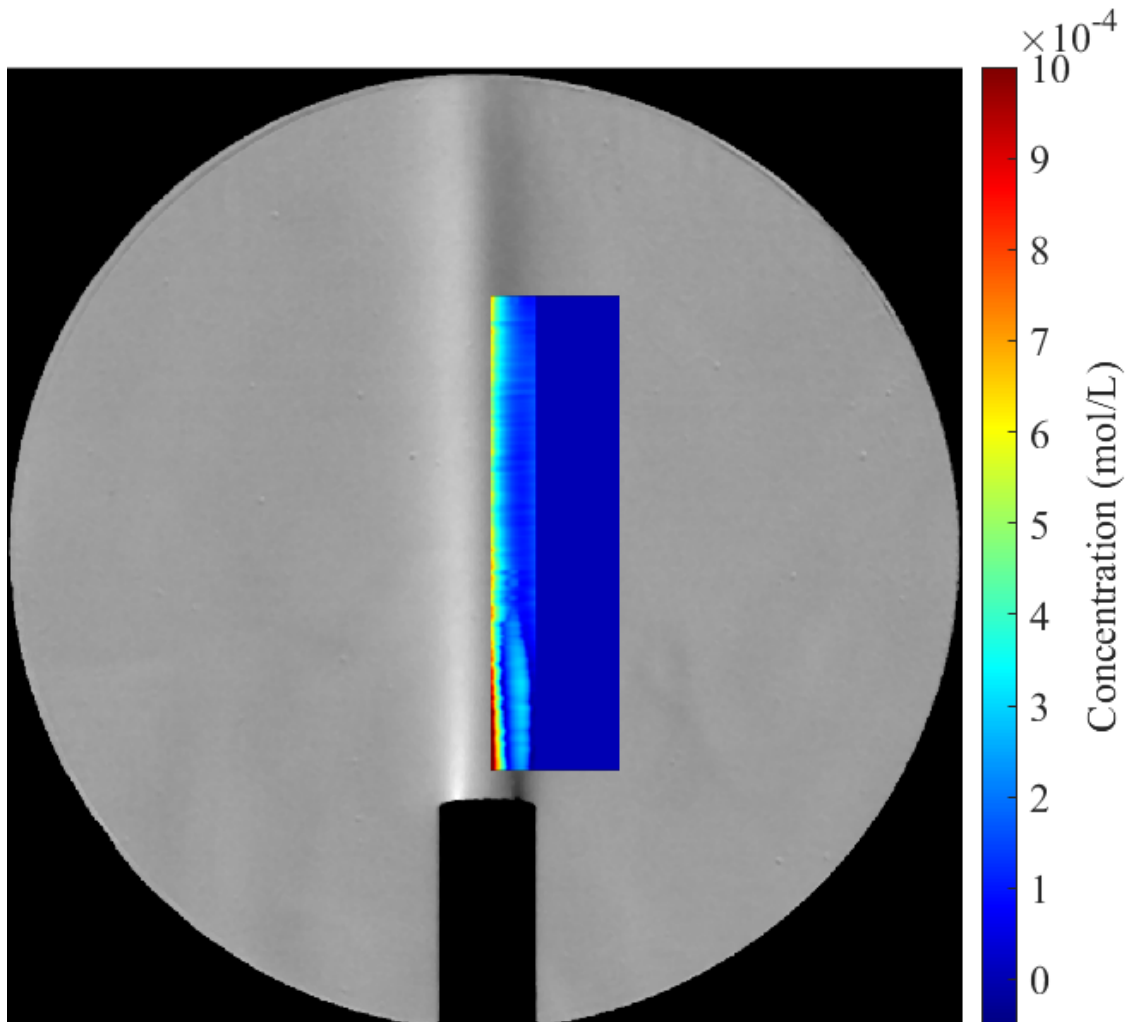


Figure 5.10: Iodine concentration color map of mixed helium-iodine plume using color-filtered schlieren method.

the strength of this approach lies in its adaptability. Once the expected optical behavior of a specific species within the flow field is known, the schlieren system can be tuned to highlight that species selectively by varying the filtering wavelengths of interest. This suggests potential for a practical, non-spectrometer-based method of species detection and density field characterization. This is particularly useful in environments where hardware limitations restrict traditional diagnostics. Over the course of the 5 tests performed using this setup, the range of calculated concentration and density values was within the same order of magnitude, as were the uncertainties calculated.

The findings here reinforce the conclusions drawn from Chapter 4, where even minimal quantities of iodine yield quantifiable changes in absorptive and refractive properties. The color-filtered schlieren method, while currently less precise, offers

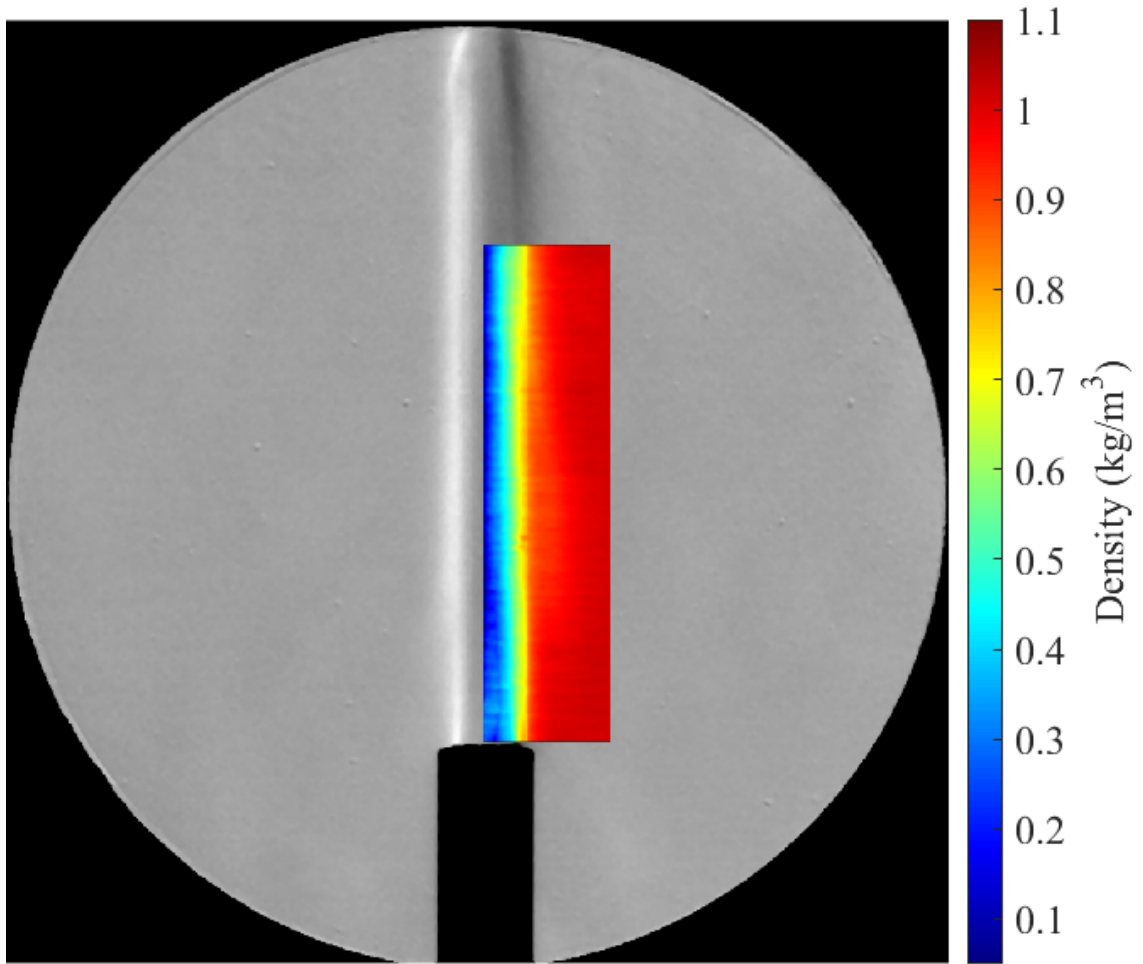


Figure 5.11: Density color map of mixed helium-iodine plume using color-filtered schlieren method.

a valuable and adaptable tool for multi-species flow characterization, especially when prior knowledge of the medium allows for tailored optical filtering and data interpretation.

CHAPTER 6

CONCLUSIONS AND RECOMMENDATIONS FOR FUTURE WORK

The research presented here explored the development, validation, and integration of pre-existing optical diagnostic methods for multi-species flow field characterization and density reconstruction. Specifically, the previously developed common-path schlieren and imaging spectroscopy technique, and the proposed color-filtered schlieren method were explored for these purposes. These experimental methods were implemented to investigate both pure helium and mixed helium-iodine plumes. Through the use of these two approaches, key physical properties of the flow field, such as iodine concentration and local gas density, were extracted using LOS integrated absorbance data, refractive index variations, and their underlying spectroscopic signatures.

The results demonstrated that iodine presence within a helium carrier gas could be consistently quantified using spectroscopic measurements, and that these results could be translated to and validated by modern quantitative schlieren techniques. The findings showed that the schlieren system, particularly when enhanced through color filtering, could serve as a viable alternative for species-specific diagnostics when prior knowledge of the flow's spectral characteristics is available. These contributions represent a significant step towards the practical application of schlieren imaging for chemically specific flow diagnostics, especially in constrained environments where traditional instruments like spectrometers may not be feasible.

This work set out to accomplish four primary goals:

- Further develop the robustness of the common path schlieren and imaging spectroscopy technique for absorption measurements of laminar helium and helium-iodine plumes.
- Experimentally quantify iodine concentrations within laminar helium-iodine plumes.
- Demonstrate the relationship between absorption due to iodine presence and density-based refractive disturbances within the schlieren field of view.
- Develop and experimentally validate a modified schlieren technique for spectroscopic characterization without the use of a spectrometer.

Each of these objectives was successfully achieved. The combined schlieren and imaging spectroscopy technique was implemented and calibrated to enable accurate spatial correlation between the schlieren and spectrometer fields of view. Absorbance data obtained from the imaging spectrometer was shown to align closely with schlieren-derived measurements, and the combined data set enabled density field reconstruction for both pure helium and mixed helium-iodine gas plumes. The application of the Beer-Lambert Law to spectral data yielded LOS integrated absorbance measurements and local iodine concentration estimates. These were validated against known absorption properties of iodine gas and provided reliable concentration values under these flow conditions. The relationship between absorption due to iodine presence and density-based refractive disturbances within the schlieren field of view was clearly established. Results showed that iodine, even at low concentrations, produced measurable changes in both absorbance and refractive index. These changes were tracked across the flow field and were shown to be proportional to iodine concentration, reinforcing the diagnostic sensitivity of the combined method. The color-filtered schlieren system also replicated the diagnostic capabilities of the spectrometer-based setup using only bandpass filters at two carefully selected wavelengths. While slightly noisier, the color-filtered schlieren approach enabled iodine concentration and density field estimation without the need for full spectral analysis. Together, these accomplishments suggest that schlieren imaging, when combined with either spectroscopic data or wavelength-specific filtering, can be extended beyond current quantitative schlieren capabilities into the realm of species-sensitive diagnostics.

Moving forward with this work, a recommendation for improved data resolution and error reduction is to use higher resolution cameras, especially for comparing multiple views of the same flow field. The camera used to capture absorption measurements had approximately 1 megapixel of resolution. Error propagation was exacerbated by the need to interpolate and smooth data in the absorption measurements taken with this camera. Increasing the camera's resolution to the next step up of approximately 4.2 megapixels would allow for greater sensitivity to changes in small areas by providing more data points at each measurement location without sacrificing visualization of the full flow field. Another way to approach this issue would be to use a better camera lens with the appropriate focal length and zoom capabilities to ensure the field of view utilizes as many sensor pixels as possible. This would also reduce the need to register one image to the other if they are positioned as similarly as possible on the sensors.

A source of validation that should be explored is computational fluid dynamics (CFD) modeling. The core properties of the flow field are all known and individually well characterized, such as the expected densities of the individual flow components and the flow behavior of the laminar plume itself. These could be modeled using CFD and used as a comparison to the values calculated using spectroscopic and refractive imaging techniques.

One key source of uncertainty in this work was the true amount of iodine gas being carried by the helium gas into the test section. The amount of iodine gas theoretically produced and the amount measured optically was discussed

at length, however, a method of validating and confirming that measurement is desired before moving forward with this research. This could be done through the use of iodine gas cells with calibrated concentration values. A better method of introducing the iodine gas into the test section is also highly recommended so that concentration values can be more accurately predicted and consistently achieved. The optical diagnostics setup could also be altered to include the spectrometer in tandem with color-filtered schlieren to provide an additional source of concentration measurement validation. This was not done here because the intensity of the background light source was not strong enough to be split more than once, and would have resulted in intensities too low to resolve changes in any of the camera views.

Once the test setup and validation methods have been improved, the next step of this work should be to introduce variation in chemical species and carrier gases. This would suggest the use of different background light sources as well, both for improved overall intensity capabilities and for a wider range of interest wavelengths available for comparison. Varied chemical species would require varied wavelengths of interest for analysis, so the optical diagnostics setup should be adjusted accordingly. A lighter tracer gas should be explored first to promote better mixing within the plume, for example, xenon or argon. Once this technique has been verified for a wider range of test materials, it should be adapted to larger-scale testing. The ultimate goal of this work is to be able to track and quantify the presence of varied chemical species in the explosive environment throughout the desired field of view. Many steps are needed before that ultimate goal is reached, some of which have been demonstrated through the research presented here.

REFERENCES

- [1] G. S. Settles. *Schlieren and shadowgraph techniques: Visualizing phenomena in transparent media*. Springer-Verlag, 2001.
- [2] M.J.Hargather and G.S. Settles. A comparison of three quantitative schlieren techniques. *Optics and Lasers in Engineering*, 50, 2012.
- [3] Gary S. Settles and Michael J. Hargather. A review of recent developments in schlieren and shadowgraph techniques. *Measurement Science and Technology*, 2017.
- [4] H. Kleine. Filming the invisible - time-resolved visualization of compressible flows. *European Physical Journal: Special Topics*, 182:3–34, 2010.
- [5] Matthew M. Biss and Kevin L. McNesby. Optically measured explosive impulse. *Experiments in Fluids*, 55, 2014.
- [6] Michael J. Hargather and Gary S. Settles. Optical measurement and scaling of blasts from gram-range explosive charges. *Shock Waves*, 17, 2007.
- [7] S.M. Torres, J. Kimberly, and M.J. Hargather. Stress field measurements using quantitative schlieren. *Journal of Applied Physics*, 136, 2024.
- [8] Jesse D. Tobin and Michael J. Hargather. Quantitative schlieren measurement of explosively-driven shock wave density, temperature, and pressure profiles. *Propellants, Explosives, Pyrotechnics*, 41(6):1050–1059, 2016.
- [9] Michael J. Hargather and Gary S. Settles. Retroreflective shadowgraph technique for large-scale flow visualization. *Applied Optics*, 48:4449–4457, 2009.
- [10] M.M. Biss, G.S. Settles, M.J. Hargather, L.J. Dodson, and J.D. Miller. High-speed digital shadowgraphy of shock waves from explosions and gunshots. In *Shock Waves*, pages 91–96, 2007.
- [11] Lauri H.J. Lajunen and P. Peramaki. *Spectrochemical analysis by atomic absorption and emission*. Royal Society of Chemistry, 2nd edition, 2004.
- [12] A. L. Schawlow. Spectroscopy in a new light. *Science*, 217(4554):9–16, July 1982.
- [13] M. Varela, S. D. Findlay, A. R. Lupini, H. M. Christen, A. Y. Borisevich, N. Dellby, O. L. Krivanek, P. D. Nellist, M. P. Oxley, L. J. Allen, and S. J. Pennycook. Spectroscopic imaging of single atoms within a bulk solid. *Physical Review Letters*, 92(9), 2004.

- [14] Barun Raychaudhuri. Imaging spectroscopy: Origin and future trends. *Applied Spectroscopy Reviews*, 51:23–35, 2016.
- [15] Robert O. Green, Michael L. Eastwood, Charles M. Sarture, Thomas G. Chrien, Mikael Aronsson, Bruce J. Chippendale, Jessica A. Faust, Betina E. Pavri, Christopher J. Chovit, Manuel Solis, Martin R. Olah, and Orlesa Williams. Imaging spectroscopy and the airborne visible/infrared imaging spectrometer (aviris). *Remote Sens. Environ.*, 65:227–248, 1998.
- [16] Alfredo Sanz-Mendel and Rosario Pereiro. *Atomic Absorption Spectroscopy: An Introduction*. Momentum Press, 2nd edition, 2014.
- [17] M. Born and E. Wolf. *Principles of Optics*. Cambridge University Press, 7th edition, 1999.
- [18] Jennifer Mott Peuker, Patrick Lynch, Herman Krier, and Nick Glumac. On alo emission spectroscopy as a diagnostic in energetic materials testing. *Propellants, Explosives, Pyrotechnics*, 38:577–585, 2013.
- [19] Nick Glumac. Absorption spectroscopy measurements in optically dense explosive fireballs using a modeless broadband dye laser. *Applied Spectroscopy*, 63:1075–1080, 2009.
- [20] Zhouyu Fu, Antonio Robles-Kelly, Terry Caelli, and Robby T. Tan. On automatic absorption detection for imaging spectroscopy: A comparative study. *IEEE Transactions on Geoscience and Remote Sensing*, 45(11):3827–3844, 2007.
- [21] Michael Soo and Nick Glumac. Ultraviolet absorption spectroscopy in optically dense fireballs using broadband second-harmonic generation of a pulsed modeless dye laser. *Applied Spectroscopy*, 68(5):517–524, 2014.
- [22] Moses Kayanda Kiteto and Cleophas Achisa Mecha. Insight into the bouguer-beer-lambert law: A review. *Sustainable Chemical Engineering*, 5(2):567–587, 2024.
- [23] Thomas G. Mayerhofer, Susanne Pahlow, and Jurgen Popp. The Bouguer-Beer-Lambert law: Shining light on the obscure. *ChemPhysChem*, 21, 2020.
- [24] M. Mamouei, K. Budidha, N. Baishya, M. Qassem, and P. A. Kyriacou. An empirical investigation of deviations from the beer-lambert law in optical estimation of lactate. *Scientific Reports*, 11(13734), 2021.
- [25] Mainuddin, M.T. Beg, Moinuddin, R.K. Tyagi, and R. Rajesh. Optical spectroscopic based in-line iodine flow measurement system - an application to coil. *Sensors and Actuators*, 109:375–380, 2005.
- [26] Javier Roger, Luis Guanter, Javier Gorrone, and Itziar Irakulis-Loitxate. Exploiting the entire near-infrared spectral range to improve the detection of methane plumes with high-resolution imaging spectrometers. *Atmospheric Measurement Techniques*, 17:1333–1346, 2024.

- [27] Nicholas H. Bings, Annemie Bogaerts, and Jose A. C. Broekaert. Atomic spectroscopy: A review. *Analytical Chemistry*, 82(12), June 2010.
- [28] P. Spietz, J. Gomez Martin, and J.P. Burrows. Effects of column density on i2 spectroscopy and a determination of i2 absorption cross section at 500 nm. *Atmospheric Chemistry and Physics*, 6:2177–2191, 2006.
- [29] Andrew L. Bullard and John F. Silny. Selectable magnification reflective triplet (smart) imaging spectrometer. In *Imaging Spectrometry XXII: Applications, Sensors, and Processing*, volume 10768 of *Proceedings of SPIE*, 2018.
- [30] Ann-Marie Wennberg, Fredrik Gudmundson, Bo Stenquist, Annika Ternesten, Lena Molne, Arne Rosen, and Olle Larko. In vivo detection of basal cell carcinoma using imaging spectroscopy. *Acta Derm Venereol*, 79:54–61, 1999.
- [31] C.A. Grady, B. Woodgate, F.C. Bruhweiler, A. Boggess, Philip Plait, Don J. Lindler, and M. Clampin adn P. Kalas. *Hubble Space Telescope* space telescope imaging spectograph coronagraphic imaging of the Herbig AĒ star AB Aurigae. *The Astrophysical Journal*, 523:L151–L154, 1999.
- [32] Roger N. Clark, Robert H. Brown, Ralf Jaumann, Dale P. Cruikshank, Robert M. Nelson, Bonnie J. Buratti, Thomas B. McCord, J. Lunine, K. H. Baines, G. Bellucci, J. P. Bibring, F. Capaccioni, P. Cerroni, A. Coradini, V. Formisano, Y. Langevin, D. L. Matson, V. Mennella, P. D. Nicholson, B. Sicardy, C. Sotin, Todd M. Hoefen, John M. Curchin, Gary Hansen, Karl Hibbits, and K. D. Matz. Compositional maps of Saturn’s moon Phoebe from imaging spectroscopy. *Nature*, 435:66–69, 2005.
- [33] Susan L. Ustin, Dar A. Roberts, Josh A. Gamon, Gregory P. Asner, and Robert O. Green. Using imaging spectroscopy to study ecosystem processes and properties. *BioScience*, 54(6):523–534, 2004.
- [34] Markus Steffens and Henning Buddenbaum. Laboratory imaging spectroscopy of a stagnic luvisol profile - high resolution soil characterisation, classification and mapping of elemental concentrations. *Geoderma*, 195-196:122–132, 2013.
- [35] John F. Silny and Brad A. Flanders. Imaging spectrometer f-number optimization for remote sensing of gases. In *Imaging Spectrometry XXII: Applications, Sensors, and Processing*, volume 10768 of *Proceedings of SPIE*. SPIE, 2018.
- [36] Gerald K. Moore. What is a picture worth? a history of remote sensing. *Hydrological Sciences Bulletin*, 24(4):477–485, 1979.
- [37] Michael K. Yetzbacher and Michael J. DePrenger. The effect of lens aperture for remote sensing of trace gases using fabry-perot interferometer-based cameras. In *Imaging Spectrometry XXII: Applications, Sensors, and Processing*, volume 10768 of *Proceedings of SPIE*. SPIE, 2018.

- [38] Chongyuan Shui, Jianqing Huang, Hecong Liu, Weiwei Cai, and Scott T. Sanders. Tomographic absorption spectroscopy based on dictionary learning. *Optics Express*, 29(22):36400–36416, 2021.
- [39] Pavlos Aleiferis, Alexandros Charalambides, Yannis Hardalupas, Nikolaos Soulopoulos, A. M. K. P. Taylor, and Yunichi Urata. Schlieren-based temperature measurement inside the cylinder of an optical spark ignition and homogeneous charge compression ignition engine. *Applied Optics*, 54(14):4566–4579, 2015.
- [40] Kin-Pang Cheong, Dingfeng Shi, Shaotong Liu, Junjun Wu, Kun Duan, Yong Song, and Wei Ren. Tomographic absorption spectroscopy for H₂O transport in a laminar jet with inverse concentration gradient. *Sensors*, 22(5939), 2022.
- [41] Cameron J. Dasch. One-dimensional tomography: a comparison of abel, onion-peeling, and filtered backprojection methods. *Applied Optics*, 31(8):1146–1152, 1992.
- [42] Jing-Wen Shi, Hong Qi, Jun-You Zhang, Ya-Tao Ren, Li-Ming Ruan, and Yong Zhang. Simultaneous measurement of flame temperature and species concentration distribution from nonlinear tomographic absorption spectroscopy. *Journal of Quantitative Spectroscopy and Radiative Transfer*, 241(106693), 2020.
- [43] Dingfeng Shi, Kin-Pang Cheong, Tengfei Jiao, Junjun Wu, Yong Song, Yushuai Liu, and Wei Ren. Time-averaged tomographic absorption spectroscopy for h₂o diffusion in turbulent jet flow at room temperature. *International Journal of Hydrogen Energy*, 52:133–146, 2024.
- [44] Frederic Champagnat, Aurelien Plyer, Olivier Leon, Philippe Cornic, David Donjat, and Francois Nicolas. Abel inversion from central-projection background oriented schlieren observations for reconstruction of axisymmetric refractive media. *Applied Optics*, 64(2):350–358, 2025.
- [45] Pankaj S. Kolhe and Ajay K. Agrawal. Abel inversion of deflectometric data: comparison of accuracy and noise propagation of existing techniques. *Applied Optics*, 48(20):3894–3902, 2009.
- [46] Daniel D. Hickstein, Stephen T. Gibson, Roman Yurchak, Dhruvajyoti D. Das, and Mikhail Ryazanov. A direct comparison of high-speed methods for the numerical abel transform. *Review of Scientific Instruments*, 90(065115), 2019.
- [47] Joshua Smith. Design and construction of a fixture to examine the product flow of Al/I₂O₅ using schlieren, spectroscopy, and pressure. Master’s thesis, New Mexico Institute of Mining and Technology, 2016.
- [48] James Anderson. Study of turbulent mixing in a post detonation environment using schlieren and imaging spectroscopy. Master’s thesis, New Mexico Institute of Mining and Technology, 2017.

- [49] Chen Wang, He Chen, Yinchao Zhang, Siying Chen, Pan Guo, and Lifu Wang. Optical design of a crossed czerny–turner spectrometer with a linear array photomultiplier tube. *Applied Optics*, 58(28):7789–7796, 2019.
- [50] Muddasir Naeem, Noor ul-ain Fatima, Mukhtar Hussain, Tayyab Imran, and Arshad Saleem Bhatti. Design simulation of czerny–turner configuration-based raman spectrometer using physical optics propagation algorithm. *Optics*, 3(1):1–7, 2022.
- [51] Su Wu, Tao Wang, Chan Huang, Jiapeng Gu, Lei Yu, Hui Xue, and Yuan Shen. Advanced optical design of czerny–turner spectrometer with high flux and low aberration in broadband. *Applied Optics*, 61(11):3077–3083, 2022.
- [52] David R. Bull. *Communicating Pictures*. Academic Press, 2014.
- [53] Joel Tellinghuisen. Transition strengths in the visibleinfrared absorption spectrum of I2 into three contributing transitions. *The Journal of Chemical Physics*, 58:2821–2834, 1973.
- [54] A Saiz-Lopez, S H Ashworth R W Saunders, D M Joseph, and J M C Plane. Absolute absorption cross-section and photolysis rate of I2. *Atmos. Chem. Phys. Atmospheric Chemistry and Physics*, 4:1443–1450, 2004.
- [55] National Institute of Standards and Technology (NIST). Nist atomic spectra database (asd), version 5.10, 2024. Accessed: 20-Feb-2025.
- [56] M. Yousef Bahadori, Dennis P. Stocker, David F. Vaughan, Liming Zhou, and Raymond B. Edelman. Effects of buoyancy on laminar, transitional, and turbulent gas jet diffusion flames. In *Second International Workshop on Combustion Science in Microgravity*, pages 91–105, 1993.
- [57] Pijush K. Kundu and Ira M. Cohen. *Fluid mechanics*. Elsevier Academic Press, Amsterdam, 3. ed., [repr.] edition, 2006.
- [58] Maria N. D’Orazio, Christian Peterson, and Michael J. Hargather. Characterization of the fractal dimension of helium plumes in laminar to turbulent transition. *Experiments in Fluids*, 66(70), 2025.
- [59] Eugene Hecht and Alfred Zajac. *Optics*. Addison-Wesley Publishing Company, Inc., 1974.
- [60] Philip E. Ciddor. Refractive index of air: new equations for the visible and near infrared. *Applied Optics*, 35(9):1566–1573, 1996.
- [61] D. F. Swinehart. The beer-lambert law. *Journal of Chemical Education*, 39(7), July 1962.
- [62] Aydan Yeltik and Yusuf Kelestemur Burak Guzelturk Hilmi Volkan Demir Savas Delikanli, Murat Olutas. Experimental determination of the absorption cross-section and molar extinction coefficient of colloidal cdse nanoplatelets. *The Journal of Physical Chemistry*, 119:26768–26775, 2015.

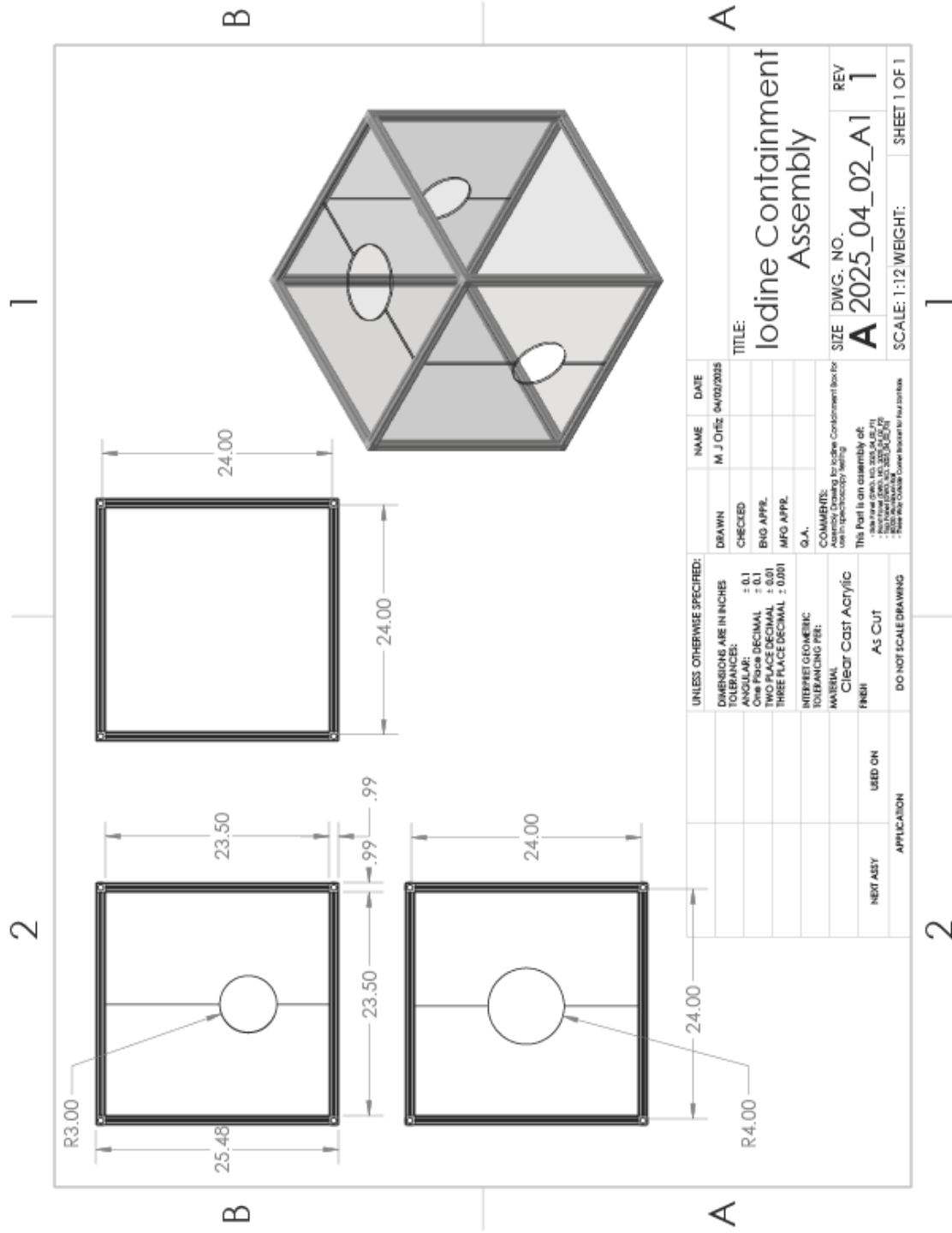
- [63] Jen Beatty. The radon transform and the mathematics of medical imaging. Master's thesis, Colby College, 2012.
- [64] Carolyn Christiansen and Gengsheng L. Zeng. Sinogram interpolation inspired by single-image super resolution. *Journal of Biotechnology and its Applications*, 2, 2023.
- [65] Christopher T. Wanstall, Ajay K. Agrawal, and Joshua A. Bittle. Implications of real-gas behavior on refractive index calculations for optical diagnostics of fuel-air mixing at high pressures. *Combustion and Flame*, 214:47–56, 2020.

APPENDIX A

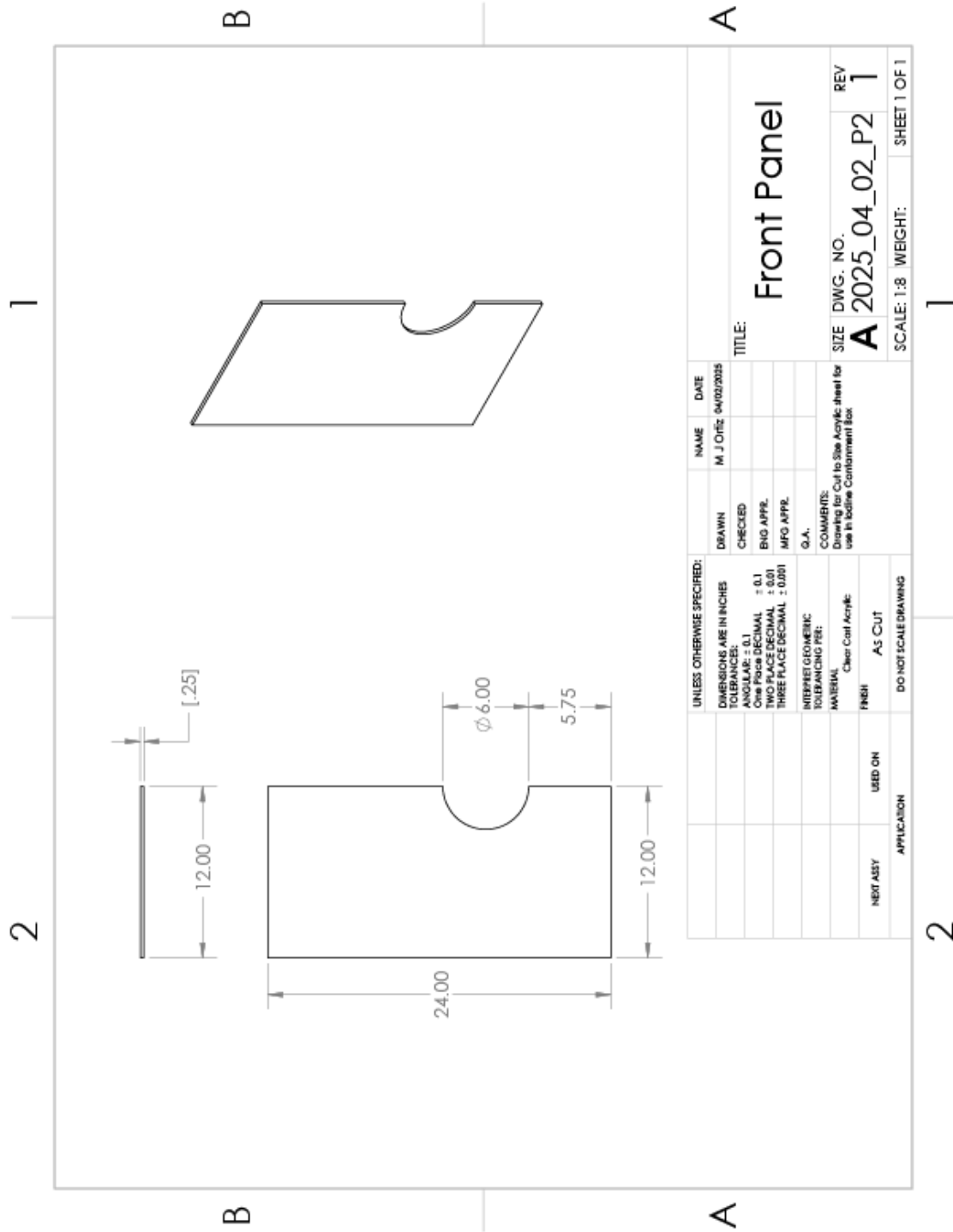
GAS CONTAINMENT BOX ENGINEERING DRAWINGS

The following pages provide a detailed overview of how the iodine containment box was constructed with ports for schlieren lenses and a ventilation fan.

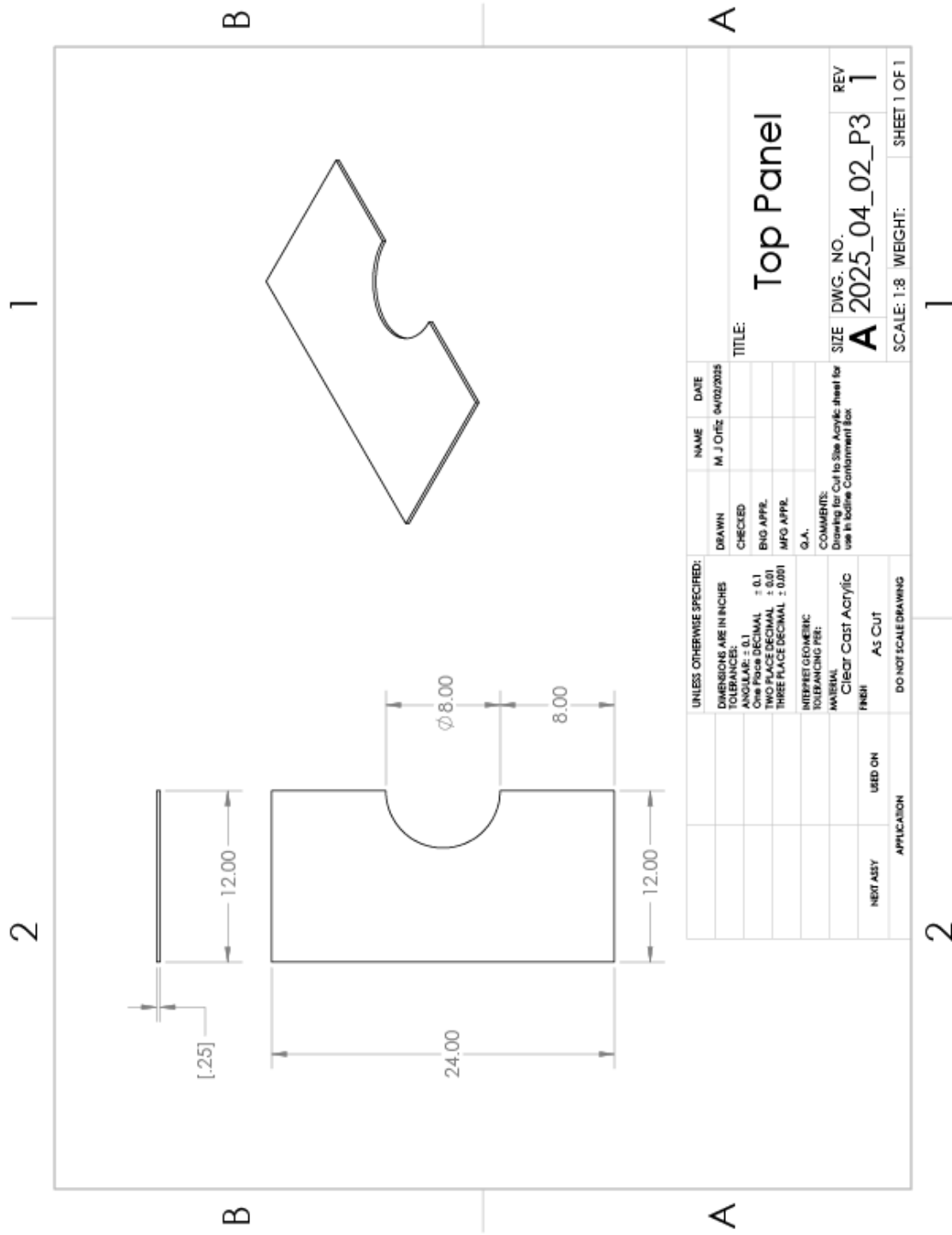
A.1 Full Containment Box Assembly



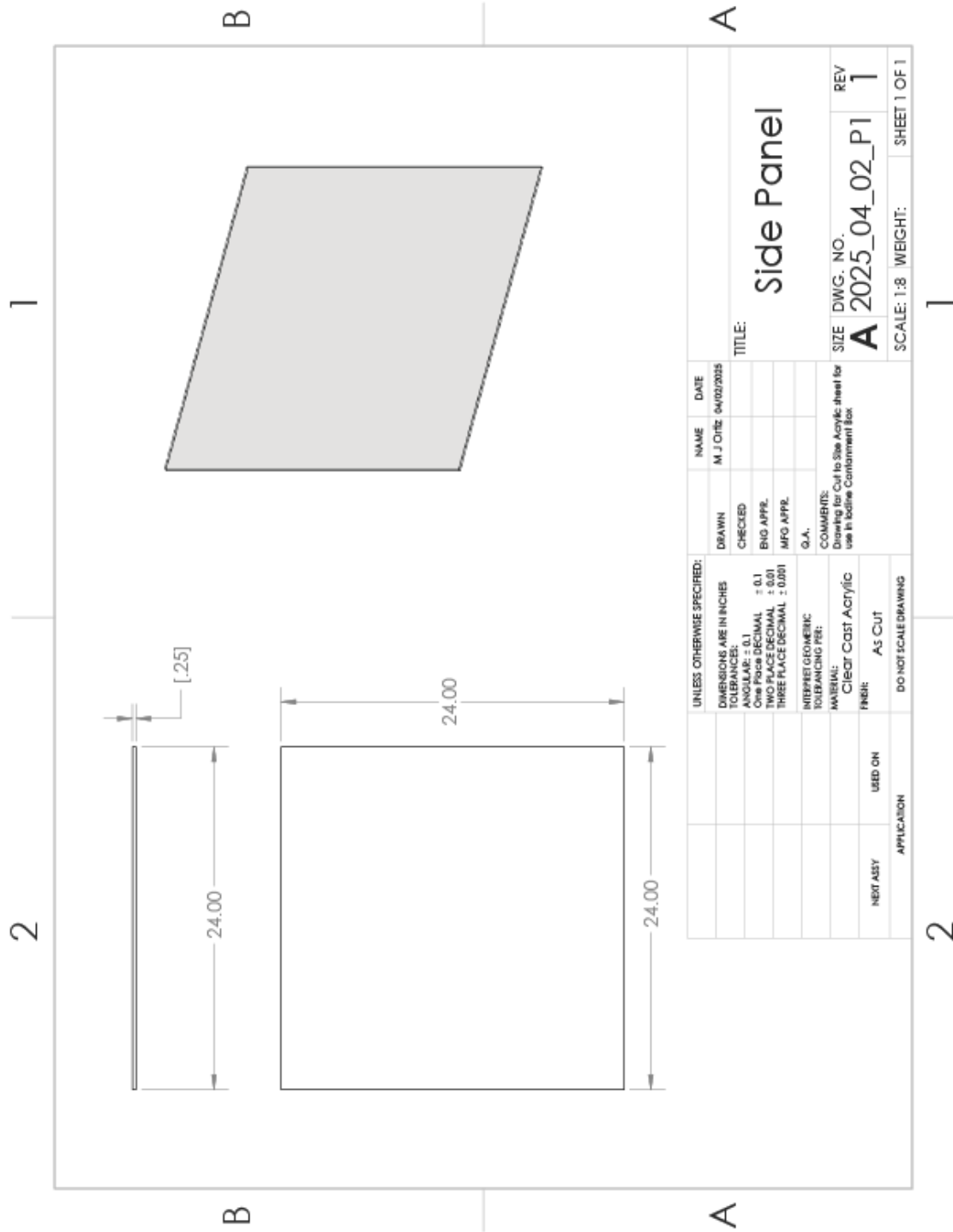
A.2 Front Panel



A.3 Top Panel



A.4 Side Panel



UNLESS OTHERWISE SPECIFIED:		NAME	DATE
DRAWN	M. J. OTR	04/02/2025	
CHECKED			
ENG. APPR.			
MFG. APPR.			
DIMENSIONS ARE IN INCHES			
TOLERANCES:			
FRACTIONS ± 0.1			
ONE PLACE DECIMAL ± 0.1			
TWO PLACE DECIMAL ± 0.01			
THREE PLACE DECIMAL ± 0.001			
INTERPRET GEOMETRIC TOLERANCING PER:			
MATERIAL:			
FINISH:			
NEXT ASSY	USED ON		
APPLICATION			
DO NOT SCALE DRAWING			
		COMMENTS:	
		Drawing for Cut to Size Acrylic sheet for use in Isoline Containment Box	
		SIZE	DWG. NO.
		A	2025_04_02_P1
		SCALE: 1:8	WEIGHT:
			SHEET 1 OF 1
		TITLE: Side Panel	
		REV	
			1

COMBINED SCHLIEREN AND
IMAGING SPECTROSCOPY FOR MULTI-SPECIES
FLOW FIELD CHARACTERIZATION AND
DENSITY RECONSTRUCTION

by

Maria J. Ortiz

Permission to make digital or hard copies of all or part of this work for personal or classroom use is granted without fee provided that copies are not made or distributed for profit or commercial advantage and that copies bear this notice and the full citation on the last page. To copy otherwise, to republish, to post on servers or to redistribute to lists, requires prior specific permission and may require a fee.

